Theory of Semiconductor Quantum Wires

by

Yinlong Sun

B.S., Beijing University, 1985

A THESIS SUBMITTED IN PARTIAL FULFILLMENT
OF THE REQUIREMENTS FOR THE DEGREE OF
DOCTOR OF PHILOSOPHY
in the Department
of
Physics

SIMON FRASER UNIVERSITY
August 1995

APPROVAL

Name: Yinlong Sun

Degree: Doctor of Philosophy

Title of thesis: Theory of Semiconductor Quantum Wires

Examining Committee: Dr. J. C. Irwin
Chair

Dr. George Kirczenow
Senior Supervisor

Dr. Michael L. W. Thewalt

Dr. Daniel Loss

Dr. Colombo R. Bolognesi

Dr. Sergio E. Ulloa
External Examiner
Department of Physics, Ohio University, Athens,
Ohio, U.S.A.

Date Approved: August 22, 1995

PARTIAL COPYRIGHT LICENSE

I hereby grant to Simon Fraser University the right to lend my thesis, project or extended essay (the title of which is shown below) to users of the Simon Fraser University Library, and to make partial or single copies only for such users or in response to a request from the library of any other university, or other educational institution, on its own behalf or for one of its users. I further agree that permission for multiple copying of this work for scholarly purposes may be granted by me or the Dean of Graduate Studies. It is understood that copying or publication of this work for financial gain shall not be allowed without my written permission.

Title of Thesis/Project/Extended Essay

Theory of Semiconductor Quantum Wires

Author:_____
(signature)

Yinlong Sun
(name)

1 September 1995
(date)

To my parents

ACKNOWLEDGEMENTS

There are many people who helped and supported me as I studied and did research for this thesis. I would like to take this opportunity to thank them.

First, my thanks go to my supervisor, Professor George Kirczenow, for suggesting the research project of this thesis and helping me understand many problems in the area of semiconductor structures. This thesis would not have been possible without his meticulous direction and profound inspiration. Through the years working with him, I have been greatly influenced by his deep insight in mastering the nature of complex systems and his rigorous attitude in understanding scientific problems. In particular, I thank him for reading the whole draft of this thesis and making many valuable suggestions.

Professor Michael Thewalt and Professor Daniel Loss also always found time to have discussions with me and to give me valuable advice on my research. I would like to express my appreciation to them.

I want to thank Prof. Michael Wortis, Prof. Robert Frindt, Prof. Anthony Arrott, Prof. Michael Plischke, Prof. Brett Heinrich, and Dr. Weiming Que for constructive discussions and generous help.

I am very grateful to Dr. Andrew Sachrajda and his collaborators at the Institute of Microstructural Sciences at NRC for providing important experimental data for my studies of gated quantum wires that are presented in this thesis. I have benefited a great deal from their experimental points of view and from the first-hand information on sample fabrication and measurements. I am also very grateful to Dr. Chris Ford for helpful discussions and experimental information, and to Dr. Charles Smith for allowing me to reproduce his experimental results for two parallel quantum wires in my thesis.

I would like to thank Simon Fraser University and NSERC for financial support, the Academic Computing Services for helpful services, and the Department of Physics for its wonderful working environment.

Finally, I give my special thanks to my wife and to my parents for their constant support and encouragement.

ABSTRACT

Quantum wires fabricated from semiconductors have stimulated tremendous interest among physicists because of their novel one-dimensional properties and potential device applications. This thesis presents theoretical studies of the electronic properties of quantum wires.

The first project of this thesis is a numerical study of many-body effects in quantum wires. For the purpose of the calculations, we introduce a model of Coulomb-confined quantum wires, in which electrons are confined by Coulomb interactions. Based on the density functional theory of Hohenberg, Kohn and Sham, the electronic structure of a Coulomb-confined quantum wire is calculated by solving self-consistently the Schrödinger and Poisson equations that describe the electrons. The calculations show that many-body effects are important in quantum wires of this type, and that the exchange and correlation energies should be included to obtain qualitatively accurate results.

The second project is on correlations between interacting parallel quantum wires. It is motivated by an experimental observation of apparent energy level locking in two parallel quantum wires. We simulate a system of two parallel quantum wires numerically, using the Coulomb-confined model and the density functional theory. The calculated electronic structure clearly shows that transverse energy levels lock together in pairs when the two wires have similar widths. The energy level locking is a novel effect of Coulomb interactions between the quantum wires and of the density of states singularities that are characteristic of one-dimensional electronic systems. Several new methods for detecting such effects experimentally are suggested.

The last project of this thesis is the establishment and solution of a realistic model of gated quantum wires, which is closely related to device applications. This model incorporates the properties of semiconductor donors and surfaces, and quasi-equilibrium considerations. Using the Green's function method, a general solution of the electrostatic potential has been obtained within the model. In particular, the depletion and pinchoff voltages are calculated analytically, and the calculated results agree well with experimental measurements. This model and its analytic solution provide both a general theoretical tool for studying gated semiconductor devices and important information for improving device performance.

Contents

List of Tables

List of Figures

Chapter 1

Introduction

1.1 General Background

Physicists have long been interested in low-dimensional systems. However, only in recent decades have modern technologies made it possible to realize systems that exhibit reduced dimensionalities, and made studies of these systems feasible.

The dimensionality of a system is not an absolute feature, but depends on the physical process being considered. In studying an electronic system, for example, its dimensionality usually involves comparisons between its physical dimensions and the Fermi wavelength of electrons. When one physical dimension of a three-dimensional system becomes comparable to the Fermi wavelength, the energy levels associated with that dimension become quantized and the system becomes effectively two-dimensional. Similarly, effectively one- or zero-dimensional systems arise when two or three physical dimensions of a three-dimensional system become comparable to the Fermi wavelength.

In recent decades, low-dimensional systems have attracted much attention. These systems include electrons on liquefied noble gases [1], in intercalated graphite [2], in bicrystals [3], in high temperature superconductors [4], in transition metal dichalcogenides [5], in polyacetylene [6], and in other layered and chain-like crystals and molecules [7]. In particular, a great deal of work has been devoted to the studies of *semiconductor structures* that exhibit low dimensionalities. [8, 9, 10]

With molecular beam epitaxy (MBE) [11] or organo-metallic chemical vapor deposition (OMCVD) [12], it is now possible to fabricate *heterostructures* [8] that consist of different layers of semiconductors with thicknesses on the 10 nm scale. In such a heterostructure, a

two-dimensional electron gas (2DEG) is realized when some semiconductor layer is appropriately doped with donors. With modern confining techniques [13], the 2DEG can be further confined laterally to a region with dimensions on the 100 nm scale. This laterally confined heterostructure, which is usually called a *nanostructure* [9, 10], provides a typical one- or zero-dimensional system of electrons. Because of the rich variety of possible combinations of materials, geometries, and external fields, the low-dimensional semiconductor structures display many extraordinary properties, which have stimulated tremendous interest among physicists in their novel physics and possible device applications. [8, 9, 10]

The semiconductor structures can be divided into three major categories:

- *Two-dimensional systems.* These systems refer to the 2DEGs in heterostructures that have no lateral confinement. Typical examples are *quantum wells* [8], which have one semiconductor layer sandwiched between two layers of a different semiconductor. The energy levels of these systems are quantized in the normal direction which is perpendicular to the heterostructure layers. Electrons or holes can move freely in a plane that is parallel to the layers. Interesting features of these systems include transitions of electrons between the quantized levels [14], coupled quantum wells [15], and the quantum Hall effect [16, 17].

- *One-dimensional systems.* These systems refer to the 2DEGs in heterostructures which are further confined in one lateral direction. [9, 10] The energy levels are thus quantized in both the normal direction and the direction of the lateral confinement, and electrons can move freely only in the third direction. Such systems are usually called *quantum wires.* Interesting features include conductance quantization [18, 19], electronic correlations between quantum wires [20], quantum transmission resonances [21, 22, 23] and random telegraphic signals [24].

- *Zero-dimensional systems.* These systems are also based on the 2DEGs in heterostructures but the 2DEGs are confined in both lateral directions. [10] The energy levels are thus quantized in three dimensions, and electrons can not move freely in any direction. Such systems are usually called *quantum dots.* Interesting features include Aharonov-Bohm effect [25], Coulomb blockade [26], and interference phenomena between quantum dots in chains [27, 28] and arrays [29, 30].

This thesis is about quantum wires—the one-dimensional electronic systems based on semiconductor heterostructures. It presents theoretical studies of the electronic structure

of the ground state of quantum wires [31], of the correlation effects between interacting parallel quantum wires [32, 33, 34], and of the electrostatic confinement of electrons in realistic quantum wires [35].

Here is the outline of this thesis. In the following sections of this chapter, we make a general review of the fabrication of quantum wires, their experimental properties, and the corresponding theoretical studies with emphasis on those that are closely related to the topics of this thesis. After this chapter, we concentrate on numerical studies, which are covered in three chapters. Chapter 2 describes the basis of the numerical calculations. Chapter 3 presents the calculated electronic structure and discussion of the many-body effects in quantum wires. Chapter 4 presents numerical studies of the correlation effects in two parallel quantum wires and their experimental implications. Then we concentrate on analytic studies, establishing a realistic model of quantum wires in Chapter 5 and performing the relevant calculations in Chapter 6. An overall summary of this thesis is given in Chapter 7.

In this thesis, we only consider quantum wires that are based on GaAs-$Al_xGa_{1-x}As$ heterostructures. This is because most quantum wires fabricated and studied experimentally are of this type. For quantum wires fabricated from other semiconductors [9] the physics can be similar. Therefore, many of the conclusions and techniques discussed in this thesis can also be applied to the quantum wires which are based on materials other than GaAs and $Al_xGa_{1-x}As$.

1.2 Fabrication

For most quantum wires, the fabrication process can be divided into two steps. In the first step, a 2DEG is realized in a semiconductor heterostructure which is grown with MBE [11] or OMCVD [12]. In the second step, the 2DEG is further confined laterally using various confinement techniques. We will discuss these two steps separately.

1.2.1 2DEGs in Heterostructures

It is now possible to use MBE or OMCVD to produce a perfect crystal on a substrate by depositing a single monolayer at a time. By abruptly changing the species being deposited, one can create a material interface which is atomically flat and has extremely low concentrations of impurities and defects. [11, 12] With such a remarkable control of material growth,

semiconductor heterostructures consisting of multiple layers can be produced easily.

A typical modulation-doped [36] heterostructure is shown in Fig. 1.1(a). The layers from bottom to top are a semiconductor substrate, GaAs channel, undoped $Al_xGa_{1-x}As$, Si-doped $Al_xGa_{1-x}As$, and GaAs cap, respectively. The layer thicknesses of the GaAs cap, Si-doped $Al_xGa_{1-x}As$, and undoped $Al_xGa_{1-x}As$ are t_c, t_d, and t_s, respectively, which are typically on the 10 nm scale. A 2DEG is present at the interface between the layers of the GaAs channel and undoped $Al_xGa_{1-x}As$, at a distance $L = t_c + t_d + t_s$ from the top surface. In this modulation-doped heterostructure, the 2DEG is spatially separated from the Si donors. The undoped $Al_xGa_{1-x}As$ layer, which is usually called a *spacer*, is used to decrease scattering of electrons of the 2DEG by the Si donors. The GaAs cap layer is used to make the system more stable. For convenience of our discussion, we choose the coordinate frame in such a way that the z-axis points from the top surface into the heterostructure.

To see how the 2DEG is formed, let us look at the energy band structure shown in Figure 1.1(b). Note that the valence and conduction band edges of GaAs locate within the band gap of the $Al_xGa_{1-x}As$, which results in the conduction band offset ΔE_c. The electrons donated by the Si donors in the doped $Al_xGa_{1-x}As$ layer can be trapped in some localized states associated with the Si donors. However, because of the small binding energy ($\sim$6 meV) of the localized states, electrons can easily be excited to the conduction band of $Al_xGa_{1-x}As$. These excited electrons can transfer to the GaAs channel layer to occupy conduction band states of the GaAs to lower their energies. These electrons can also transfer to the surface of the GaAs cap layer to occupy the surface states. (The energy difference between the conduction band minimum and the energy of surface states at $z = 0$ is called the *surface Schottky barrier*, which is denoted by Φ_{ssb}.) Because the ionized Si donors left in the Si-doped $Al_xGa_{1-x}As$ layer have positive charges, they attract electrostatically the electrons that have transferred to the GaAs channel layer. This attraction confines the electrons to the interface at $z = L$ and thus makes the electrons form a 2DEG. At the same time, the space charges that are present cause all energy bands to bend within the heterostructure, as shown in Figure 1.1(b).

The quality of a 2DEG depends on a few basic parameters such as the effective mass of the electrons m^*, electron mobility μ, electron mean free path l, Fermi velocity v_F, and area electron density n. In the GaAs-$Al_xGa_{1-x}As$ heterostructure, $m^* = 0.067m_e$, which corresponds to the effective mass of electrons at the bottom of GaAs conduction band. The electron mobility is a very important parameter. It is defined as the ratio of the average

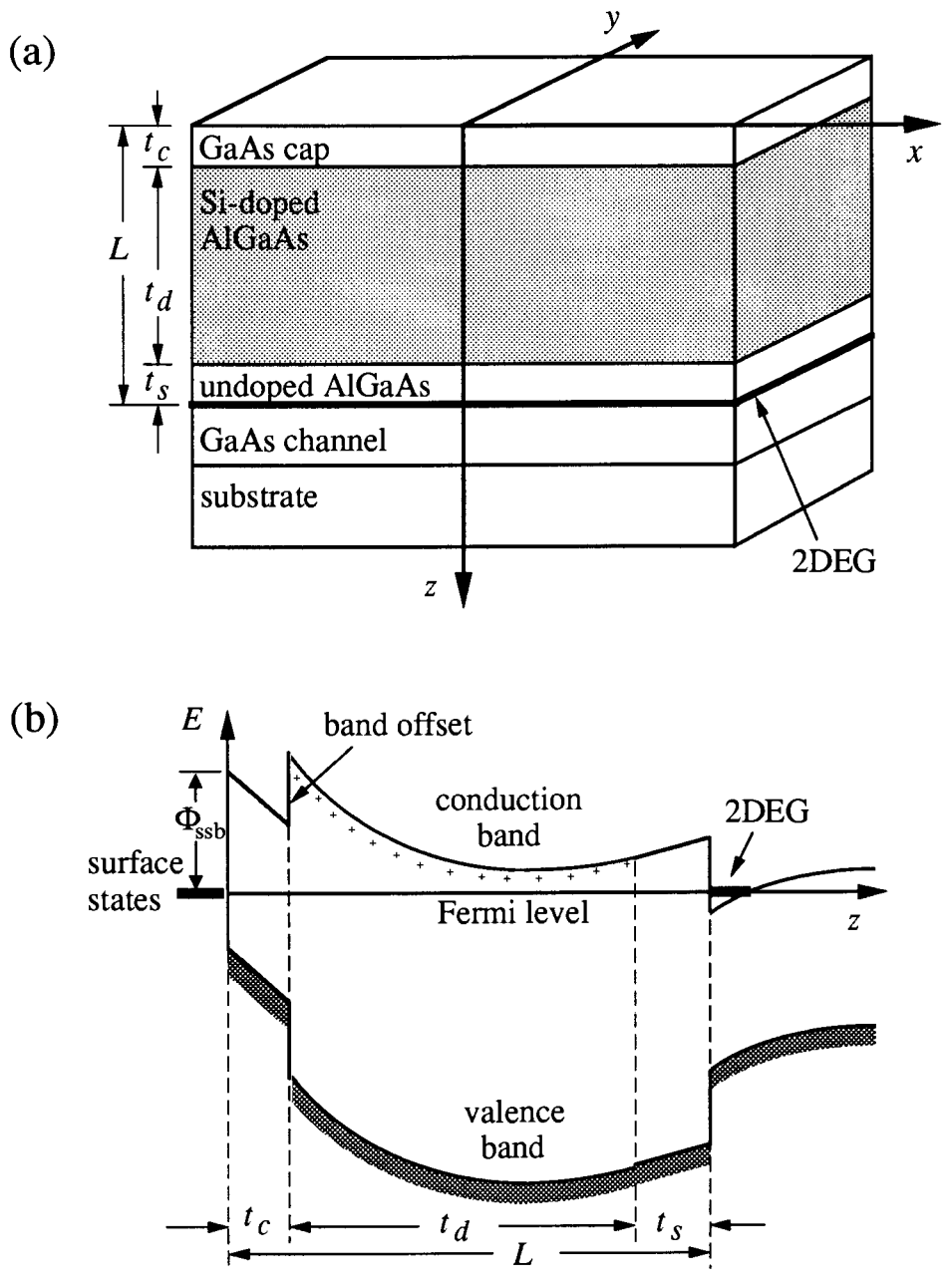

Figure 1.1: (a) A typical GaAs-$Al_xGa_{1-x}As$ heterostructure with a 2DEG present at the $z = L$ interface. (b) The band structure of the heterostructure along the z-axis. The system is in equilibrium with the Fermi energy chosen to be zero. The conduction and the valence bands are bent due to the presence of the space charges.

drift velocity of an electron in an external electric field

$$\bar{\mathbf{v}}_{\text{drift}} = -\mu\mathbf{F}, \tag{1.1}$$

where the negative sign appears because the electron drift in the direction opposed to that of the electric field $\mathbf{F}$. Thus, the electric current density can be expressed as

$$\mathbf{j}_{\text{drift}} = -en\bar{\mathbf{v}}_{\text{drift}} = en\mu\mathbf{F}, \tag{1.2}$$

where n is the density of electrons. Relating the electron mobility to the scattering of electrons, we find

$$\mu = \frac{e\tau}{m^*}, \tag{1.3}$$

where τ is the effective scattering time, which is the relaxation time for the electron distribution. Correspondingly, the electron transport mean free path is given by

$$l = v_{\text{F}}\tau. \tag{1.4}$$

A high-quality 2DEG requires both large values of the electron mobility and correspondingly large values of the electron mean free path.

For general reference, we list in Table 1.1 the typical parameter values for 2DEGs as well as for GaAs-$Al_xGa_{1-x}As$ heterostructures. The values of the electron mobility and mean free path are for low temperatures ($T \leq 1$ K). Note that the electron mobility is $10^4 - 10^6$ cm^2/Vs, which is very large. This is because of the small effective mass of the electron and the large electron scattering time. For the 2DEG in a GaAs-$Al_xGa_{1-x}As$ heterostructure, phonon scattering is low at low temperatures, the scattering by Si donors is much reduced by the spacer, and the interface scattering is negligible because of the smooth GaAs-$Al_xGa_{1-x}As$ interface realized with MBE or OMCVD [11, 12].

1.2.2 Lateral Confinement

The second step in fabricating quantum wires is to apply a lateral confinement to the 2DEG in the GaAs-$Al_xGa_{1-x}As$ heterostructure. Many lateral confinement techniques [13] have been used in laboratories. In the following discussion, however, we focus only on the four major confinement techniques: selective etching, split gates, ion implantation, and selective epitaxy.

In applying the lateral confinement, a surface *patterning* process is always involved. The most widely used patterning techniques are electron-beam lithography [37], ion-beam

Table 1.1: Typical parameter values for 2DEGs and GaAs-$Al_xGa_{1-x}As$ heterostructures. (Refer to Ref. [9].) The electron mobility and mean free path are for low temperatures ($T \leq 1$ K).

Type	Description	Notation	Value	Unit
2DEG	effective mass of electron	m^*	0.067	m_e
	scattering time	$\tau = m^*\mu_e/e$	$0.4 - 40$	ps
	electron mobility	μ_e	$10^4 - 10^6$	cm^2/Vs
	area density	n	$1 - 6$	$10^{11}cm^{-2}$
	Fermi wave vector	$k_F = (2\pi n)^{1/2}$	~ 1.5	$10^6 cm^{-1}$
	Fermi wave length	$\lambda_F = 2\pi/k_F$	~ 40	nm
	Fermi energy	$E_F = \hbar^2 k_F^2/2m^*$	~ 10	meV
	Fermi velocity	$v_F = \hbar k_F/m^*$	~ 2	$10^7 cm/s$
	mean free path	$\ell = v_F\tau$	$10^2 - 10^4$	nm
Others	dielectric constant	ε	12.5	
	band gap of GaAs	E_g	1.42	eV
	conduction band offset	ΔE_c	~ 0.2	eV
	z-directional energy spacing	ΔE_z	~ 0.04	eV
	surface Schottky barrier	Φ_{ssb}	~ 0.8	eV
	binding energy of shallow donors	E_b	~ 6	meV

lithography [38], and optical lithography [39]. To produce a surface pattern, one deposits on the substrate surface a thin layer of some particle- or optical-sensitive resist material, which is usually a polymer material such as poly-methyl methacrylate (PMMA). Then a selected area of the resist is exposed to highly focused beams of electrons, ions, or photons, which cause a chemical or structural change in the exposed area. For a positive resist, the exposure causes a bond breaking in the selected area of the resist, and the exposed area is washed away later by the developer. For a negative resist, the exposure induces cross-links between polymer chains and the unexposed area will be washed away. The resist that remains on the substrate provides the pattern which is ready to be used in the following techniques.

Selective Etching

This technique produces a lateral confinement of the 2DEG in the GaAs-$Al_xGa_{1-x}As$ heterostructure by selectively removing its top layers with chemical reactions. [40] A conventional approach is the *deep mesa method* [41, 42, 43] where the heterostructure is etched deeply down to the GaAs channel layer with only the central region not etched (Figure 1.2(a)). Wide Hall bars are usually fabricated in this way. However, for quantum

wires with widths below 1 μm, the deep mesa method is not reliable because the mobility of electron is degraded significantly by the exposed side walls.

A newer approach is the *shallow mesa method* [44, 45, 46, 47], which achieves the lateral confinement by etching away only a thin layer of the GaAs cap (Figure 1.2(b)). The shallow mesa requires that the 2DEG be sensitive to the thickness of the cap layer. That is, electrons of the 2DEG should be depleted from the interface, except in the central region above which the cap layer is not etched. With the shallow mesa, it is possible to fabricate quantum wires with the confinement widths below 100 nm. [46]

Split Gates

This technique, which was first introduced by Thornton *et al.* [48] and Zheng *et al.* [49], uses two metallic strips on top of the heterostructure that work as gates. When a sufficiently negative bias (relative to the 2DEG) is applied to the gates, the 2DEG is depleted from the regions under the gates, leaving a central channel undepleted as shown in Fig. 1.2(c). The gate separations are typically on the 100 nm scale, and the width of the confined 2DEG can be even smaller. The split-gate technique does not degrade the electron mobility because the confinement is achieved by a smooth electrostatic potential. Also, the confinement width of the electrons can be changed conveniently by simply varying the gate voltage. Because of these advantages, quantum wires fabricated with the split-gate technique have been widely used in experimental studies [18, 19, 20, 22, 24].

To attach the metallic gates to the heterostructure, a fabrication procedure known as *lift-off* [50] is usually used. With a resist (PMMA) covering the central region of the heterostructure surface after the patterning process, a layer of metal (such as Au, Pt, or Ti) is evaporated onto the patterned surface. By dissolving the remaining resist, the metal on top of the resist is carried away (lifted off), and thus two metallic gates are formed on the heterostructure.

In patterning the resist (PMMA), electron-beam lithography is the best choice for producing a high resolution pattern. However, the electron-beam writing is very slow and thus the patterning process takes a relatively long time (compared to ion-beam lithography and optical lithography). To reduce the exposed surface area, quantum wires fabricated with the split-gate technique usually have a short length [18, 19, 20], which is comparable to the gate separation. These short split-gate quantum wires are also called *point contacts* or *quantum constrictions.* An important advantage of the short quantum wires is that they have less

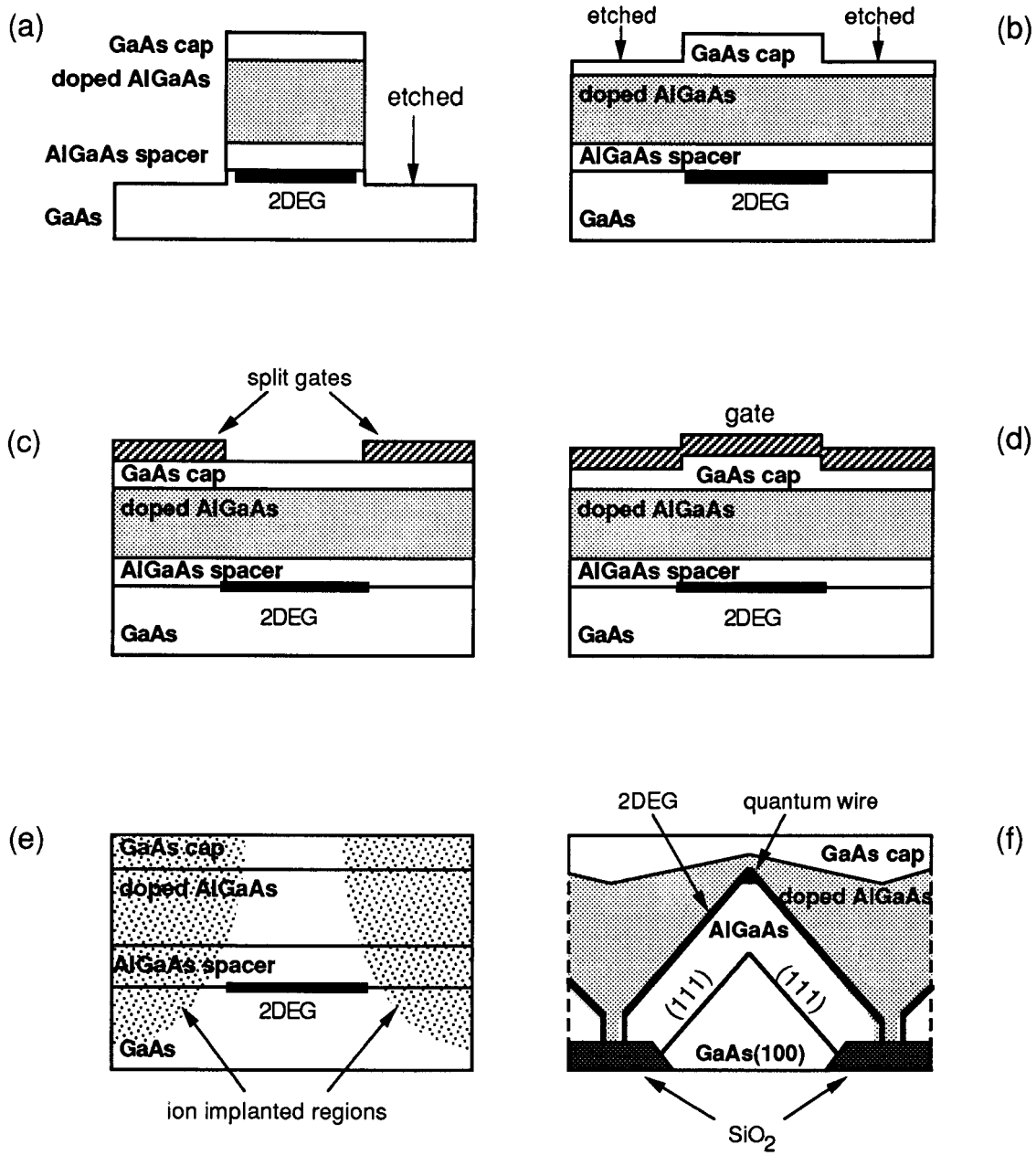

Figure 1.2: Cross-sections of quantum wires fabricated with the major confinement techniques. (a) Deep mesa selective etching. (b) Shallow mesa selective etching. (c) Split-gate technique. (d) Combination of split-gate technique and shallow mesa. (e) Ion implantation. (f) Selective epitaxy.

impurity scattering than long wires and therefore can display the confinement effect more clearly in experiments (see the next section). In theoretical studies, however, it is convenient for us to consider model quantum wires that are infinitely long; This simplification does not change qualitatively the basic properties of the quantum wires that are the topic of this thesis.

It is worth mentioning that the split-gate technique can have two interesting modifications. One [51] combines the split-gate and selective etching techniques: The heterostructure is first etched with shallow mesa then is covered by a layer of metal to work as gate (Fig. 1.2(d)). The other approach [39, 52, 53] uses a patterned organic or inorganic insulator as a gate dielectric to increase the separation between the gate and the 2DEG. This corresponds to replacing the unetched part of the cap in Fig. 1.2(d) by a dielectric.

Ion Implantation

This technique [38, 54, 55, 56] uses focused ion beams to implant high-energy ($\sim$100 keV) ions (such as Ga, Si, or Be) to induce crystal damage and doping in a well-controlled region. The ion exposure is always followed by sample annealing to activate the implanted ions and expand the damaged region. In quantum wires, a high dose of ions is implanted on both sides of the central region. Because the electron mobility is drastically reduced in the region implanted with ions, the electrons of the 2DEG are effectively confined to the central region, as shown in Fig. 1.2(e). With the ion implantation technique, it is possible to fabricate quantum wires even narrower than 100 nm [55, 56]. However, this technique has some uncertainty in the confinement width because the expansion range of the implanted ions after annealing is hard to control. Because the confined electrons of the 2DEG can be very close to the implanted ions, the electron mobility is definitely affected.

Selective Epitaxy

In contrast to the above techniques, the selective epitaxy accomplishes the heterostructure growth and the lateral confinement at the same time. [57] This technique is now widely used in fabricating quantum wires. [58, 59, 60, 61, 62, 63] Its fabrication process involves several steps. First, a strip pattern is developed on a GaAs substrate with a (100) surface, and the pattern is masked with an insulator such as SiO_2. (See Fig. 1.2(f).) Then, with OMCVD or MBE, GaAs is grown on the unmasked region to produce a triangular prism which has

the (111) facet sidewalls. (This is because the growth in the (100) direction is much faster than in the (111) direction.) The next step is to grow a thick layer of $Al_xGa_{1-x}As$ on the GaAs triangular prism, followed by a very thin (~5 nm) layer of GaAs. Finally, a doped $Al_xGa_{1-x}As$ layer and a GaAs cap layer are grown. In such a structure 2DEG is formed in the zigzagged GaAs layer between the two $Al_xGa_{1-x}As$ layers. By properly choosing the doping level and the thickness of the doped $Al_xGa_{1-x}As$ layer, electrons can be confined to the top corner of the GaAs layer and thus a quantum wire is realized. With this technique, it is possible to fabricate quantum wires with widths as small as 10 nm.

Besides the above techniques, other confinement methods such as intrinsic strain [64], lateral p-n junctions [65], gates in the 2DEG plane [66], and holographic illumination [67] have also been used to fabricate quantum wires.

According to above discussion, we can see that the width of the confined 2DEG is typically on the 100 nm scale. However, the Fermi wavelength of the 2DEG in GaAs-$Al_xGa_{1-x}As$ is typically 40 nm (see Table 1.1). Because the confinement width is comparable to the Fermi wavelength, the energy levels of the 2DEG in the confinement direction are quantized. Therefore, quantum wires are quasi-one-dimensional electronic systems.

1.3 Experimental Properties

In this section, we focus on the transport properties of quantum wires that are closely related to the topics of the theoretical studies of this thesis. However, for general reference, other major experimental properties are outlined at the end of this section.

Generally speaking, the transport properties of an electronic system are determined to a large extent by the electron scattering mechanisms involved. For a quantum wire, all temperature-dependent scattering (such as phonon scattering) at low temperatures ($T \leq 1$ K) is negligibly small and therefore the transport properties are only determined by impurity (dopant) scattering and boundary scattering. The competition between the impurity and boundary scatterings results in three transport regimes of the quantum wire. In the *diffusive regime*, the mean free path of electrons which depends on the impurity scattering is much smaller than the width of the quantum wire, and thus impurities are the dominant factor in the scattering. In the *ballistic regime*, on the other hand, the mean free path of the electrons is much larger than the width of the quantum wire, and thus boundary scattering

is the dominant factor. When the mean free path and the width of the quantum wire are comparable, the system is between the ballistic regime and the diffusive regime, and this regime is often called *quasi-ballistic regime.*

From the diffusive regime to the ballistic regime, quantum wires display many interesting transport properties. [9, 10] In the diffusive regime, the systems are disordered and are associated with *localization*, a concept first discussed by P. W. Anderson [69]. The disordered systems are characterized by a large electron backscattering produced by impurities, which involves quantum mechanical interference effects. [70] In this research field, several sophisticated theoretical techniques, such as scaling [71] and field theoretical methods [72], have been developed. There are many introductory reading [73, 74, 75] and review articles [70, 71, 76, 77] on various aspects of the disordered systems.

This thesis, however, is closely related to the ballistic transport properties of quantum wires. As described in the last section, the typical widths of quantum wires are on the 100 nm scale, while the mean free path of electrons at low temperatures ($T \leq 1$ K) is typically $10^2 - 10^4$ nm (see Table 1.1).[1] Therefore, it is quite possible to realize quantum wires whose widths are smaller than the mean free path of electrons, i.e., in the ballistic regime. Now we review the major ballistic transport properties of quantum wires.

1.3.1 Conductance Quantization

Conductance measurement is an important experimental method in studying quantum wires. Fig. 1.3(a) shows a schematic top view of the typical layout for conductance measurements on a split-gate quantum wire. The lightly shaded areas represent gate bars which have a width on the 1 μm scale. The heavily shaded areas represent the split gate with both the gate separation and width on the 100 nm scale. Boxes 1 and 2 with cross signs inside represent the ohmic contacts that are the source and drain of the 2DEG, respectively. (Note that experimental measurements usually use four terminals, but the two terminals for measuring current are not shown in Fig. 1.3(a).) When a sufficiently negative gate voltage V_g, i.e., the voltage between the gates and the 2DEG, is applied, electrons of the 2DEG are confined laterally as shown in Fig. 1.3(b). (Note that this is a case of a short quantum wire.) At the same time, if a voltage V_{sd} is applied between the source and drain of the 2DEG, an

[1] The mean free path of confined electrons is somewhat smaller than that for a true 2DEG because the confined electrons have a lower Fermi energy and because fabrication of confined electron systems inevitably introduces defects into the systems.

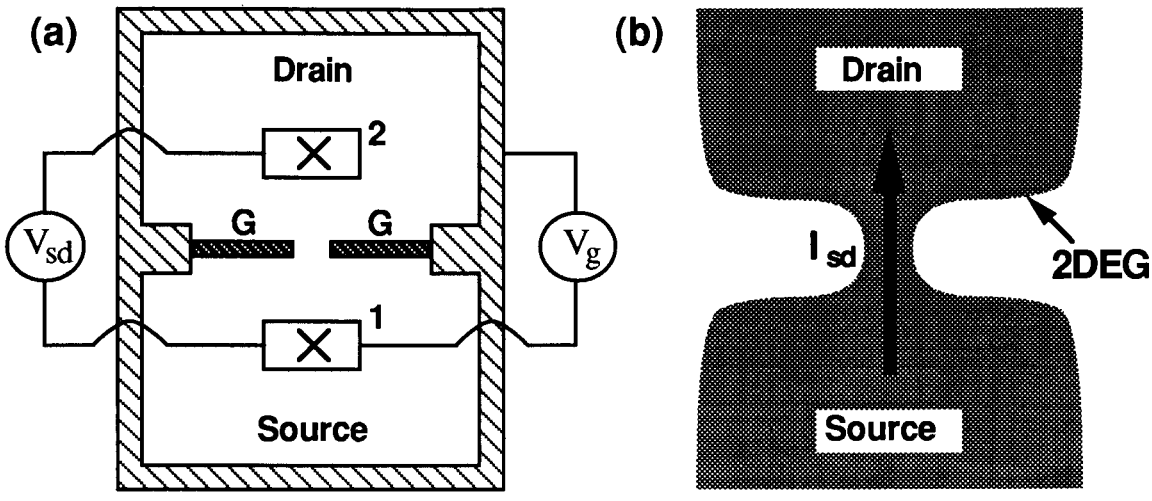

Figure 1.3: (a) The typical layout for conductance measurements on the split-gate quantum wires. Boxes 1 and 2 are the ohmic contacts with the source and drain of the 2DEG, respectively. V_g is a negative voltage applied between the gates and the 2DEG. V_{sd} is a voltage applied between the source and drain. (b) The confined 2DEG is indicated by shading.

electric current I_{sd} will flow from the source to the drain. By measuring I_{sd} and V_{sd} at low temperatures ($T \leq 1$ K), one can evaluate the conductance G and the resistance R of the short quantum wire through

$$G = \frac{1}{R} = \frac{I_{sd}}{V_{sd}}. \tag{1.5}$$

Low-temperature conductance measurements were first performed by van Wees *et al.* [18] and Wharam *et al.* [19] independently on short split-gate quantum wires. Both groups observed that the conductance and resistance display a series of plateaus as a function of the gate voltage. For illustration, we show in Fig. 1.4 typical resistance measurements on a short split-gate quantum wire measured by Sachrajda and collaborators at NRC. In Fig. 1.4, curve A is the resistance before the quantum wire is exposed to illumination, and curves B and C are the resistances after short and long illumination by a red light emitting diode (LED), respectively. At about $V_g = -0.33$ V, all of the resistances increase rapidly, which implies that the electrons have been depleted from the regions below the gates. This gate voltage is called the *depletion voltage*. As the gate voltage increases negatively further, the curves display a series of plateaus at about $h/2e^2$, $h/4e^2$, $h/6e^2$, etc. (After subtracting

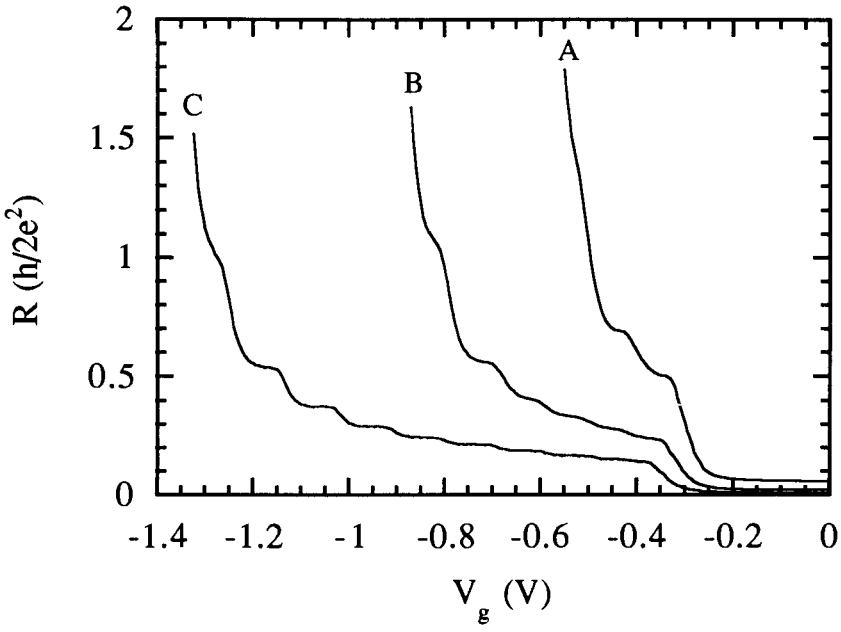

Figure 1.4: The resistance measurements on a split-gate quantum wire. Curves A, B, and C are the resistances of the quantum wire before illumination, after a short illumination, and after a long illumination, respectively. Data courtesy of Dr. Andrew S. Sachrajda and collaborators at the Institute of Microstructural Sciences, NRC, Canada.

the resistances at zero gate voltage due to the ohmic contacts, the plateaus will match these values better.) Every resistance curve finally rises up dramatically, which means that electrons are completely depleted and the quantum wire is pinched off. The gate voltage at which this happens is called the *pinchoff voltage* or *cutoff voltage*. The pinchoff voltages for curves a, b, and c are -0.55 V, -0.86 V, and -1.33 V, respectively.

The conductance or resistance curves of quantum wires can be affected by many factors. We list the major factors below.

1. *Illumination.* As shown in Fig. 1.4, the resistance curves before illumination, after a short illumination, and after a long illumination are substantially different from each other. This is because illumination converts deep donors into shallow donors which can donate their electrons to the quantum wire. Thus it increases the density of electrons in the quantum wire. A quantitative discussion on this will be given in Chapters 5 and 6.

2. *Temperature.* It is observed [78] that the resistance plateaus deteriorate gradually with increasing temperature, and that at moderately high temperatures ($T \sim 5$ K) the curves show a smooth behavior with the gate voltage.

3. *Wire length.* Quantum wires that display nice conductance plateaus are always very short, i.e., on the 100 nm scale. Experiments [79] have found that long quantum wires (~ 1 μm) do not display clear plateaus, because of the large possibility of backscattering due to impurities and the sidewall roughness of the wires. In short quantum wires the backscattering is suppressed significantly.

4. *Impurities.* Besides the backscattering, impurities can induce other conductance features of quantum wires, such as *transmission resonances* [22, 23] and time-dependent *random telegraphic signals* (RTSs) [24], even at very low temperature ($T \sim 0.1$ K).

5. *Magnetic field.* Although the conductance quantization itself does not require the presence of any magnetic field, a magnetic field can significantly reduce the backscattering and thus suppress the fluctuations in the conductance plateaus at low temperatures. [78]

6. *Gate geometry.* The detailed features of the conductance curves, such as the flatness of plateaus and the sharpness of transitions between plateaus depend also on the geometric shape of the split gate. [21] This is because the geometric shape of the split gate influences the confining potential well of quantum wires.

It is interesting to note the similarity between the conductance quantization of quantum wires and the quantum Hall effect [16, 17]. However, these are essentially different effects. The conductance quantization of quantum wires needs no magnetic field, while the quantum Hall effect requires a magnetic field. The conductance quantization of quantum wires is a property of ballistic transport, while the quantum Hall effect is associated with edge states and does not require the system to be in the ballistic regime. Finally, the accuracy of the conductance quantization of quantum wires (typically 1%) is much lower than that of the quantum Hall effect (typically 10^{-7}). The relatively lower accuracy for the conductance quantization of quantum wires is caused by both the ohmic connections that form resistances in series with the measured quantum wire and scattering from residual defects as well as tunneling effects. [10] Therefore, the physics in the conductance quantization of quantum wires must be different from that in the quantum Hall effect.

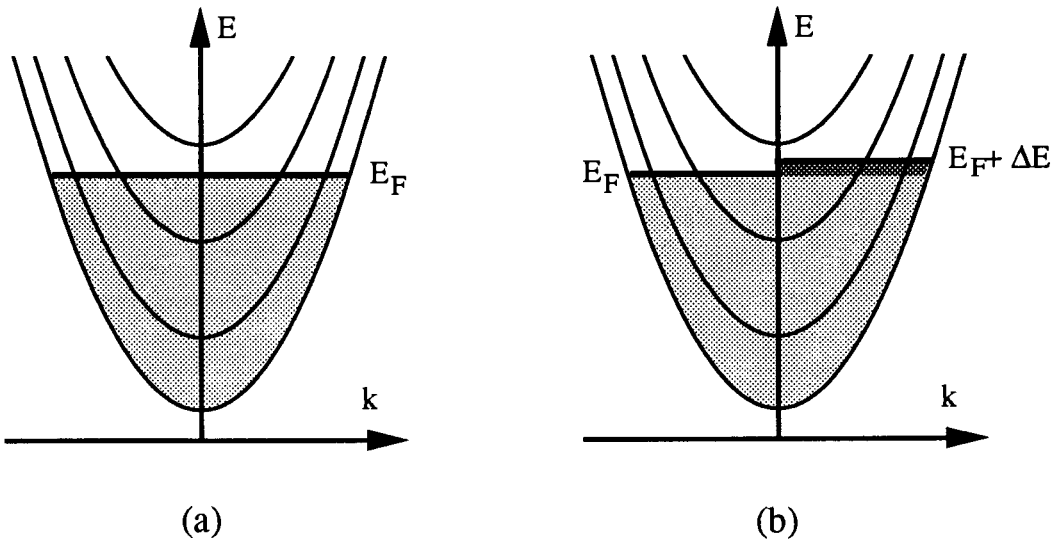

Figure 1.5: (a) The quantum wire has a uniform chemical potential (Fermi level) when $V_{sd} = 0$. (b) The chemical potential (Fermi energy) for electrons with $+k$ is higher than that for electrons with $-k$ when $V_{sd} \neq 0$. The net electric current between source and drain is given by the electrons in the heavily shaded region.

In fact, the conductance quantization can be understood in terms of a simple quantum mechanical argument for a ballistic one-dimensional electronic system. [78] Consider a quantum wire in which electrons move freely in the y-direction (the longitudinal direction) and energy levels are quantized in the x-direction (the transverse direction). Thus, an electron's energy can be expressed as

$$E_l(k) = E_l + \frac{\hbar^2 k^2}{2m^*}, \tag{1.6}$$

where E_l is the transverse energy level and k is the wavevector in the y-direction. When no voltage is applied between the source and drain, electrons have a uniform Fermi level as shown in Fig. 1.5(a). However, when a voltage V_{sd} is applied between the source and drain, the chemical potential (Fermi level) of electrons in the drain is lower than in the source by $\Delta E = eV_{sd}$, as shown in Fig. 1.5(b). Therefore, there are more electrons moving from the source to the drain (with $+k$) than electrons moving from the drain to the source (with $-k$). The net current at zero temperature is given by the electrons in the heavily shaded region in Fig. 1.5(b).

In the ballistic regime, the total electric current between source and drain corresponds

to the sum of contributions from all electrons in the heavily shaded region

$$I_{\rm sd} = e \sum_{E_l<E_{\rm F}} \int_{E_{\rm F}}^{E_{\rm F}+\Delta E} dE D_l(E) v_l(E), \tag{1.7}$$

where $D_l(E)$ is the density of states and $v_l(E)$ is the electron velocity for the lth transverse energy level. For one-dimensional systems, the density of states is given by

$$D_l(E) = 2\left(2\pi \frac{dE_l(k)}{dk}\right)^{-1}, \tag{1.8}$$

where the prefactor 2 comes from the spin degeneracy. The electron velocity is given by

$$v_l(E) = \frac{dE_l(k)}{\hbar dk}. \tag{1.9}$$

Substituting Eqs. (1.8) and (1.9) into Eq. (1.7), the k-dependences of the density of states and the electron velocity cancel. Thus,

$$I_{\rm sd} = 2e \sum_{E_l<E_{\rm F}} \frac{\Delta E}{h} = \frac{2e^2}{h} N_{\rm p} V_{\rm sd}, \tag{1.10}$$

where $N_{\rm p}$ is the number of transverse levels populated by electrons. According to equation (1.5), one obtains

$$G = \frac{2e^2}{h} N_{\rm p}. \tag{1.11}$$

In conductance measurements, when the gate voltage becomes more negative after the depletion voltage is reached, the quantum wire narrows and the transverse energy levels rise relative to the Fermi energy. Thus the number of populated transverse levels $N_{\rm p}$ decreases. Each time $N_{\rm p}$ decreases by one, the resistance rises to a new plateau. Finally, no transverse levels are populated by electrons and the quantum wire is pinched off. This analysis shows that the conductance quantization is a signature of one-dimensional electronic systems in the ballistic regime.

The conductance of quantum wires can be generally expressed in the form of a Landauer formula [80, 81, 82, 83] which is widely used in multi-channel transmission of waveguides

$$G = \frac{2e^2}{h} {\rm Tr}\ {\bf t}{\bf t}^\dagger = \frac{2e^2}{h} \sum_{n,m=1}^{N} |t_{nm}|^2, \tag{1.12}$$

where t_{nm} presents the transmission probability amplitude from channel n to channel m. Detailed discussions of the Landauer formula have been given in the literature [84, 85, 86].

The main complication for the realistic short wires is that the confining potential changes along the longitudinal direction rapidly. Therefore, the tunneling of evanescent states from one end of the short wire to the other would suggest a deviation from the exact quantization. Related to this question, many theoretical models [87, 88, 89] have been developed, involving solving the Schrödinger equation with different assumed confining potentials. These works show that the evanescent states tend to erode the quantization, but clear conductance plateaus are present even in quantum constrictions with similar length and width.

1.3.2 Correlations between Wires

To explore the electronic correlations between parallel quantum wires, many systems of parallel quantum wires have been fabricated and studied experimentally. [20, 90, 91, 92, 93] An important early experimental study was made by Smith *et al.* [20] on two short, parallel split-gate quantum wires. In their conductance measurements against the gate voltage (see Fig. 1.6), Smith *et al.* found that the total conductance shows successive "double" steps of $4e^2/h$. Curve A, which was the first measurement after the fabrication of sample, clearly shows the double steps $4e^2/h$ against gate voltage. Curves B, C, and D, which were later measurements, also show successive double steps $4e^2/h$. The single steps of $2e^2/h$ occurring in curves B, C, and D near the pinchoff voltage have been explained as being due to the successive pinchoff of the two quantum wires. It was found that the double steps $4e^2/h$ of conductance occurred on different occasions when the relative widths of the two quantum wires had changed due to the spontaneous rearrangement of charges in electronic traps in the device. Based on this fact, Smith *et al.* suggested that the double steps of $4e^2/h$ imply that the relative alignments of the transverse energy levels of the two quantum wires are not random but *correlated.* However, the reason for the correlation between the energy levels of the quantum wires was not known.

The $4e^2/h$ double steps of the conductance have also been observed in other systems of parallel quantum wires [91, 92]. In a recent experimental study, Simpson *et al.* [93] developed a system of two parallel quantum wires with a similar geometry to that used by Smith *et al.* [20], but with independent voltage control of each gate. Simpson *et al.* compared the total conductance of the two quantum wires to the sum of the two individual conductances. However, they found no evidence of alignments of the transverse energy levels of the two quantum wires. Therefore, the experimental situation at present is unclear.

It is worth mentioning that the conductance behavior of two quantum wires *in series* has

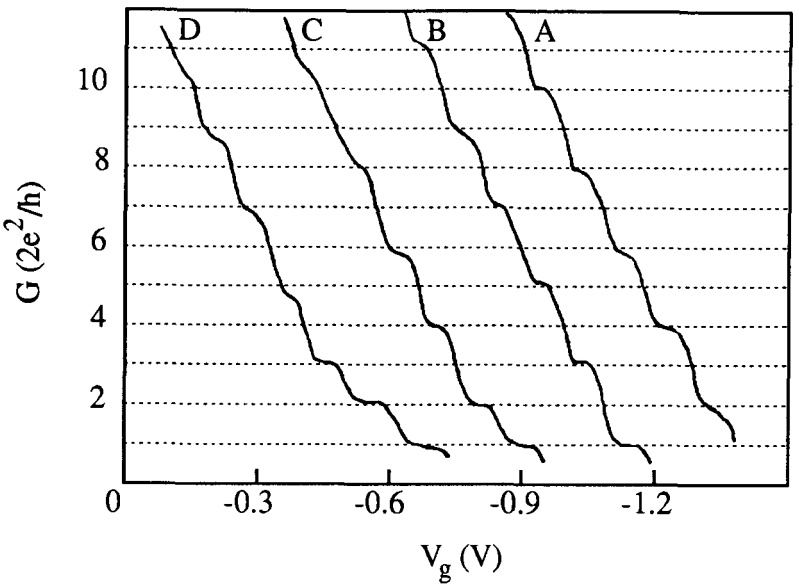

Figure 1.6: Conductance measurements on two parallel split-gate quantum wires against the gate voltage for different measurement situations. Curve A was the first measurement after the fabrication of sample. Curve B, which has been displaced by 0.2 V to the left for clarity, was a measurement on the following day. Curve C, displaced by another 0.2 V to the left, was a measurement on another date. Curve D, displaced by another 0.2 V to the left, was a measurement one month later. Data courtesy of Dr. Charles G. Smith. [20]

also been explored by many experimental groups. [94, 95, 96, 97, 98]. These experiments presented an anomalous (non-ohmic) resistance addition rule: the resistance of the series connection is smaller than the sum of the components. Such a behavior has been interpreted as being due to *adiabatic transmission* [99], which allows the transverse modes to evolve along the wires without mixing. In the completely adiabatic situation, the total resistance of the two quantum wires in series is given by the largest resistance of the two quantum wires [100], just as the resistance of a single quantum wire is determined by its width at the narrowest point. However, a semiclassical electron *collimitation effect* [100] is also believed to play an important role in the phenomena.

1.3.3 Other Properties

The quantum wires used in the above ballistic transport studies are relatively clean systems. However, many realistic quantum wires are in the quasi-ballistic regime and exhibit

significant impurity effects. For examples, it was observed [22] that the conductance of quantum wires exhibits transmission resonances at large gate voltages. Theoretical studies [23, 101, 102, 103, 104] showed that such transmission resonances can be explained by the electronic tunneling via a localized state that is associated with an attractive impurity inside quantum wires. This situation is similar to that of a double quantum barrier device where electrons are transmitted via a state localized in the intermediate region between the barriers.

Many quantum wires display conductance "dips" (sharp reduction) [105] or random telegraphic signals [24, 106, 107, 108, 109]. These effects are believed to be associated with single impurities changing their locations or ionization states.

Multiple impurity effects have been studied by several theoretical groups [110, 111, 112, 113]. In a recent numerical study, Davies *et al.* [113] used realistic screened ionized-impurity potentials to describe the background of a quantum wire, and found that the quantization of the conductance breaks down when impurity scattering is getting strong.

It has been found [21, 87, 88, 114, 115] that the geometry of quantum wires can also affect the conductance of quantum wires significantly. For example, a quantum wire with a "cavity" inside shows transmission resonances which are similar to those related to impurities. Here the resonance features are associated with the localized states of the cavity in the quantum wire.

Application of magnetic fields perpendicular to the 2DEG of a quantum wire can introduce several interesting effects. [78] When the magnetic fields are moderate ($B \leq 1$ T), fluctuations in the conductance plateaus are reduced because the magnetic fields reduce the impurity backscattering. When the magnetic fields are higher, the *magnetic depopulation* of subbands occurs. This effect produces progressively wider plateaus with well-quantized values, and smoothly makes the transition to the quantum Hall regime. For large fields ($B \geq 4$ T), additional plateaus at odd integer multiples of e^2/h are observed because of spin splitting. Note that the conductance quantization formula (1.11) should be valid for any type of subband structure.

Besides transport properties, other experimental approaches have also been used to study quantum wires, such as optical effects [116, 117], and dielectric response and plasmons [39, 118, 119, 120, 121].

1.4 Theoretical Review

Now we review briefly the theoretical studies of quantum wires. Because electrons in quantum wires are confined to a length scale that is comparable to the Fermi wavelength, the energy levels that are associated with the motion across the quantum wires are quantized. Therefore, quantum wires should be studied using quantum mechanics.

1.4.1 General Description

Consider a system of N confined electrons in a GaAs-$Al_xGa_{1-x}As$ quantum wire. The Schrödinger equation of the system is

$$-\frac{\hbar^2}{2m}[\nabla_1^2+\cdots+\nabla_N^2]\Psi_{\text{total}}(\{\mathbf{r}\})+V_{\text{total}}(\{\mathbf{r}\})\Psi_{\text{total}}(\{\mathbf{r}\})=E_{\text{total}}\Psi_{\text{total}}(\{\mathbf{r}\}), \quad (1.13)$$

where $\{\mathbf{r}\}=(\mathbf{r_1},\cdots,\mathbf{r_N})$ refer to the coordinates of N electrons, and $\Psi_{\text{total}}(\{\mathbf{r}\})$ and E_{total} are the total eigenfunction and eigenenergy of the system, respectively. The total potential energy $V_{\text{total}}(\{\mathbf{r}\})$ can be expressed as

$$V_{\text{total}}(\{\mathbf{r}\})=V_{\text{crystal}}(\{\mathbf{r}\})+V_{\text{ext}}(\{\mathbf{r}\})+V_{\text{int}}(\{\mathbf{r}\}), \quad (1.14)$$

where $V_{\text{crystal}}(\{\mathbf{r}\})$, $V_{\text{ext}}(\{\mathbf{r}\})$, and $V_{\text{int}}(\{\mathbf{r}\})$ are the contributions from the crystal potential which determines the band structure, from the external field which confines electrons, and from the electron-electron interactions, respectively.

In practical studies, equation (1.13) is simplified using different levels of approximation. The first level of approximation is the *effective mass approximation* [122, 123], which is almost always used. In this approximation, the wavefunctions of the system are expressed as products of Bloch wavefunctions that are associated with the crystal potential, and *envelope wavefunctions* that are associated with the slowly varying external potential and electron-electron interactions. In studying quantum wires, explicit treatment of the Bloch wavefunctions is usually not necessary (except for some phenomena such as optical absorption where the underlying Bloch wavefunctions are involved). The effects of the Bloch wavefunctions can be incorporated into the electron effective mass [122], and, as a result, we only need to deal with the envelope wavefunctions. Thus the Schrödinger equation becomes

$$-\frac{\hbar^2}{2m^*}[\nabla_1^2+\cdots+\nabla_N^2]\Psi_{\text{env}}(\{\mathbf{r}\})+[V_{\text{ext}}(\{\mathbf{r}\})+V_{\text{int}}(\{\mathbf{r}\})]\Psi_{\text{env}}(\{\mathbf{r}\})=E_{\text{env}}\Psi_{\text{env}}(\{\mathbf{r}\}), \quad (1.15)$$

where $\Psi_{\rm env}(\{\mathbf{r}\})$ and $E_{\rm env}$ are the envelope wavefunction and its corresponding eigenenergy, respectively. Note that the effective mass m^* corresponds to the value at the conduction band minimum of GaAs.

Generally speaking, it is not possible to solve the many-particle form of the Schrödinger equation (1.15) analytically because of the interaction term $V_{\rm int}(\{\mathbf{r}\})$. An interesting exception that is worth mentioning is the so-called *Luttinger liquid model* [124, 125, 126], which describes strictly one-dimensional electronic systems that have a linear energy dispersion against wavevector. The Hamiltonian of the Luttinger liquid model is analytically solvable, and the excitations of electrons are more appropriately described by a picture of bosons instead of fermions. This model was first used to study the conductivity of one-dimensional organic solids [124], and was recently suggested [127] for tunneling conductance of a quantum Hall state. Recently, some experiments [128] suggested that ideal one-dimensional semiconductor quantum wires in the domain of low energy excitations may be Luttinger liquids. However, the experimental evidence [128] is not clear enough and further experiments on such systems would be of interest. In this thesis, we will still use the Fermi liquid theory to study quantum wire systems.

For convenience of calculations, we will approximate the many-particle form of the Schrödinger equation (1.15) by the single-particle form

$$-\frac{\hbar^2}{2m^*}\nabla^2\Psi_{\rm env}(x,y,z)+[V_{\rm ext}(x,y,z)+V_{\rm int}(x,y,z)]\Psi_{\rm env}(x,y,z)=E_{\rm env}\Psi_{\rm env}(x,y,z), \quad (1.16)$$

where $\Psi_{\rm env}(x,y,z)$ and $E_{\rm env}$ are the effective envelope wavefunction and its corresponding energy for one particle. The many-particle effects are included (in a mean field approximation) in the interaction term of the potential energy $V_{\rm int}(x,y,z)$. In other words, the potential energy $V_{\rm int}(x,y,z)$ should now include the regular Coulomb energy and the energies of exchange and correlation. There are several treatments for the interaction term $V_{\rm int}(x,y,z)$, which form the second level-approximations.

1. *The Independent particle approximation.* This approximation simply neglects the interaction term $V_{\rm int}(x,y,z)$ completely. The Schrödinger equation (1.16) can therefore be solved analytically for simple forms of $V_{\rm ext}(x,y,z)$. It is possible to generalize this approximation slightly to include some effect of interactions by adjusting the external potential term $V_{\rm ext}(x,y,z)$. The independent particle approximation is useful for qualitative discussion, but its accuracy is not good and all of the information on interactions is lost.

2. *Thomas-Fermi method.* While neglecting the energies of exchange and correlation, the Thomas-Fermi method [129] includes the Coulomb energy but assumes that the kinetic energy relates to the local electron density. The Poisson equation can therefore be expressed in terms of the potential function and thus becomes easier to be solved. This method is particularly useful for calculating the ground-state density distribution of electrons if the density of electrons is slowly varying.

3. *The Hartree approximation.* This approximation includes the direct Coulomb interaction and treats the kinetic energy correctly but neglects the exchange-correlation energies. The Schrödinger equation is reduced to the single-particle form with the Coulomb interaction being expressed in the simplest mean field form. The screening effect of electrons is reflected by this approximation, and the accuracy of calculations is much improved. However, the Schrödinger equation in the Hartree approximation can only be solved numerically. For low-dimensional systems, the Hartree approximation, although often useful [130, 131], can be inaccurate because the exchange-correlation effects tend to be stronger in low dimensions [132].

4. *The Hartree-Fock approximation.* This approximation improves the Hartree approximation by including both the Coulomb interaction and the exchange interaction. It is appropriate for systems with a few electrons such as quantum dots. [133, 134]

5. *The density functional theory.* This theory [136, 137] includes completely the Coulomb interaction, and the exchange-correlation effects. In this theory, the many-particle Schrödinger equation reduces to a single-particle form by including the exchange-correlation energies in an effective potential energy, which is a functional of the electron density. However, numerical calculations are usually done in the *local density approximation* (LDA), which relates the exchange-correlation energies to the local electron density. With similar calculation procedures to those used in the Hartree approximation, the density functional theory is very powerful and provides much more accurate results. The main shortcoming of the density functional theory is that it works reliably only for the ground states of many-particle systems. [138] More discussion of the density functional theory is given Chapter 5 and the Appendix.

1.4.2 Analytic Studies

Let us consider a quantum wire in which electrons can move freely in the y-direction but are confined in the x- and z-directions. In the independent particle approximation, the Schrödinger equation becomes

$$-\frac{\hbar^2}{2m^*}\left[\frac{d^2}{dx^2}+\frac{d^2}{dy^2}+\frac{d^2}{dz^2}\right]\Psi_{l_xkl_z}(x,y,z)+V_{\rm ext}(x,z)\Psi_{l_xkl_z}(x,y,z)=E_{l_xkl_z}\Psi_{l_xkl_z}(x,y,z), \tag{1.17}$$

where $\Psi_{l_xkl_z}(x,y,z)$ and $E_{l_xkl_z}$ are the wavefunction[2] and energy for eigen state (l_x,k,l_z), respectively. Here l_x and l_z are the quantum numbers associated with the x-direction and z-direction confinements, respectively, and k is the wavevector of electron in the y-direction. Because $V_{\rm ext}(x,z)$ is y-independent, the wavefunctions can be separated as

$$\Psi_{l_xkl_z}(x,y,z)=\Phi_{l_xl_z}(x,z)e^{iky}, \tag{1.18}$$

$$E_{l_xkl_z}=E_{l_xl_z}+\frac{\hbar^2k^2}{2m^*}, \tag{1.19}$$

where the transverse eigenfunction $\Phi_{l_xl_z}$ and eigenenergy $E_{l_xl_z}$ are solutions of

$$-\frac{\hbar^2}{2m^*}\left[\frac{d^2}{dx^2}+\frac{d^2}{dy^2}\right]\Phi_{l_xl_z}(x,z)+V_{\rm ext}(x,z)\Phi_{l_xl_z}(x,z)=E_{l_xl_z}\Phi_{l_xl_z}(x,z). \tag{1.20}$$

However, equation (1.20) is still difficult to solve analytically because the external potential energy $V_{\rm ext}(x,z)$ depends on the details of the lateral confinement and can be very complicated. Therefore, a third level of approximations is used to simplify $V_{\rm ext}(x,z)$. For examples, $V_{\rm ext}(x,z)$ can be taken to have a circular, rectangular, or other types of geometry [139], whichever is suitable for the realistic situation being considered.

For quantum wires fabricated by laterally confining the 2DEGs in GaAs-$Al_xGa_{1-x}As$ heterostructures (see Fig. 1.1), a convenient way is to discuss the energy quantization in the x- and z-direction separately. Qualitatively speaking, the z-direction confinement is related to the conduction band offset, electrostatic attraction of the positive charges of the ionized donors, and mutual-screening of electrons. A widely used approximation for the z-dependent confining potential is a triangular well

$$V(z)=\begin{cases}\infty, & z\le L\\ eFz, & z>L\end{cases} \tag{1.21}$$

[2]Below we simplify the "envelope wavefunctions" as "wavefunctions" and omit the subscript "env".

where F is the electric field in the triangular well. Substituting equation (1.21) into (1.20), the wavefunctions obtained are Airy functions and the energy levels are [135]

$$E_{l_z} = (\frac{9}{2m^*})^{1/3} \left[\pi e\hbar F(l_z + \frac{3}{4})\right]^{2/3}, \; l_z = 0, 1, 2, \cdots \tag{1.22}$$

In a real quantum wire, however, the electric field varies along the z-axis (see Figure 1.1). A reasonable approximation for F is the average value of the real electric field over the region to which the electrons are confined. The average field can be taken as the value of the field at z' at which there are equal numbers of electrons with $z < z'$ and $z > z'$. Thus,

$$F = \frac{en}{2\varepsilon\varepsilon_0}, \tag{1.23}$$

where n is the area density of electrons of the 2DEG.

Combining equations (1.22) and (1.23), we can estimate the energy intervals between the quantized levels for the z-direction

$$\Delta E_z \sim \left[\frac{\pi^2 e^4 \hbar^2 n^2}{m^* \varepsilon^2 \varepsilon_0^2}\right]^{1/3} \sim 40 \text{ meV}, \tag{1.24}$$

where we have used the parameter values given in Table 1.1. Note that the energy spacing ΔE_z is much less than the GaAs-$Al_xGa_{1-x}As$ conduction band offset $\Delta E_c \sim 0.2$ eV. Therefore, the triangular well is a reasonably good approximation for low and moderate electron densities at which just one or two quantized levels associated with the z-direction are populated, which is the usual case for GaAs-$Al_xGa_{1-x}As$ quantum wires.

The x-direction confinement can be handled in a similar way. The simplest approximation for $V(x)$ is an infinite square well

$$V(x) = \begin{cases} \infty, & x \leq 0 \\ 0, & 0 < x < a \\ \infty, & x \geq a \end{cases} \tag{1.25}$$

where a is the characteristic width of the quantum wire. The corresponding wavefunctions and energy levels are

$$\Phi_{l_x}(x) = \sqrt{\frac{2}{a}} \sin(\frac{\pi l_x x}{a}), \tag{1.26}$$

$$E_{l_x} = \frac{\pi^2 \hbar^2 l_x^2}{2m^* a^2}, \tag{1.27}$$

where $l_x = 1, 2, \cdots$. If we use $a \sim$100 nm, the energy intervals between the quantized levels for the x-direction are typically

$$\Delta E_x \sim \frac{\pi^2 \hbar^2}{m^* a^2} \sim 1 \text{ meV}. \tag{1.28}$$

Based on the above analytic discussion, we conclude that

$$\Delta E_x \ll \Delta E_z. \tag{1.29}$$

Because of this, the z-degree of freedom is effectively frozen out. Therefore, under normal conditions, we only need to consider the motion of electrons in the x and y directions. As we will see, this conclusion is important for our theoretical modeling for the numerical studies of quantum wires.

However, in realistic quantum wires, the potentials that confine electrons laterally are similar to neither the infinite square nor parabolic wells. In split-gate quantum wires, for example, the confining potential in principle should be found by solving the Poisson equation numerically within the heterostructure of a quantum wire ($z \geq 0$), with appropriate boundary conditions. [131] Because numerical calculations are usually complicated, many theoreticians [141, 142, 143, 144, 145, 146] have been trying to formalize the confining potentials. Moreover, an analytic description of the confining potentials is very useful for experimentalists to improve device performance, because the analytic description can reflect the effects of various parameters of quantum wires in a direct way. However, it turns out that the confining potentials depend on many factors of quantum wires, such as the conduction band offset, the surface Schottky barrier, and space charge distributions. We will come back to discuss this issue with more details in Chapters 5 and 6.

1.4.3 Numerical Studies

When electron-electron interactions are taken into consideration, the electronic structure of quantum wires needs to be calculated numerically. To date many numerical studies of quantum wires have been made, using the Thomas-Fermi method [147, 148, 149], in the Hartree approximation [130, 131, 150, 151], in the Hartree-Fock approximation [152], and in the density functional theory [153].

In numerical studies of quantum wires, it is important to note that the wave functions and the electron-electron interaction energy depend on each other. In other words, to solve

the Schrödinger equation (1.16) we need to know $V_{\rm int}(x,y,z)$, but $V_{\rm int}(x,y,z)$ depends on the wave functions which should be obtained by solving the Schrödinger equation. An effective technique for dealing with such problems is that of *self-consistent calculations*. In a self-consistent calculation, one assumes a suitable form of $V_{\rm int}(x,y,z)$ as a trial function. With the assumed $V_{\rm int}(x,y,z)$ and the already known $V_{\rm ext}(x,y,z)$, which is determined by external conditions, equation (1.16) is solved numerically. Then, using the wavefunctions obtained by solving the Schrödinger equation, $V_{\rm int}(x,y,z)$ is recalculated. With this newly calculated $V_{\rm int}(x,y,z)$ the Schrödinger equation is solved again. Such iterations are repeated until both $V_{\rm int}(x,y,z)$ and the wavefunctions no longer change significantly. The stable $V_{\rm int}(x,y,z)$ and wavefunctions are therefore the numerical solution of the problem.

Self-consistent calculations of the electronic structure were first performed by Laux and Stern [130] for a quantum wire based on Si-SiO_2 MOSFET, and later by several groups [131, 150, 151] for split-gate quantum wires that are based on GaAs-$Al_xGa_{1-x}As$ heterostructures. All of these calculations were in the Hartree approximation. The typical calculated electronic structure was given by the calculation of Laux *et al.* [131]. This calculation demonstrated that the lateral confining potential resembles a parabola but with a *flattened* bottom, which implies that there is a strong self-screening of the electrons in the quantum wire. When the gate voltage becomes more negative, the number of the populated transverse levels decreases gradually until the quantum wire is pinched off. This calculation also showed that the energy spacings of the quantized levels in the x-direction (due to the lateral confinement) are typically below 5 meV, while the energy spacings of the quantized levels in the z-direction (due to the attraction of the positively charged ionized donors) are much larger. This agrees with the conclusion obtained from our analytic discussion above.

Because of the omission of exchange-correlation effects, the Hartree approximation is not accurate enough to describe some features of quantum wires correctly. In early studies [132], the exchange and correlation energies were found to be very important in low-dimensional systems. Therefore, the exchange and correlation effects should play an important role in quantum wires which are low-dimensional systems. Here it is interesting to mention that recent numerical studies [133, 134] show that the many-body effects are comparable to the Hartree energy in quantum dots.

Some numerical studies have been made of quantum wires beyond the Hartree approximation. Using the Hartree-Fock approximation, Nakamura *et al.* [152] studied the exchange interaction in a restricted basis and found the exchange interaction to be quite strong.

Recently, Ravaioli *et al.* [153] took both the exchange and correlation interactions into account in their numerical calculation. However, their main focus was on studying the coupling effects of parallel quantum wires by inspecting the behavior of wavefunctions, while the relation between many-body effects and the electronic structure was not sufficiently investigated.

It should be mentioned that, in solving the Poisson equation in the above numerical studies, different boundary conditions have been used for the exposed surface of split-gate quantum wires. The proper choice of the boundary conditions at the exposed surface is a difficult issue because this involves the complicated surface properties, which are very complicated. An interesting discussion of this has been given recently by Chen *et al.* [149]. We will return to the problem of the boundary conditions in Chapter 6.

Chapter 2

Basis of Numerical Calculations

This chapter provides the basis for the numerical calculations to be presented in the next two chapters. In this chapter, we first introduce the *Coulomb-confined quantum wires*, which are the model used in our numerical calculations. Then we apply the density functional theory to electrons in a Coulomb-confined quantum wire, and obtain the equations based on which the numerical calculations are performed. Finally, we describe the procedures of the self-consistent calculation as well as important numerical techniques that are used in the programming.

2.1 Coulomb-Confined Quantum Wires

The structure of a single Coulomb-confined quantum wire is shown in Fig. 2.1. In such a structure, electrons are donated by a uniform ribbon of donors that is infinitely long in the y-direction and has a width w. The donated electrons are confined to the xy-plane (called the *electron plane*), which is separated from the donor ribbon by a distance d. The whole system is embedded in a uniform dielectric and is charge-neutral. In this system, electrons are confined in the x-direction (the lateral direction) because of the attractive Coulomb interactions between the electrons and the donor ribbon.

A Coulomb-confined quantum wire can be regarded as an idealization of a realistic quantum wire that is realized in a GaAs-$Al_xGa_{1-x}As$ heterostructure. The electron plane in the Coulomb-confined quantum wire represents the GaAs-$Al_xGa_{1-x}As$ interface at which a 2DEG is formed in the realistic quantum wire (refer to Fig. 1.1 and Fig. 1.2). Correspondingly, the donor ribbon represents the ionized donors in the doped $Al_xGa_{1-x}As$ layer, and

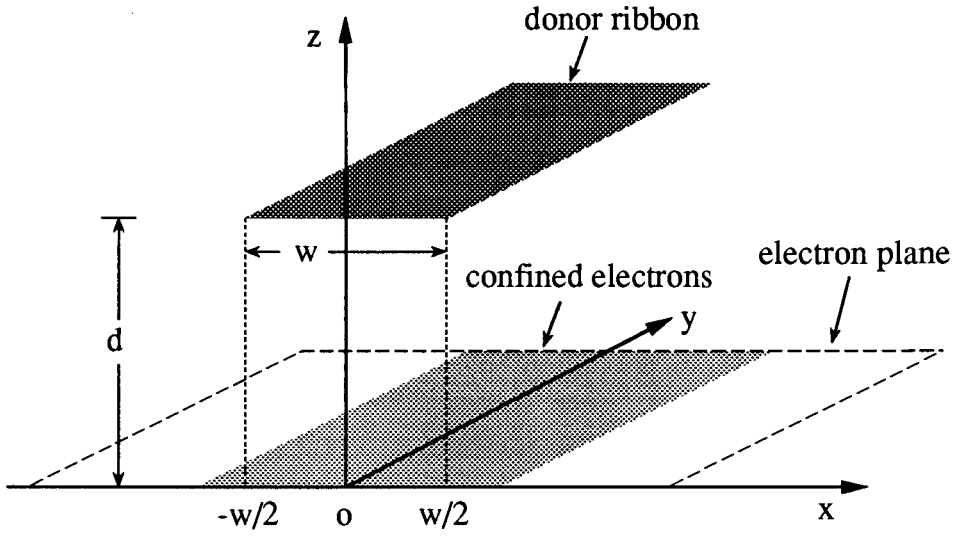

Figure 2.1: The schematic structure of a single Coulomb-confined quantum wire. The donor ribbon is infinitely long in the y-direction and has a width w. Electrons donated by the donors are confined to the xy-plane, which is separated from the donor ribbon by a distance d. The whole system is embedded in a uniform dielectric and is charge-neutral.

the separation d between the electron plane and the donor ribbon reflects the thickness of the undoped $Al_xGa_{1-x}As$ spacer in the realistic quantum wire.

Here we should make a remark regarding the model of Coulomb-confined quantum wires. In realistic GaAs-$Al_xGa_{1-x}As$ quantum wires, the ionized donors are in fact present within the whole region of the doped $Al_xGa_{1-x}As$ layer instead of only in a central region. However, when electrons are confined laterally in the realistic quantum wires, the electrostatic effect of the ionized donors far away ($|x| >> w$) on the confined electrons is effectively cancelled by that of surface or interface electrons far away ($|x| >> w$). For example, in a quantum wire fabricated with shallow mesa (see Fig. 1.2(b)), the electrostatic effect of the ionized donors under the etched surface is effectively cancelled by that of the electrons at the etched surface. Similarly, in a split-gate quantum wire (see Fig. 1.2(c)), the effect of the ionized donors under the gate is effectively cancelled by that of the electrons at the interface of the gate and GaAs cap layer. (More discussion of this issue will be given in Chapters 5.) In other words, the ionized donors that affect the confined electrons are only those in the central region. This is why we have used a donor "ribbon" in our model to represent the ionized donors (plus surface or interface electrons, to be exact) in the realistic quantum wire.

Note, however, that it should be possible to fabricate quantum wires in which the donors are indeed confined to a ribbon in space as we have assumed, although, to our knowledge, this has not been done to date.

Another remark is about the electron plane in the Coulomb-confined quantum wire. In realistic quantum wires, electrons are not constricted to an ideal plane but can be present within a short range ($\sim$ 5 nm [131]) in the z-direction. The electron distribution within this short range in the z-direction can be obtained by using a triangular potential well which has been described in Sec. 1.4. Based on both the relationship (1.29) of our analytic discussion in Sec. 1.4 and previous numerical calculations [131], the energy spacings between the quantized energy levels in the x-direction are much smaller than those between the quantized energy levels in the z-direction. This means that, in normal situations, we only need to consider the quantized energy levels in the x-direction, because different quantized energy levels in the z-direction are involved only when the electron density is very high ($n > 10^{12}$ cm^{-2}). When we discuss the situations in which the density of electrons is not very high, we can neglect the dependence of electrons on the z-direction and simply assume that the electrons are confined to a plane.

In numerical studies, the model of Coulomb-confined quantum wires has several advantages. First, this model avoids the practical complication that the lateral confinement of electrons is affected by many factors in realistic quantum wires. For example, in a split-gate quantum wire, the lateral confinement of electrons involves the properties of donors, the surface Schottky barrier, the conduction band offset, geometrical parameters, and external factors such as illumination. Studies of the effects of these factors are certainly important, and are the central topic of Chapters 5 and 6, but directly including all of these factors would make numerical calculations very cumbersome. The model of Coulomb-confined quantum wires can be viewed as a simple way of representing the net effect of all of these realistic factors. In this way, the numerical calculations are much simplified. The second advantage of the Coulomb-confined model is that the model can mimic the realistic processes of varying the gate voltage in split-gate quantum wires by changing the linear density of the donors and electrons while keeping the whole system to be charge-neutral. The numerical results calculated within the Coulomb-confined model can therefore be used to understand qualitatively the experimental properties observed in realistic split-gate quantum wires. Finally, with the simple physical picture provided by the Coulomb-confined model, we can more easily concentrate on some complicated but intrinsic properties of quantum wires, such as

the many-body effects.

2.2 Application of the Density Functional Theory

The density functional theory developed by Hohenberg, Kohn, and Sham [136, 137] provides an accurate treatment of the many-body effects that influence the ground state properties of inhomogeneous electronic systems. (The general formalism of the Hohenberg-Kohn-Sham density functional theory is described in the Appendix.) In the Hohenberg-Kohn-Sham density functional theory (referred to as "the density functional theory" below), the effective Schrödinger equation for an electron in a Coulomb-confined quantum wire is

$$-\frac{\hbar^2}{2m^*}\left[\frac{d^2}{dx^2}+\frac{d^2}{dy^2}\right]\Psi_{\ell k}(x,y)+V_{\rm eff}[n;x]\Psi_{\ell k}(x,y)=E_{\ell k}\Psi_{\ell k}(x,y), \tag{2.1}$$

where $\Psi_{\ell k}(x,y)$ and $E_{\ell k}$ are the eigenfunction and eigenenergy, respectively, m^* is the effective mass of electron, and $V_{\rm eff}[n;x]$ is the *effective potential energy* which is a functional of the electron density $n(x)$. (Note that our system is uniform in the y-direction.) The effective potential energy $V_{\rm eff}[n;x]$ is given by

$$V_{\rm eff}[n;x]=V_{\rm c}(x)+\mu_{\rm xc}[n], \tag{2.2}$$

where $V_{\rm c}(x)$ is the *Coulomb energy* (also called *Hartree energy*), and $\mu_{\rm xc}[n]$ is given by

$$\mu_{\rm xc}[n]=\frac{\delta E_{\rm xc}[n]}{\delta n}, \tag{2.3}$$

where $E_{\rm xc}[n]$ is the total *exchange and correlation energy* of the system.

According to Kohn and Sham [137], $E_{\rm xc}[n]$ can generally be expanded as

$$E_{\rm xc}[n]=\int d\mathbf{r}[\epsilon_{\rm xc}(n(\mathbf{r}))n(\mathbf{r})+\epsilon_{\rm xc}^{(2)}(n(\mathbf{r}))|\nabla n(\mathbf{r})|^2+\cdots]. \tag{2.4}$$

When the electron density $n(\mathbf{r})$ varies slowly in space, we can omit all the gradient terms and keep only the first term in Eq. (2.4), that is,

$$E_{\rm xc}[n]=\int d\mathbf{r}\epsilon_{\rm xc}(n(\mathbf{r}))n(\mathbf{r}). \tag{2.5}$$

Substituting Eqs. (2.3) and (2.5) into Eq. (2.2), we obtain

$$V_{\rm eff}(x)=V_{\rm c}(x)+\frac{d}{dn}[\epsilon_{\rm xc}(n(x))n(x)]. \tag{2.6}$$

The above treatment of omitting all gradient terms in Eq. (2.4) is called the *local density approximation* (LDA). The local density approximation has been very successful in studying the ground state properties of many-body systems, such as atoms, molecules, and crystalline solids. [157] We will use the local density approximation in our calculations.

It is interesting to note that, if we neglect $E_{\rm xc}[n]$ completely, the effective potential energy contains only the Coulomb energy $V_{\rm c}(x)$. This treatment is the so-called *Hartree approximation.*

In the local density approximation, the exchange-correlation energy becomes a function of position. For convenience of discussion, $\epsilon_{\rm xc}$ is usually separated as

$$\epsilon_{\rm xc} = \epsilon_{\rm x} + \epsilon_{\rm c}, \tag{2.7}$$

where $\epsilon_{\rm x}$ and $\epsilon_{\rm c}$ correspond to the exchange energy and correlation energy per electron, respectively. After doing this, Eq. (2.6) can be written as

$$V_{\rm eff}(x) = V_{\rm c}(x) + \mu_{\rm x}(x) + \mu_{\rm c}(x), \tag{2.8}$$

where

$$\mu_{\rm x}(x) = \frac{d}{dn}[\epsilon_{\rm x}(n(x))n(x)], \tag{2.9}$$

and

$$\mu_{\rm c}(x) = \frac{d}{dn}[\epsilon_{\rm c}(n(x))n(x)], \tag{2.10}$$

are contributions of the exchange and correlation energies to the effective potential energy $V_{\rm eff}(x)$, respectively.

In the local density approximation, once the electron density is known, the contributions of the exchange and correlation energies to the effective potential energy $V_{\rm eff}(x)$, as displayed in Eq. (2.8), can be calculated. For a 2DEG, $\epsilon_{\rm x}$ has the following analytic form [154]

$$\epsilon_{\rm x}(n) = -\frac{8\sqrt{2}}{3\pi r_s} = -\frac{8a_B^*}{3\pi}\sqrt{2\pi n}, \tag{2.11}$$

in which $a_{\rm B}^* = 4\pi\varepsilon\varepsilon_0\hbar^2/(m^*e^2)$ is the effective Bohr radius, where ε is the dielectric constant and m^* is the effective mass of electron, and $r_s = a/a_{\rm B}^*$, where $a = 1/(\pi n)^{1/2}$ corresponds to the average radius of the space occupied by each electron. Note that the energy unit of Eq. (2.11) is the effective Rydberg, which is defined as 1 Ryd* $= m^*e^4/2(4\pi\varepsilon\varepsilon_0\hbar)^2$. If we use $\varepsilon = 12.5$ and $m^* = 0.067\ m_e$, which are the values for a GaAs-$Al_xGa_{1-x}As$ quantum wire, then $a_{\rm B}^* = 98.7$ (Å) and 1 Ryd$^* = 5.83 \times 10^{-3}$ (eV).

The correlation energy ϵ_c for 2DEGs has been calculated numerically by various authors such as Jonson [155], and Tanatar and Ceperly [156]. The numerical results given by these authors are similar. In our calculations, we use the correlation energy calculated by Tanatar and Ceperly [156]

$$\epsilon_c(n) = \frac{a_0(1 + a_1 r_s^{1/2})}{1 + a_1 r_s^{1/2} + a_2 r_s + a_3 r_s^{3/2}}, \tag{2.12}$$

where

$$r_s = \frac{a}{a_B^*} = \frac{1}{a_B^*(\pi n)^{1/2}}. \tag{2.13}$$

The coefficients are $a_0 = -0.3568$, $a_1 = 1.1300$, $a_2 = 0.9052$, and $a_3 = 0.4165$, which are fitted in the range $1 < r_s < 50$. For 2DEGs in GaAs-$Al_xGa_{1-x}As$ quantum wires, the electron density $n(x)$ is typically in the range of $10^{10} - 10^{12}$ cm^{-2}, which corresponds to 10^2 (Å) $< a < 10^3$ (Å), or $1 < r_s < 10$. Therefore, Eq. (2.12) is valid for the quantum wire systems.

For the Coulomb-confined quantum wire shown in Fig. 2.1, the area density of donors is described by

$$n_d(x) = \begin{cases} \sigma, & \text{if } -w \le x \le w \\ 0, & \text{otherwise} \end{cases} \tag{2.14}$$

where σ is a positive constant. Therefore, the Coulomb energy $V_c(x, y)$ can be calculated directly from

$$V_c(x) = \frac{e^2}{4\pi\varepsilon\varepsilon_0} \int_{-\infty}^{\infty} dx' \int_{-\infty}^{\infty} dy' \left[\frac{n(x')}{\sqrt{(x - x')^2 + y'^2}} - \frac{n_d(x')}{\sqrt{(x - x')^2 + y'^2 + d^2}} \right], \tag{2.15}$$

where we have chosen $V_c(x)$ to be zero at $x = \pm\infty$. After performing the integration over y', Eq. (2.15) becomes

$$V_c(x) = \frac{e^2}{4\pi\varepsilon\varepsilon_0} \int_{-\infty}^{\infty} dx' \left\{ n(x') \ln[(x - x')^2] - n_d(x') \ln[(x - x')^2 + d^2] \right\}. \tag{2.16}$$

With both the exchange-correlation energy ϵ_{xc} and the Coulomb energy $V_c(x)$ known, the effective potential energy $V_{eff}(x)$ can be calculated from Eq. (2.8) and therefore the effective Schrödinger equation (2.1) can be solved. Considering that our system is uniform in the y-direction, the two-dimensional Eq. (2.1) can be reduced to the one-dimensional form

$$-\frac{\hbar^2}{2m^*} \frac{d^2}{dx^2} \Phi_\ell(x) + V_{eff}[n; x]\, \Phi_\ell(x) = E_\ell \Phi_\ell(x), \tag{2.17}$$

with

$$\Psi_{\ell k}(x,y) = \Phi_\ell(x)e^{iky}, \tag{2.18}$$

and

$$E_{\ell k} = E_\ell + \frac{\hbar^2 k^2}{2m^*}, \tag{2.19}$$

where E_l and $\Phi_l(x)$ are the eigen transverse energy level and eigenfunction, respectively, and k is the wave vector in the y-direction.

At zero temperature, the area electron density $n(x)$ relates to the transverse wavefunctions through

$$n(x) = 2 \sum_{\ell,k,E_\ell \le E_F} |\Psi_{\ell k}(x,y)|^2, \tag{2.20}$$

where E_F is the Fermi energy, and the prefactor 2 is for the spin degeneracy. After performing the summation over k, Eq. (2.20) becomes

$$n(x) = \frac{2}{\pi}\sqrt{\frac{2m^*}{\hbar^2}} \sum_{\ell,E_\ell \le E_F} \sqrt{E_F - E_\ell}|\Phi_\ell(x)|^2. \tag{2.21}$$

If we integrate over x on both sides of Eq. (2.21), we obtain

$$\eta = \int_{-\infty}^{\infty} dx n(x) = \frac{2}{\pi}\sqrt{\frac{2m^*}{\hbar^2}} \sum_{\ell,E_\ell \le E_F} \sqrt{E_F - E_\ell}, \tag{2.22}$$

where η is the linear density of electrons along the y-direction. Eq. (2.22) can be used to determine the Fermi energy E_F once η is known. Note that, because the Coulomb-confined quantum wire is overall charge neutral,

$$\eta = w\sigma. \tag{2.23}$$

Therefore η is determined if w and σ are given.

2.3 Programming

For a single Coulomb-confined quantum wire, there are three independent model parameters: the area donor density σ, the width of the donor ribbon w, and the separation d between the donor ribbon and the electron plane. These three model parameters are the inputs for the program. The two constant parameters involved are the dielectric constant ε and

the effective mass of electron m^*. In our calculations, they are chosen to be $\varepsilon = 12.5$ and $m^* = 0.067\ m_e$, which correspond to the values for a GaAs-$Al_xGa_{1-x}As$ quantum wire.

Our numerical calculations are performed using the self-consistent technique. This technique can be described by the following calculation steps.

1. Choose an initial trial function for the electron density $n(x)$. For example, we can use the donor density $n_d(x)$ as a trial function for $n(x)$.

2. Calculate the Coulomb energy $V_c(x)$ from Eq. (2.16) using the trial function for $n(x)$.

3. Calculate the exchange energy $\epsilon_x(n(x))$ from Eq. (2.11) and the correlation energy $\epsilon_c(n(x))$ from Eq. (2.12) using the trial function for $n(x)$.

4. Substitute the calculated $V_c(x)$, $\epsilon_x(n(x))$, and $\epsilon_c(n(x))$ into Eq. (2.8). Obtain the effective potential energy $V_{eff}(x)$.

5. Solve the Schrödinger Eq. (2.17) using the calculated $V_{eff}(x)$. Obtain the transverse energy levels E_ℓ and wavefunctions Φ_ℓ.

6. Obtain the Fermi energy E_F from Eq. (2.22) using the calculated transverse energy levels E_ℓ.

7. Calculate the electron density $n(x)$ from Eq. (2.21) using the calculated Fermi energy E_F, transverse energy levels E_ℓ, and wavefunctions Φ_ℓ.

8. Determine the degree of consistency between the trial and calculated electron densities $n(x)$. If a sufficient agreement has been achieved, terminate the calculation and output results. Otherwise, choose another trial function for $n(x)$ and go back to step 2.

There are many criteria for determining the degree of consistency in step 8. The crucial point is, if a sufficient agreement is achieved, the "new" calculated $n(x)$ in step 7 should be sufficiently close to the "old" $n(x)$ that was used in steps 2 and 3. That is, the solution is *self-consistent.* In our calculations, we use the following criterion

$$\int_{-\infty}^{\infty} dx \frac{|n(x)[\text{new}] - n(x)[\text{old}]|}{n(x)[\text{old}]} < \delta, \tag{2.24}$$

where δ is the accuracy required for a calculation. If Eq. (2.24) is satisfied, then the calculation is completed. In our calculations, δ is chosen to be 0.01 or less.

Note that in the last step of the above calculation cycle, it is usually not a good idea to use the "new" calculated $n(x)$ in step 7 as the trial function $n(x)$ for the *next* iteration of the calculation. Using directly the "new" calculated $n(x)$ can result in strong "oscillations", which keep the calculation from approaching to the self-consistent solution. A better way to choose a "next" trial function is to combine the "new" calculated $n(x)$ in step 7 and the "old" $n(x)$ that was used in steps 2 and 3, that is,

$$n(x)[\text{next}] = (1 - r) \times n(x)[\text{old}] + r \times n(x)[\text{new}], \tag{2.25}$$

where $0 < r < 1$. Using a small r can avoid oscillations in the iteration procedure efficiently.

In programming, we have used several numerical techniques to improve the calculation performance.

- In this calculation project, a major task is to solve the Schrödinger Eq. (2.17), which is a quadratic differential equation. For this purpose, we implement the NAG Subroutine D02FEF, which provides solutions for such a differential equation with both its eigen values and eigen functions. Based on many numerical tests, we found that the most efficient way to implement the Subroutine D02FEF is to use the zero-value boundary conditions, i.e., the eigen functions are zero at the boundaries of x. However, in order to use the zero-value boundary condition without introducing significant errors, we need to solve the equation in a sufficiently large calculation range $[-X, X]$ for x. (We are only interested in the bound states whose wavefunctions are exponentially small for large $|x|$.) However, when X is too large, the solutions given by the Subroutine D02FEF are not reliable. We found that the optimized calculation range is $X \sim 5w$, which ensures both reliable solutions of the differential equation and a sufficient accuracy.

- The second consideration concerns eliminating metastable states. For this purpose, we use from time to time a large r in Eq. (2.25) deliberately to "kick" the iterations out of the metastable state if it occurs. We also use different initial trial functions for $n(x)$ for the same *calculation point* (i.e., a set of given model parameters) and verify if the final solutions are the same. Once we have obtained such a reliable solution for a particular calculation point, which must be the self-consistent solution, we use this solution as the initial trial function for the next calculation point whose model parameters change only slightly. In this way, we can make sure that all of the solutions are not associated with metastable states.

- Finally, to save calculation time, we have used an algorithm that automatically adjusts the point density of the arrays used. In other words, the spatial density of the points used in the calculations is determined according to the rate of variation of the relevant function in that local region. The more rapidly the relevant function changes, the more points are taken in that region. This algorithm significantly decreases the execution time of many calculation tasks, such as the calculation of Eq. (2.16) for the Coulomb energy. (Note that the integration function in Eq. (2.16) has a singularity.)

The calculation program was coded in FORTRAN 77. For a single Coulomb-confined quantum wire, each calculation point takes about 30 minutes to finish (assuming that the program runs with one processor on a Silicon Graphics computer at Simon Fraser University). For two parallel quantum wires, the calculation time is increased several times because of the subtle effect of charge balance between the two quantum wires.

Chapter 3

Single Coulomb-Confined Quantum Wires

This chapter presents the calculated ground-state electronic structure of *single* Coulomb-confined quantum wires. In the first section, we study the many-body effects in the Coulomb-confined quantum wires by comparing the electronic structures calculated using the density functional theory and in the Hartree approximation. In the second section, we give a qualitative discussion of the bound states in the Coulomb-confined quantum wires, and of the implications of the nature of the bound states for the calculated results. The third section focuses on the dependence of the electronic structure of the Coulomb-confined quantum wires on the model parameters. Most of the results presented in this chapter have been published in Ref. [31].

3.1 Many-Body Effects

3.1.1 Density Functional Calculations

Fig. 3.1 shows typical results of calculations for a single Coulomb-confined quantum wire using the density functional theory. The model parameters used for this calculation are: $w = 200$ nm, $d = 20$ nm, and $\eta = 2 \times 10^5$ cm^{-1}. Fig. 3.1(a) shows the lateral profiles of the effective potential energy $V_{\rm eff}(x)$, Coulomb energy $V_{\rm c}(x)$, and $\mu_{\rm x}(x)$ and $\mu_{\rm c}(x)$, which are the contributions of the exchange energy and correlation energy to $V_{\rm eff}(x)$ (see Eqs. (2.8), (2.9) and (2.10)), respectively. The Fermi energy is $E_{\rm F} = -0.96$ meV, and the three lowest

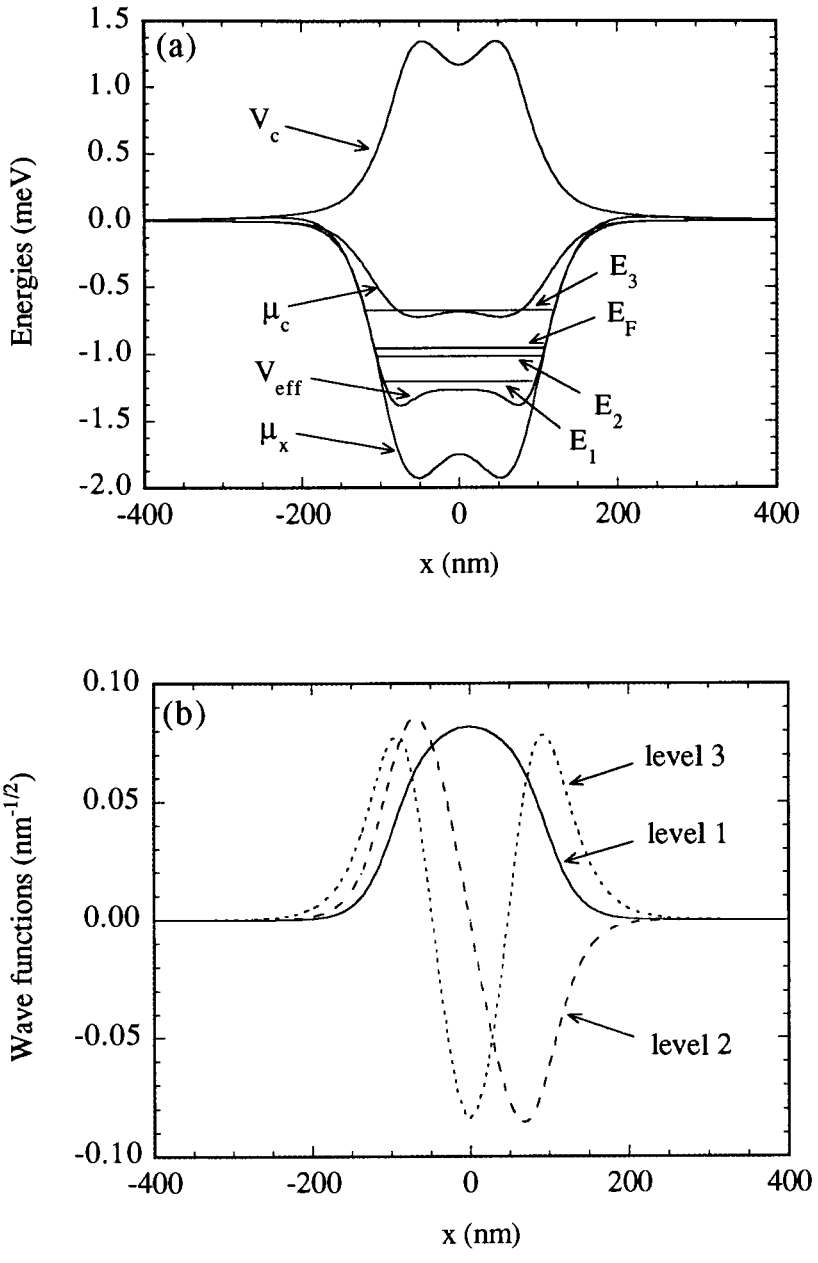

Figure 3.1: Typical calculated results for a single Coulomb-confined quantum wire using the density functional theory. The model parameters are: w = 200 nm, d = 20 nm, and $\eta = 2 \times 10^5$ cm^{-1}. (a) The curves are the effective potential energy $V_{\rm eff}(x)$, the Coulomb energy $V_{\rm c}(x)$, and the contributions of the exchange and correlation energies $\mu_{\rm x}(x)$ and $\mu_{\rm c}(x)$, respectively. The Fermi energy $E_{\rm F}$ and the three lowest transverse levels are also shown. (b) The density functional wavefunctions of the three lowest transverse levels.

transverse energy levels are $E_1 = -1.22$ meV, $E_2 = -1.02$ meV and $E_3 = -0.65$ meV. The density functional wavefunctions of the three lowest transverse energy levels are shown in Fig. 3.1(b).

As shown in Fig. 3.1(a), the Fermi energy is located between the second and the third transverse energy levels. This means that only the two lowest transverse levels (also called subbands) are populated by electrons. Fig. 3.1(b) shows that the density functional wavefunctions of the three lowest transverse energy levels are clearly confined to the immediate vicinity of the donor ribbon, i.e., $-w/2 \leq x \leq w/2$. Therefore all of the populated states are strongly bound.

It is interesting to note that the Coulomb energy $V_c(x)$ in this density functional calculation is positive everywhere, while the exchange and correlation energies are negative and large. The exchange and correlation energies are so strong that in fact they provide the potential well that confines electrons laterally. Because of this strong attraction due to the exchange and correlation effects, electrons are bound so tightly to the central region of the potential well that the Coulomb energy $V_c(x)$, which includes both electron-donor and electron-electron Coulomb interactions (see Eqs. (2.15) and (2.16)), is overall positive. The lateral confinement of electrons is thus provided by the exchange and correlation energies. This result shows that the exchange and correlation effects are very important in the Coulomb-confined quantum wire.

3.1.2 Hartree Calculations

Fig. 3.2 shows typical results of the calculation in the Hartree approximation for the same model parameters as are used in Fig. 3.1. Fig. 3.2(a) shows the lateral profile of the Coulomb energy $V_c(x)$, the Fermi energy $E_F = 0.135$ meV, and the three lowest transverse energy levels $E_1 = -0.086$ meV, $E_2 = 0.077$ meV, and $E_3 = 0.133$ meV. The Hartree wavefunctions for the three lowest transverse energy levels are shown in Fig. 3.2(b). In this calculation the electrons were taken to be confined to the range $|x| \leq 1000$ nm by choosing zero boundary conditions on the wavefunctions at $x = \pm X = \pm 1000$ nm.

As we can see, the electronic structure calculated in the Hartree approximation is entirely different from the one calculated using the density functional theory. The potential well and the transverse energy levels from the Hartree calculation are very shallow compared to those from the density functional calculation. The Hartree wavefunctions of levels 2 and 3, which are populated, extend significantly beyond the region of the potential well $-w/2 \leq x \leq w/2$,

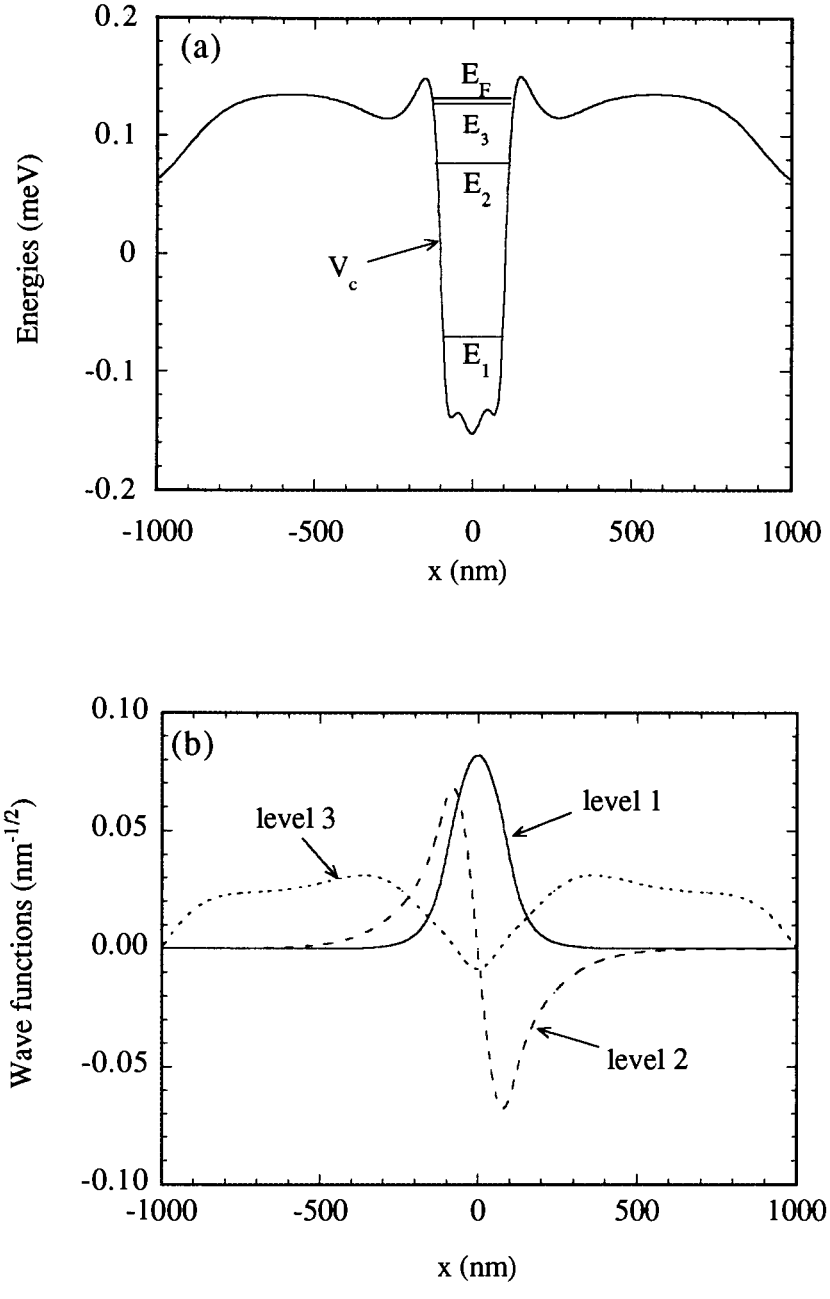

Figure 3.2: Typical results calculated in the Hartree approximation. The model parameters are: $w = 200$ nm, $d = 20$ nm, and $\eta = 2 \times 10^5$ cm^{-1}. (a) The profile of the Coulomb energy $V_c(x)$, the Fermi energy E_F, and the three lowest transverse energy levels. Note that the slight asymmetry of $V_c(x)$ near $x = 0$ is due to the limited numerical accuracy. (b) The Hartree wavefunctions of the three lowest transverse energy levels.

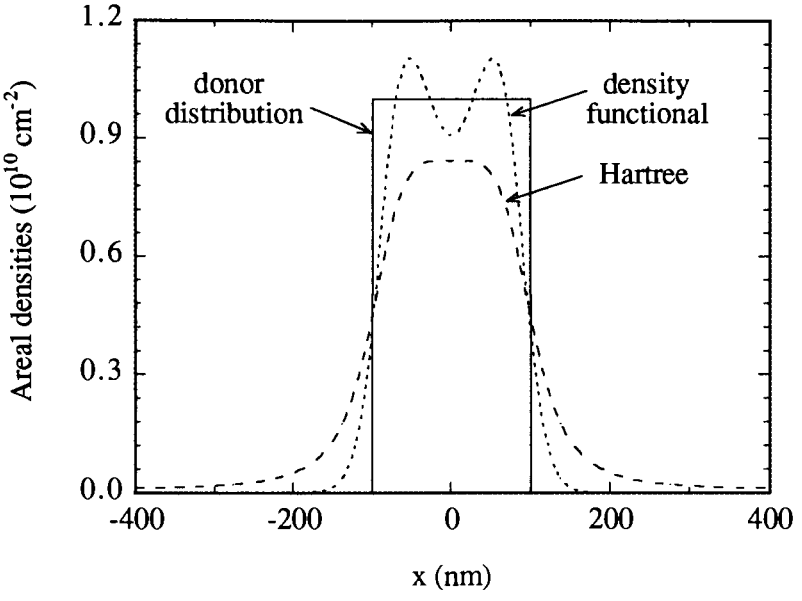

Figure 3.3: The area densities of electrons from the density functional and Hartree calculations with comparison to the fixed area density of donors.

which means that these two populated levels are not strongly bound. Such states will be referred to as "weakly bound states". These remarkable differences between the calculated electronic structures are because the strong exchange and correlation effects are not taken into account in the Hartree approximation. This is why the Hartree potential well is very shallow and its confinement of the electrons is very weak.

The difference between the density functional calculation and the Hartree calculation are also reflected in the calculated lateral distributions of electrons. Fig. 3.3 displays the lateral distributions of electrons corresponding to the density functional and Hartree calculations, and compares them with the fixed area density of donors. This figure indeed shows that a considerable number of electrons spread beyond the region of the potential well in the Hartree calculation, while the electrons are very tightly confined to the central regions for the density functional calculation.

Based on the above comparison, we conclude that the exchange and correlation effects are very important for the Coulomb-confined quantum wire. The many-body effects must be included in the calculations, and the Hartree approximation is not adequate for this case. Our numerical results for the Coulomb-confined quantum wire provide new evidence that many-body effects tend to be stronger in low-dimensional systems, as was proposed in

previous theoretical studies [132].

3.2 Bound States

Let us now turn our attention temporarily to discussing an important issue that is associated with the nature of the bound states, because this helps one understand the implications of our numerical results.

Since we choose the zero of the potential energy at $x = \pm\infty$, a bound transverse level must have a negative energy eigen value. This fact raises the question: do the positive energies of levels 2 and 3 in Fig. 3.2(a) mean that *unbound* levels are populated by electrons in the Hartree approximation?

Before answering this question, one should note that the above numerical calculations are done in a *finite* range of x, i.e., $-X \leq x \leq X$, and using zero-value boundary conditions on the transverse wavefunctions at $x = \pm X$. Hence the numerical results correspond rigorously to the Coulomb-confined quantum wire suggested in Fig. 2.1 only when $X \to \infty$. But *when* $X \to \infty$, *all populated levels must be bound, even in the Hartree approximation.* This statement can be proved by contradiction:

> Suppose that some populated levels were not bound for $X \to \infty$. Then a finite amount of charge per unit length of the wire would be completely removed from the wire and go away to infinity. Then there would be a net positive charge (say Δq) per unit length of the system consisting of the donor ribbon and electrons that are bound to it. Then the total electrostatic potential would contain a term that is proportional to $\Delta q \ln|x|$ when $|x|$ approaches infinity. Therefore if there were populated unbound levels, then the quantum wire would be contained in a potential well with very soft but infinitely high walls. But such a infinitely high potential well has NO unbound levels at all. So we have a contradiction and the initial assumption that there are unbound populated levels is not correct. Therefore, all populated levels must be bound.

Based on this argument, the Hartree numerical results that levels 2 and 3 have positive energy eigenvalues means that, in the Hartree approximation, these levels are *weakly bound states* and their positive energies must be caused by the finiteness of X and the zero-value boundary conditions.

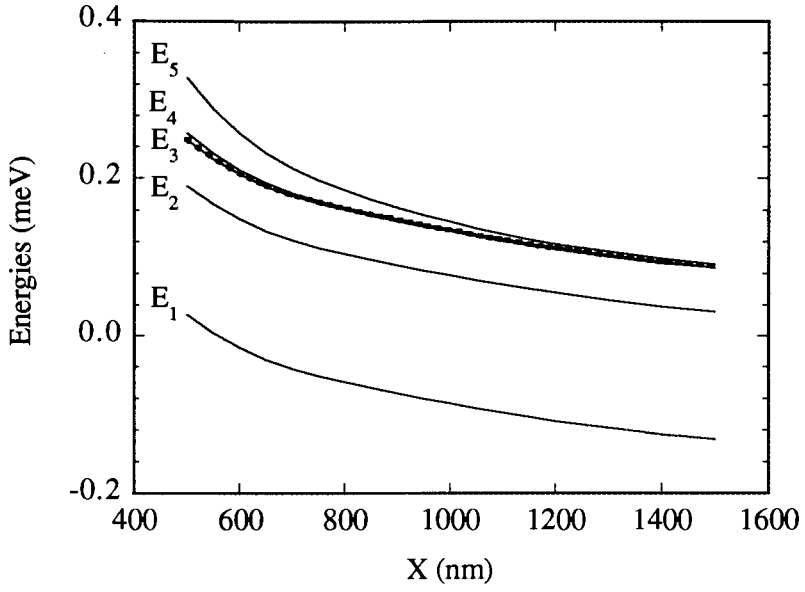

Figure 3.4: The five lowest transverse levels (solid lines) and the Fermi energy (dotted line) from the Hartree calculations using different X. The model parameters used are: $w = 200$ nm, $d = 20$ nm, and $\eta = 2 \times 10^5$ cm^{-1}.

To investigate the effect of the finiteness of the range of the calculations, we repeated the Hartree calculations using the same model parameters but with different values of X. The results are shown in Fig. 3.4. When X is increased, the Fermi energy and all of the transverse energy levels decrease monotonically albeit quite slowly. The dependence of energies on X shows again that levels 2 and 3 are only weakly bound. Because the wavefunction of such a weakly bound level has a considerable amplitude well outside of the region $[-w/2, w/2]$ of the potential well, using a finite calculation range and the zero-value boundary conditions has a significant effect on the wavefunction of this level, and thus on the calculated energy. When X is increased, electrons are allowed to distribute within a larger range and thus the repulsion between the electrons is reduced. Hence the electrostatic energy (as well as the kinetic energy) becomes lower and the potential well becomes deeper and all energy levels become lower. The very slow decrease of the energy levels with increasing X when X is large ($X > 1000$ nm) implies that levels 2 and 3 are extremely *weakly bound* and their wavefunctions spread over a range much larger than $[-w/2, w/2]$. This analysis tells us that *if some weakly bound states are populated, the calculation results are not reliable* because they depend on the value of X.

When using the same model parameters as used in Fig. 3.4 to do the same calculations in the density functional theory, we found that the calculated Fermi energy and energy levels are quite stable relative to different values of X. This is because, in the density functional calculations, the exchange and correlation energies are included and, as a result, the populated energy levels are strongly bound for the model parameters used. However, it should be pointed out that, even in the density-functional calculations, weakly bound states can be populated when the spatial distance between the electron plane and the donor ribbon is large enough, or the linear electron density of the quantum wire is very high. Such effects will be seen in the calculations presented in the next section.

3.3 Effects of the Model Parameters

3.3.1 Linear Density of Electrons

The dependence of the calculated[1] electronic structure of the Coulomb-confined quantum wires on the linear density of electrons is shown in Fig. 3.5. Fig. 3.5(a) shows the Fermi energy and the five lowest transverse levels against the linear electron density η ranging from 0.5×10^5 cm^{-1} to 8×10^5 cm^{-1}. Fig. 3.5(b) shows the values at $x = 0$ of the effective potential energy $V_{\rm eff}$, Coulomb energy $V_{\rm c}$, and the contributions of the exchange and correlation energies $\mu_{\rm x}$ and $\mu_{\rm c}$. The width of the donor ribbon is $w = 200$ nm and the separation between the electron plane and the donor ribbon is $d = 20$ nm.

In Fig. 3.5(a), all of the populated levels are well below zero. This means that the populated levels are tightly bound[2] and thus *the numerical results are reliable.* Note that, however, when the linear density of electrons is increased further beyond 8×10^5 cm^{-1}, the 5th transverse level will become populated. According to Fig. 3.5(a), this level has a positive energy and therefore must be weakly bound. This shows that weakly bound states can be populated when the linear density of electrons is sufficiently high, even in the density functional theory.

An interesting feature shown in Fig. 3.5(a) is that whenever the Fermi energy crosses a transverse level, the curve of the Fermi energy tends to follow the curve of the level that has just been crossed by $E_{\rm F}$. This happens when the linear density is equal to 1.3×10^5 cm^{-1},

[1] From now on, all numerical results are from density functional calculations.

[2] Because this is a Coulomb system and the potential energy is chosen to be zero at infinity, bound states have negative eigenenergies. Note, however, that some very weakly bound states (discussed below) have positive energies in the present calculations because the calculations were performed in a finite range of x.

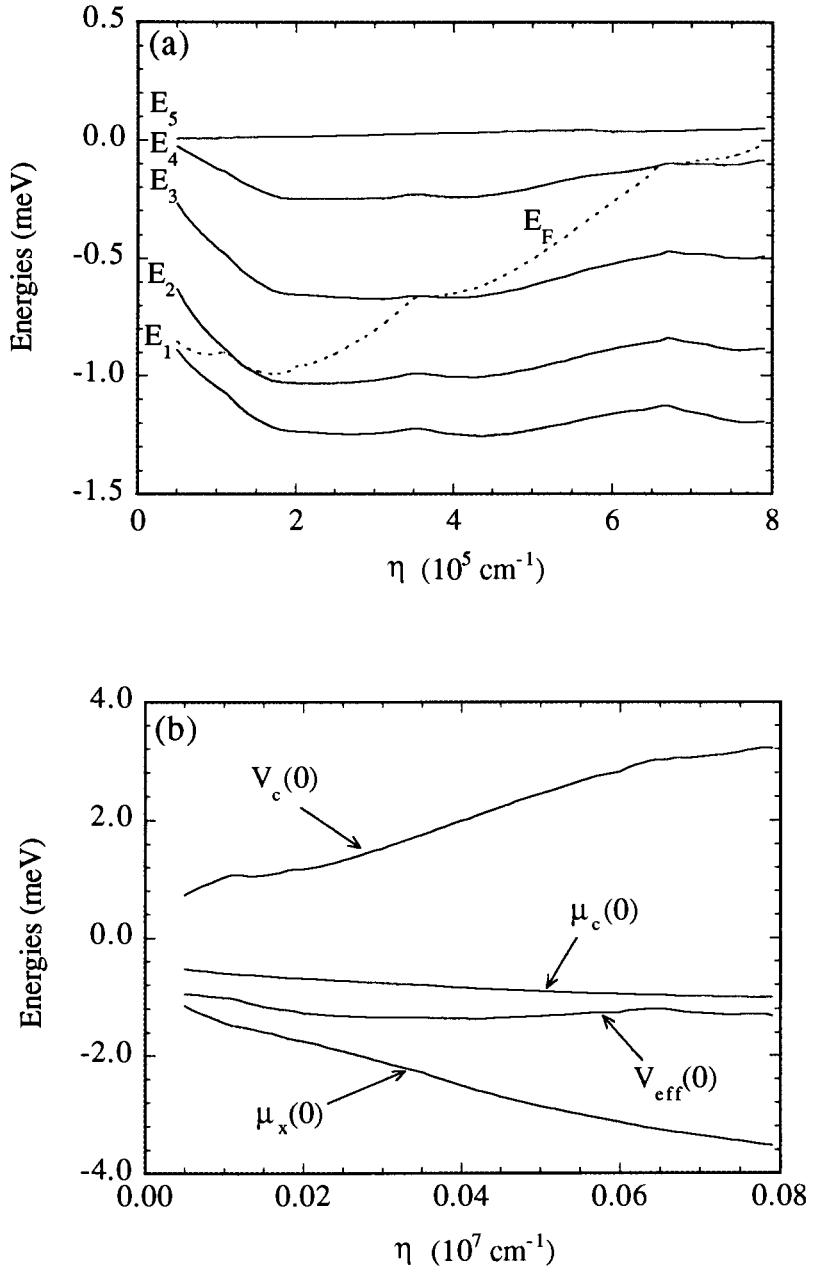

Figure 3.5: The dependence of the electronic structure on the linear density of electrons. For this calculation $w = 200$ nm, $d = 20$ nm and $X = 1000$ nm. (a) Fermi energy and the five lowest transverse levels. (b) The energy values at $x = 0$ for V_{eff}, V_{c}, μ_{x} and μ_{c}.

3.6×10^5 cm^{-1}, and 6.6×10^5 cm^{-1}. This effect reflects the singularities of the density of states at the Fermi energy when E_F coincides with an energy level. Because the quantum wire is a quasi-one-dimensional system, the density of states is generally described by

$$D(E) = \frac{1}{\pi}\sqrt{\frac{2m^*}{\hbar^2}} \sum_{\ell, E_\ell \le E} \frac{1}{\sqrt{E - E_\ell}}, \tag{3.1}$$

and at the Fermi energy

$$D(E_F) = \frac{1}{\pi}\sqrt{\frac{2m^*}{\hbar^2}} \sum_{E_\ell \le E_F} \frac{1}{\sqrt{E_F - E_\ell}}. \tag{3.2}$$

(Note that Eq. (3.2) can be obtained directly from taking a derivative with respect to E_F of Eq. (2.22).) Therefore, when E_F is just above the bottom of a subband, the density of states $D(E_F)$ is very large so that increasing the number of electrons can only raise the Fermi level slightly. Also because of these singularities, the curves of the transverse energy levels change their slopes when the Fermi level crosses a transverse level.

Another interesting feature is that, all transverse energy levels first decrease and then increase in energy while η increases. This behavior results from the competition between the Coulomb energy and the exchange-correlation energy. According to Eq. (2.11), $\epsilon_x \propto -n^{1/2}$. The correlation energy ϵ_c also increases negatively with n, but slower than ϵ_x. (See Eq. (2.12).) The Coulomb energy has no strict power-law dependence on the electron density, because the electron density appears in the integral in Eqs. (2.15) and (2.16). However, when all populated transverse levels are tightly bound, electrons distribute mainly within the potential well and thus approximately $V_c \propto n$. At low electron densities, the exchange-correlation energy dominates the Coulomb energy. As we have seen, the exchange-correlation energy confines electrons so tightly that the Coulomb energy is overall positive. Because the exchange-correlation energy dominates the Coulomb energy at low densities, increasing η results in further lowering of all transverse levels. However, when the electron density is increased sufficiently, the Coulomb energy becomes more important, thus causing the energy curves to become flat and then to rise gradually. The curves in Fig. 3.5(b) reflect the general trends of the changes in the different energies with η. Note that the curves in Fig. 3.5(b) can only reflect the energy changes roughly, because they are the values at $x = 0$ and the energies always oscillate near $x = 0$ (see Fig. 3.1). Finally, it should be mentioned that the kinetic energy always increases with η.

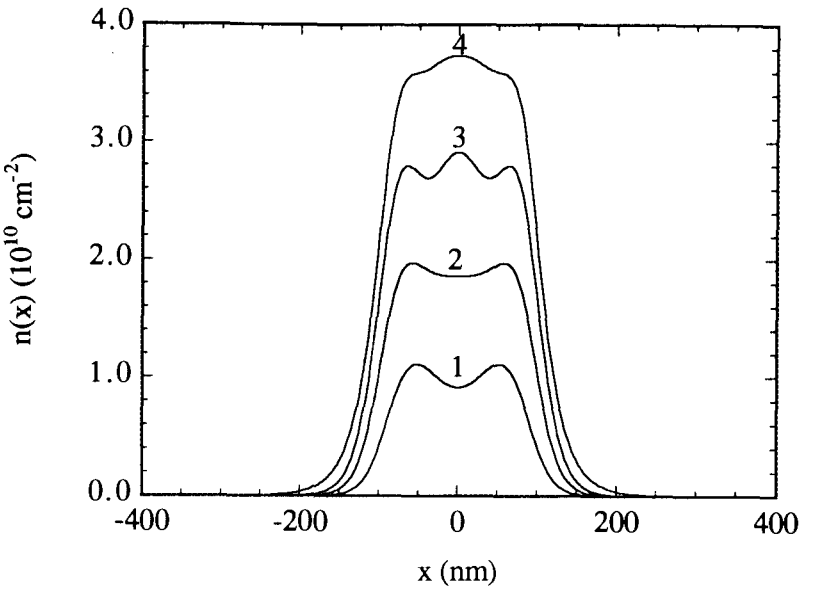

Figure 3.6: The lateral distributions of electrons for different values of η when $w = 200$ nm, $d = 20$ nm, and $X = 1000$ nm. Curves 1, 2, 3, and 4 correspond to η being 2×10^5 cm^{-1}, 4×10^5 cm^{-1}, 6×10^5 cm^{-1}, and 8×10^5 cm^{-1}, respectively.

Fig. 3.6 shows the lateral distributions of electrons for η equal to 2×10^5 cm^{-1}, 4×10^5 cm^{-1}, 6×10^5 cm^{-1}, and 8×10^5 cm^{-1}, which correspond to the curves numbered with 1, 2, 3, and 4, respectively. (Note that the electron densities n are typically on the 10^{10} cm^{-2} scale.) The small oscillatory structures near $x = 0$ are associated with the numbers of subbands populated by electrons. Referring to Fig. 3.5(a), for curves 1, 3, and 4, the number of populated transverse levels are 2, 3, and 4, respectively. For curve 2, with $\eta = 6 \times 10^5$ cm^{-1}, the third level is populated but is close to the Fermi energy, and therefore this curve still shows a two-peak but flattened structure.

3.3.2 Effects of Distance

The typical behavior of the various energies against the distance d between the donor ribbon and the electron plane is shown in Fig. 3.7. For this calculation, the width of donor ribbon is $w = 200$ nm and the linear electron density is 2×10^5 cm^{-1}. Fig. 3.7(a) shows the variations of the Fermi energy and of the five lowest levels for d from zero to 60 nm. In this figure, we observe how the strongly bound levels 4 and 5 become weakly bound when d becomes large enough. For these model parameters, the Fermi energy increases with d at

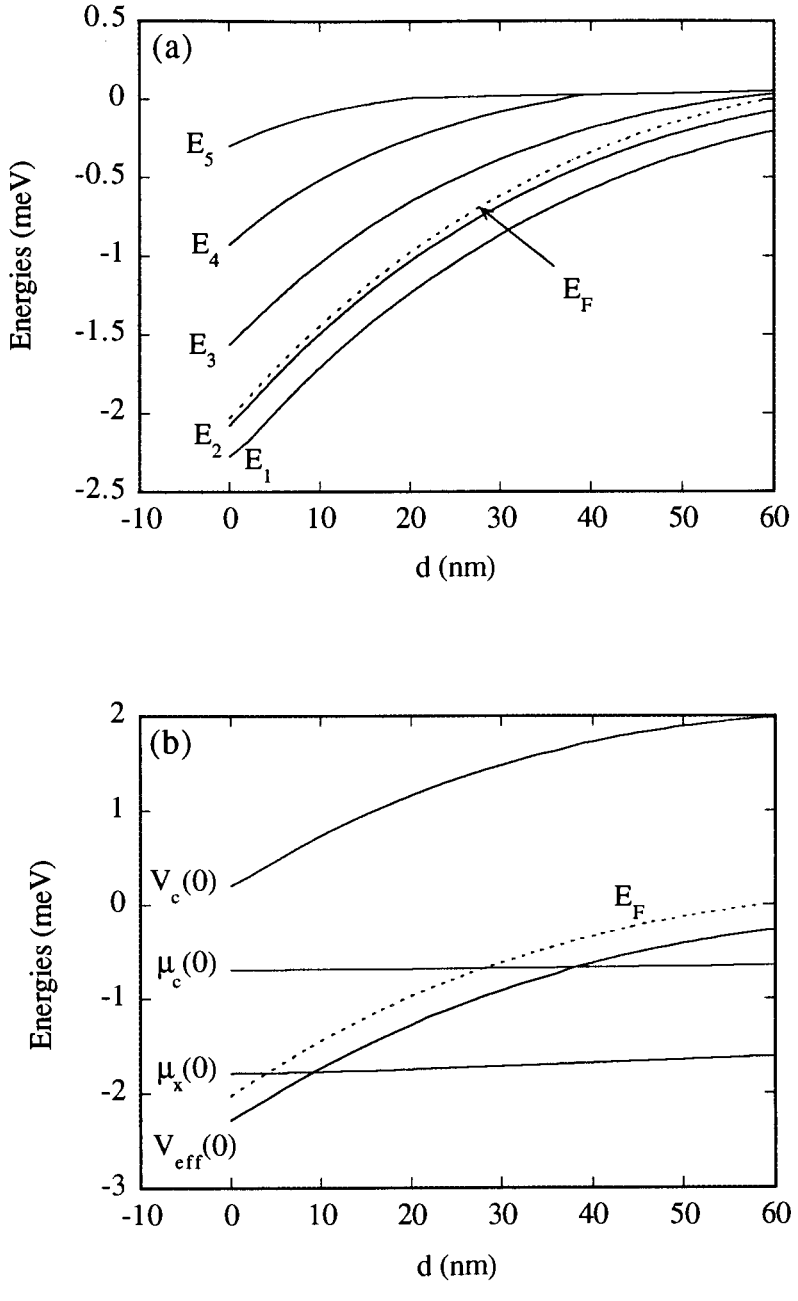

Figure 3.7: The energy behavior against d. The model parameters are $w = 200$ nm, $\eta = 2 \times 10^5$ cm^{-1}, and $X = 1000$ nm. (a) Fermi energy and the five lowest transverse levels. (b) The values at $x = 0$ of V_{eff}, V_{c}, μ_{x} and μ_{c}, as well as the Fermi energy.

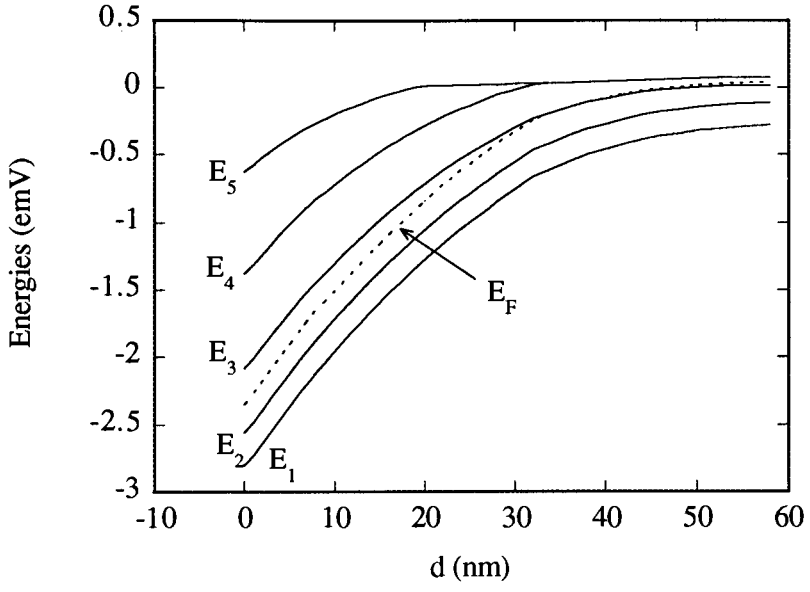

Figure 3.8: The dependence of the transverse energy levels and Fermi level on the distance d for $w = 200$ nm, $\eta = 3 \times 10^5$ cm^{-1}, and $X = 1000$ nm.

almost the same pace as the occupied levels and therefore the Fermi energy does not cross any level in the regime in which only strongly bound levels are occupied. In Fig. 3.7(b), we plot the $x = 0$ values of the Coulomb energy, exchange energy, correlation energy, and total effective potential energy, and the Fermi energy against d. While the exchange and correlation energy values are very insensitive to the variation of d, the Coulomb energy value changes significantly. The Fermi energy tracks the effective potential energy V_{eff} quite closely, which indicates that the kinetic energy is not sensitive to the value of d.

For a comparison, we display in Fig. 3.8 the energy dependence on d with $w = 200$ nm but a higher linear density $\eta = 3 \times 10^5$ cm^{-1}. Notice that the Fermi energy crosses the third level when $d = 36$ nm. As the separation increases further, the third level becomes weakly bound because its energy is above zero. Its wavefunction extends well beyond the region of the positive ribbon and is similar to that of level 3 in Fig. 3.2b. (See footnote 2 on page 46.)

3.4 Summary

The main results obtained in this chapter can be summarized as follows:

1. The exchange and correlation effects are very important in the Coulomb-confined quantum wires. The Hartree approximation is not adequate for such systems and numerical calculations should be done using the density functional theory.

2. The numerical results are reliable if all populated transverse energy levels are tightly bound states.

3. All of the electrons are tightly bound within the effective potential well at low linear electron densities and small separations between the donor ribbon and the electron plane. However, some weakly bound transverse levels can be populated by electrons at high densities and/or large separations.

These conclusions are useful for our further numerical studies of the electronic structure of two parallel quantum wires to be presented in the next chapter.

Before finishing this chapter, it is necessary to make a few remarks. First, the numerical results presented in this chapter are based on the exchange-correlation energy calculated by Tanatar and Ceperly [156]. We have also used the exchange-correlation energy of Jonson [155], and the results agree very well with those using the Tanatar and Ceperly's values. Second, the Hartree calculations have been successful in previous numerical studies of gated quantum wires [130, 131]. The reason is that the electron density in the gated quantum wires (typically $n \sim 10^{11}$ cm^{-2}) is much higher than the electron density in the Coulomb-confined quantum wires (typically $n \sim 10^{10}$ cm^{-2}). Our calculations have shown that the Coulomb energy tends to be more important at high electron densities. The comparison between the exchange and correlation effects and the Coulomb energy for high electron densities deserves further studies. Finally, the present numerical method is applicable only to the situations in which all populated levels are tightly bound states. To study situations when weakly bound states are populated, i.e., when the electron density or the separation between the electron plane and the donor ribbon is sufficiently large, a new numerical approach should be developed. The latter project is interesting because it describes the transition regime from quasi-one-dimensional to quasi-two-dimensional systems.

Chapter 4

Two Parallel Quantum Wires

In studying quantum mechanical systems it is often illuminating to view them as composed of subsystems, weakly or strongly coupled together. When a pair of energy levels belonging to two such subsystems approach each other, an *energy level crossing* or *anti-crossing* occurs, as illustrated in Fig. 4.1(a) and Fig. 4.1(b), respectively. Simple level crossings happen when the matrix elements of the Hamiltonian that are responsible for the hybridization between the states of the subsystems vanish, often for reasons of symmetry. On the other hand, anti-crossings occur because quantum hybridization between the subsystems becomes important in near-degenerate situations. The hybridization opens an energy gap, lifting the incipient level degeneracy. For example, the band gaps that control the electronic properties of crystalline solids can be viewed as manifestations of energy level anti-crossings.

However, energy level crossings and anti-crossings are not the only possibilities in near-degenerate situations. As will be demonstrated in detail below, a third type of behavior is also possible, namely, *energy level locking*. This new phenomenon is illustrated in Fig. 4.1(c). Energy level locking may be thought of as the opposite of anti-crossing. That is, instead of nearly degenerate energy levels "repelling" each other, they lock together. In this chapter, we will show that the energy level locking can occur in two parallel Coulomb-interacting quantum wires, and that this new phenomenon is a characteristic of Coulomb-coupled quasi-one-dimensional fermionic systems.

The calculations of this chapter are based on the density functional theory and the self-consistent calculation technique described in Chapter 2. In the first part of this chapter, we first present the results of calculations for two *similar* parallel quantum wires which display the energy level locking, and then investigate the reason for this novel effect. In the second

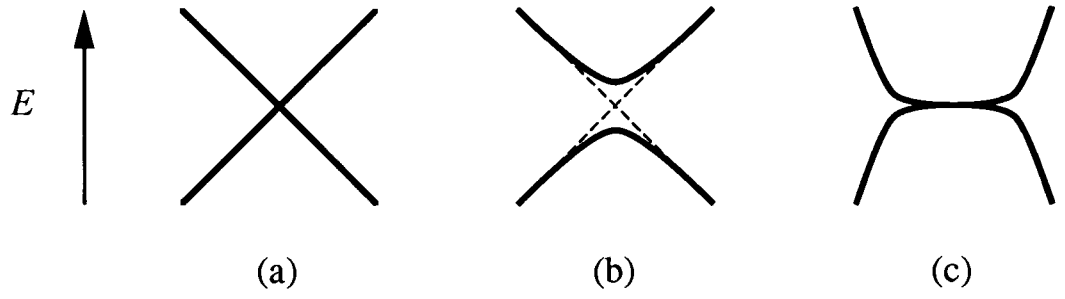

Figure 4.1: The behavior of energy levels in near-degenerate situations. (a) Crossing. (b) Anti-crossing. (c) Locking.

part, we present results of calculations for two *dissimilar* parallel quantum wires. Finally, we summarize the numerical results and discuss their experimental implications. The results presented in this chapter have been published in references [32, 33, 34].

The structure of two parallel Coulomb-confined quantum wires is shown in Fig. 4.2. This structure is similar to that of the single quantum wire shown in Fig. 2.1, but now the system has two parallel donor ribbons A and B. These ribbons donate electrons to the electron plane and thus themselves become two strips of positive charge. For the two parallel quantum wires, there are six model parameters: the width $w_{\rm a}$ and area donor density $\sigma_{\rm a}$ for donor ribbon A, the width $w_{\rm b}$ and area donor density $\sigma_{\rm b}$ for donor ribbon B, the separation s between the two ribbons, and the distance d between the donor ribbons and the electron plane. (Note that the two donor ribbons are in the same plane.) These six parameters are the inputs of the calculations. The formalism and the procedure used in the calculations are the same as described in Chapter 2, except that Eq. (2.14) should be replaced by

$$n_{\rm d}(x) = \begin{cases} \sigma_{\rm a}, & \text{if } -s/2 - w_{\rm a} \le x \le -s/2 \\ \sigma_{\rm b}, & \text{if } s/2 \le x \le s/2 + w_{\rm b} \\ 0, & \text{otherwise} \end{cases} \tag{4.1}$$

where $\sigma_{\rm a}$ and $\sigma_{\rm b}$ are the area donor densities for ribbons A and B, respectively.

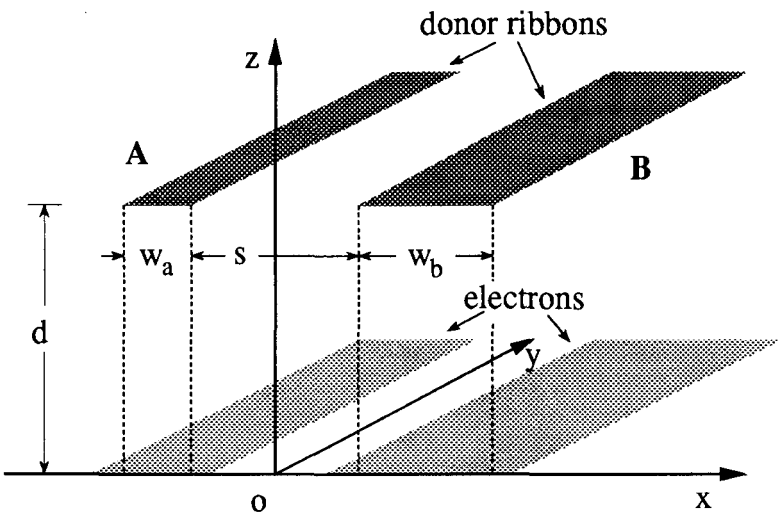

Figure 4.2: Schematic drawing of two parallel Coulomb-confined quantum wires. Electrons are confined to the xy-plane. The donor ribbon A has a width w_a and area donor density σ_a, and the donor ribbon B has a width w_b and area donor density σ_b. The two ribbons have a separation s and an offset distance d from the electron plane. The whole system is embedded in a uniform dielectric and is charge-neutral.

4.1 Similar Quantum Wires: Energy Level Locking

The calculated electronic structure of two similar parallel quantum wires is shown in Fig. 4.3. The model parameters used are $w_a = 190$ nm, $w_b = 200$ nm, $s = 200$ nm, and $d = 20$ nm. The donor densities in the two ribbons are kept the same $\sigma_a = \sigma_b = \sigma$, which is the abscissa of this calculation. (Since the system is charge-neutral overall, σ can also be regarded as an electron filling parameter.) The solid lines are the six lowest transverse energy levels, and the dashed line is the Fermi energy. The energy levels are labeled A or B, according to whether they belong primarily to wire A or B, respectively, as determined by inspection of the calculated wavefunctions.

In Fig. 4.3, when the Fermi energy rises up through the lower of a pair of adjacent energy levels with increasing σ, the (algebraic) slope of the lower energy curve of the pair increases while that of the upper curve decreases. Thus the two corresponding energy levels are brought closer together. Levels 3 and 4 lock together at the Fermi energy, while the gap between levels 5 and 6 narrows by a factor of about 5. These are clearly effects of *energy level locking*. The energy level locking is associated with the Fermi energy crossing

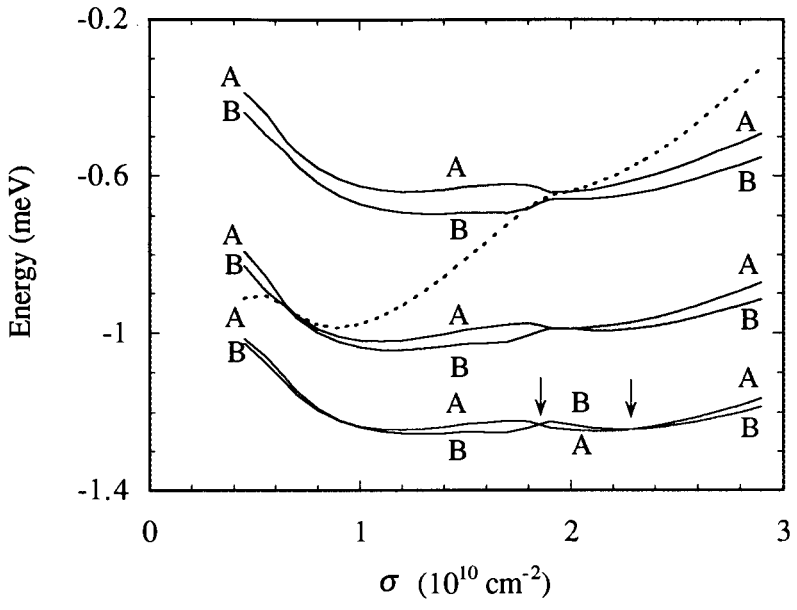

Figure 4.3: The calculated results of two similar parallel quantum wires. The used model parameters are w_a = 190 nm, w_b = 200 nm, s = 200 nm, and d = 20 nm. The six lowest transverse levels (solid lines) and Fermi energy (dotted line) against the uniform donor density σ. Energy levels are labeled A and B according to which wire they belong principally to. Arrows indicate anti-crossings.

the corresponding levels. Note that the locked levels tend to remain together and that the sequence of the locked levels remains unchanged throughout. As we can see in Fig. 4.3, the locked level belonging to wire B is always lower than the locked level belonging to wire A.

The energy level locking is caused by a charge imbalance that occurs between the two quantum wires when a transverse level begins to fill. The origin of the charge imbalance is the $E^{-1/2}$ density of states singularity at the bottom of a subband (see Eq. (3.1)), which is a characteristic of quasi-one-dimensional systems. When the Fermi energy rises up through a transverse level E_ℓ, because of the density of states singularity, most of the added electrons go into subband ℓ. Thus the wire to which E_ℓ mainly belongs acquires an excess of electrons, and a charge imbalance occurs. Such a charge imbalance, through the Coulomb interaction, shifts the self-consistent electrostatic potential and thus the transverse energy levels of the wire with the excess (deficiency) of electrons upwards (downwards) significantly, favoring energy level locking. Energy levels that lock together do not separate immediately when the Fermi energy rises above them, because their density of states singularities almost coincide,

which inhibits further changes of the charge differential.

Some features of the electronic structure shown in Fig. 4.3 can be understood qualitatively as a competition between a charge imbalance and inter-wire quantum hybridization. The inter-wire quantum hybridization acts to separate the adjacent levels, and thus opposes energy level locking. In Fig. 4.3, the separation between levels 3 and 4 and the separation between levels 5 and 6 narrow markedly when the Fermi energy crosses them. This implies that the charge imbalances are the dominant factor. However, the energy gap between levels 5 and 6 remains fairly large. This is because inter-wire quantum tunneling and therefore hybridization is more significant for higher levels.

4.1.1 Charge Imbalance

To show that a charge transfer does occur when a transverse level begins to fill, we present the following qualitative argument. Consider the situation where all populated levels are tightly bound, so that the wavefunction overlaps between the different wires are negligible. For convenience of discussion, we assume initially that the potential wells of the quantum wires remain unchanged although the area donor density σ (i.e., the electron filling parameter) increases. In other words, the Fermi energy $E_{\rm F}$ varies with σ but transverse energy levels are independent of σ.

Consider the ratio of the numbers of electrons in wires A and B as a function of σ

$$r(\sigma) = \frac{N_{\rm a}(\sigma)}{N_{\rm b}(\sigma)}, \tag{4.2}$$

where $N_{\rm a}(\sigma)$ and $N_{\rm b}(\sigma)$ are the numbers of electrons in wires A and B at σ, respectively. According to Eq. (2.22), $N_{\rm a}(\sigma)$ and $N_{\rm b}(\sigma)$ can be expressed by

$$N_{\rm a}(\sigma) = L\eta_{\rm a}(\sigma) = \frac{2L}{\pi}\sqrt{\frac{2m^*}{\hbar^2}} \sum_{E_{\ell_{\rm a}} \le E_{\rm F}(\sigma)} \sqrt{E_{\rm F}(\sigma) - E_{\ell_{\rm a}}}, \tag{4.3}$$

and

$$N_{\rm b}(\sigma) = L\eta_{\rm b}(\sigma) = \frac{2L}{\pi}\sqrt{\frac{2m^*}{\hbar^2}} \sum_{E_{\ell_{\rm b}} \le E_{\rm F}(\sigma)} \sqrt{E_{\rm F}(\sigma) - E_{\ell_{\rm b}}}, \tag{4.4}$$

where L is the length of the quantum wires, $\eta_{\rm a}(\sigma)$ and $\eta_{\rm b}(\sigma)$ are the linear densities of electrons in wires A and B, respectively, and $E_{\ell_{\rm a}}$ and $E_{\ell_{\rm b}}$ are the transverse levels belonging to wires A and B, respectively. Note that the Fermi energy $E_{\rm F}$ is a function of σ.

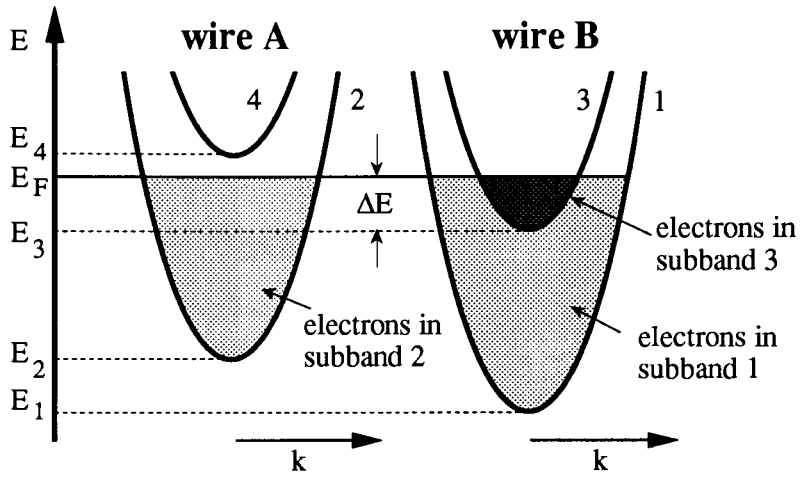

Figure 4.4: Schematic energy level structure of a pair of parallel wires. The horizontal axis is the longitudinal wave vector k and the vertical axis is the subband energy E_{lk}. The parabolic curves are the four lowest subbands. The shaded regions indicate that the corresponding states are populated by electrons.

Suppose when $\sigma = \sigma_0$, $E_{\rm F}(\sigma_0) = E_3$. Thus the ratio of the numbers of electrons in wires A and B is

$$r(\sigma_0) = \frac{N_{\rm a}(\sigma_0)}{N_{\rm b}(\sigma_0)} = \frac{\sqrt{E_{\rm F}(\sigma_0) - E_2}}{\sqrt{E_{\rm F}(\sigma_0) - E_1}}, \tag{4.5}$$

where the populated transverse levels are E_1, which belongs to wire B, and E_2, which belongs to wire A. Suppose that when σ increases from σ_0 by a small amount $\Delta\sigma$, the Fermi energy increases by a small amount ΔE so that it locates above level 3 but still below level 4, as shown in Fig. 4.4. Then, at $\sigma = \sigma_0 + \Delta\sigma$, the numbers of electrons in wires A and B are

$$N_{\rm a}(\sigma_0 + \Delta\sigma) = N_{\rm a}(\sigma_0) + \frac{1}{\pi}\sqrt{\frac{2m^*}{\hbar^2}}\frac{\Delta E}{\sqrt{E_{\rm F}(\sigma_0) - E_2}} \tag{4.6}$$

and

$$N_{\rm b}(\sigma_0 + \Delta\sigma) = N_{\rm b}(\sigma_0) + \frac{1}{\pi}\sqrt{\frac{2m^*}{\hbar^2}}\frac{\Delta E}{\sqrt{E_{\rm F}(\sigma_0) - E_1}} + \frac{2}{\pi}\sqrt{\frac{2m^*}{\hbar^2}}\sqrt{\Delta E}, \tag{4.7}$$

respectively. The last term in Eq. (4.7) is due to level 3, which is a new populated transverse level. The other two terms containing ΔE in Eqs. (4.6) and (4.7) are associated with the 2nd and 1st levels, respectively. Because ΔE is very small, the term due to level 3 in Eq. (4.7)

dominates the other terms. Keeping to the lowest order in ΔE, the ratio of the numbers of electrons becomes

$$r(\sigma_0 + \Delta\sigma) = r(\sigma_0) - r(\sigma_0)\frac{\sqrt{\Delta E}}{\sqrt{E_F(\sigma_0) - E_1}}. \tag{4.8}$$

This equation implies that a charge imbalance occurs when a new transverse level begins to fill.

If σ increases further so that E_F rises above level 4, another term due to level 4 should be added to the expression of r

$$r(\sigma_0 + \Delta\sigma) = r(\sigma_0) - r(\sigma_0)\frac{\sqrt{\Delta E}}{\sqrt{E_F(\sigma_0) - E_1}} + r(\sigma_0)\frac{\sqrt{\Delta E'}}{\sqrt{E_F(\sigma_0) - E_2}}, \tag{4.9}$$

where $\Delta E' = E_F(\sigma_0 + \Delta\sigma) - E_4$. In similar parallel wires, because $E_1 \sim E_2$ and $E_3 \sim E_4$, the last two terms in Eq. (4.9) tend to cancel each other. Because of this cancellation, when σ increases, further differential charging is inhibited and thus the locked levels tend to stay together.

Obviously, the above qualitative argument also applies to situations when higher levels (such as levels 5 and 6) are crossed by the Fermi energy.

The above argument is clearly oversimplified because in reality the electrostatic potentials and thus the transverse energy levels are actually affected by the charge imbalance and move in response to it. Suppose that wire A is deficient in electrons. This means that wire A has an excess of positive charge due to donors, which corresponds to $\Delta\sigma$ of the donor density. The change of the electron potential energy of wire A is mainly due to the excess donors of ribbon A because it is much closer than ribbon B. Then, according to Eq. (2.15), the change of the potential well of wire A at the well center ($x = -s/2 - w_a/2$) can be estimated through

$$\begin{aligned} \Delta V_{\text{eff}}(-s/2 - w_a/2) &\simeq \Delta V_c(-s/2 - w_a/2) \\ &\simeq -\frac{e^2\Delta\sigma}{4\pi\varepsilon\varepsilon_0}\int_{-s/2-w_a}^{-s/2}\int_{-\infty}^{\infty}\frac{dx'dy'}{\sqrt{(x' + s/2 + w_a/2)^2 + y'^2 + d^2}} \end{aligned} \tag{4.10}$$

which gives us a negative correction to the electron potential energy. This means that the potential energy and thus the transverse energy levels of wire A are decreased. In a similar way, we can show that the potential and the transverse energy levels of wire B are increased correspondingly. These electrostatic level shifts are responsible for the energy level locking.

The above qualitative considerations are reflected in our self-consistent numerical results which provide accurate quantitative values for the electron ratio r. In Fig. 4.5, we display

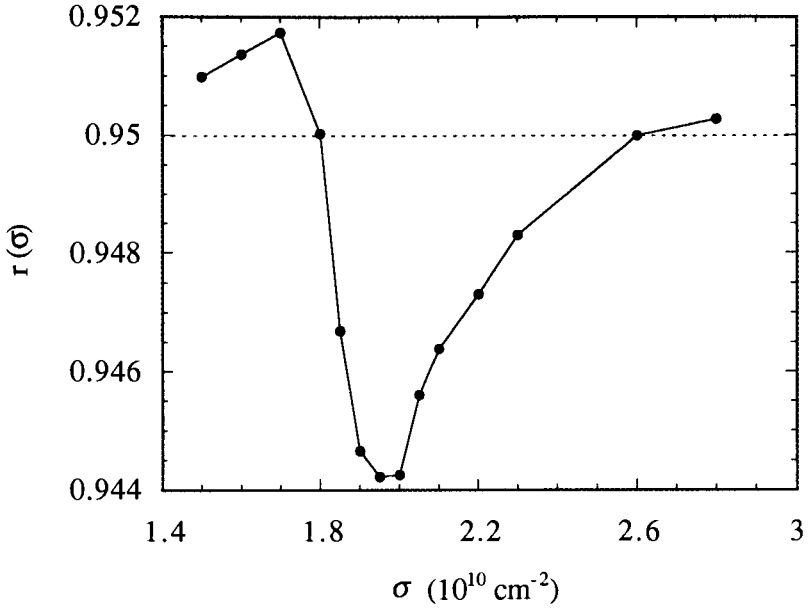

Figure 4.5: Calculated electron number ratio r between the wires. $r_0 = w_a/w_b = 0.95$ corresponds to perfect charge balance. The solid line is a guide to the eye.

our self-consistently calculated ratio r for the range of σ in which the Fermi energy crosses the 5th and 6th transverse levels. Notice that $r_0 = w_a/w_b = 0.95$ corresponds to perfect charge balance between the wires, because we use $w_a = 190$ nm and $w_b = 200$ nm for this calculation. Fig. 4.5 shows that r oscillates about $r_0 = 0.95$. Its drop near $\sigma = 1.8 \times 10^{10}$ cm^{-2} and rise beginning at $\sigma = 2.0 \times 10^{10}$ cm^{-2} are due to the 5th and 6th transverse levels beginning to fill, respectively.

4.1.2 Energy Level Anti-crossing

A charge imbalance occurring due to *high* levels induces an electrostatic potential that acts like an "external field" on *lower* levels. This charge imbalance can cause the corresponding pairs of *lower* levels to lock together or even anti-cross. In Fig. 4.3, when level 5 begins to fill, level 3 and 4 are brought together significantly. On the other hand, levels 1 and 2 anti-cross twice (indicated by the arrows), corresponding to the Fermi energy crossing level 5 and 6, respectively.

Here it is necessary to point out that *exact* level degeneracies do not occur in a system of two parallel quantum wires. The reason is that the density functional equations defining the

Table 4.1: A comparison of the characteristic differences between energy level anti-crossings and lockings.

Anti-crossings	Lockings
single-particle effect	many-particle effect
opening an energy gap	reducing the energy gap
caused by wavefunction overlap	caused by a charge imbalance
level sequence switches	no level sequence switches
occur in all dimension	occur in one dimension

transverse energy levels in our model are effectively one dimensional, and discrete energy levels of one-dimensional systems are never degenerate [158].

In quantum mechanical systems, energy level anti-crossings are very common, such as producing energy gaps in crystalline solids. However, energy level lockings are novel phenomena. The characteristic differences between anti-crossings and lockings are outlined in Table 4.1.

In a particular system, energy level anti-crossings and lockings may coexist. The resultant electronic structure depends on the competition between these two effects. In most situations, the effect of energy level locking is very weak. Our numerical calculations have demonstrated for the first time that the energy level locking can be the dominant effect in some systems, namely, two parallel quantum wires. Further exploration for the energy level locking would be of much interest.

4.1.3 Effect of Wire Separation

An interesting question is how the inter-wire separation s affects the energy level locking in two similar parallel quantum wires. To study this, we have calculated the electronic structure of two similar quantum wires with different wire separation s. The numerical results are shown in Fig. 4.6. The parameters used are $w_a = 190$ nm, $w_b = 200$ nm, $d = 20$ nm, and $\sigma_a = \sigma_b = 2.0 \times 10^{10}$ cm^2, which correspond to the locking of levels 5 and 6 in Fig. 4.3. In Fig. 4.6(a), the solid lines are the eight lowest levels and the dotted line is the Fermi energy. On the right side of this figure, the solid lines ending with solid circles and the dashed lines ending with open circles correspond to the energy levels of isolated wires A and B (each of them is charge-neutral), respectively.

Compared to the gaps between the corresponding levels of the isolated wires, we observe

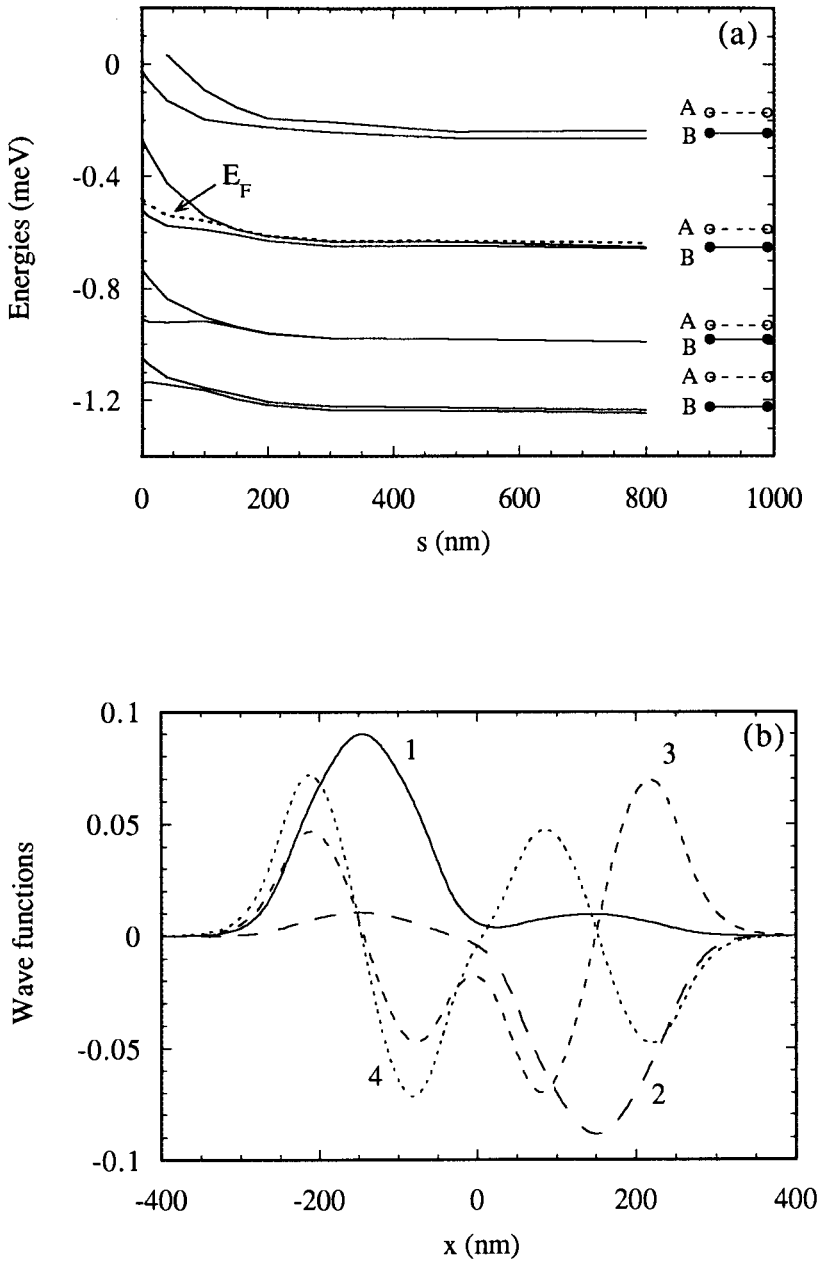

Figure 4.6: (a) Transverse energy levels (solid lines) and Fermi energy (dotted line) against the inter-wire separation s. The solid lines and the dashed lines at the right hand side of the figure correspond to the energy levels of *isolated* wire A and B, respectively. (b) Wavefunctions of the four lowest levels when $s = 100$ nm. Parameters used for both (a) and (b) are $w_a = 190$ nm, $w_b = 200$ nm, $d = 20$ nm, and $\sigma_a = \sigma_b = 2.0 \times 10^{10}$ cm^2.

strong effects of energy level locking for large wire separation. When s is small, however, the inter-wire tunneling becomes strong, which causes the energy levels to become well separated because of wavefunction hybridization. To illustrate the role of the tunneling when s becomes small, we show in Fig. 4.6(b) the wavefunctions of the lowest four levels for $s = 100$ nm. It can be seen that all wavefunctions have considerable amplitudes in both wires. In Fig. 4.6(a), the lower pairs of levels show more tendency to lock together, because the electrons of the lower levels experience a higher effective barrier between wires. Here we should point out that levels 3 and 4 are closer than levels 1 and 2 for large s, because, at this particular value of σ, the order of levels 1 and 2 is reversed (check the wavefunction or refer to Fig. 4.3).

It is interesting to note that, in Fig. 4.6, even for the large wire separation s of 800 nm, the gaps between the paired levels of the two interacting wires are still much smaller than the gaps between the corresponding levels of isolated wires. Thus the energy level locking found in the present model is a quite long-range effect. The reason for this is that the Coulomb energy cost of the charge transfer between infinite parallel wires depends logarithmically on the distance between the wires (for large s), and is thus insensitive to the wire spacing. On the other hand, the tunneling between wires that opposes the energy level locking decreases exponentially as s increases.

Finally, it is necessary to point out that the system of two parallel quantum wires that we consider is not equivalent to two *isolated* quantum wires, even when the wire separation is infinitely large. The reason is that the two parallel quantum wires are correlated so that the whole system has a uniform Fermi energy, even when the wire separation is infinitely large. In experimental devices this comes about because both wires are connected electrically to the same 2DEG that can transfer electrons between the two wires. (See Fig. 1.3.) On the other hand, two isolated quantum wires are both charge-neutral and thus can have different Fermi energies. This is why the energy levels of two correlated quantum wires for large s are quite different from their corresponding levels in the two isolated quantum wires.

4.2 Dissimilar Quantum Wires

The electronic structures of dissimilar quantum wires are quite different from those of similar quantum wires. In Fig. 4.7, we present the calculated electronic structures for two situations in which the ratio of the widths of the two quantum wires are different. For Fig. 4.7(a),

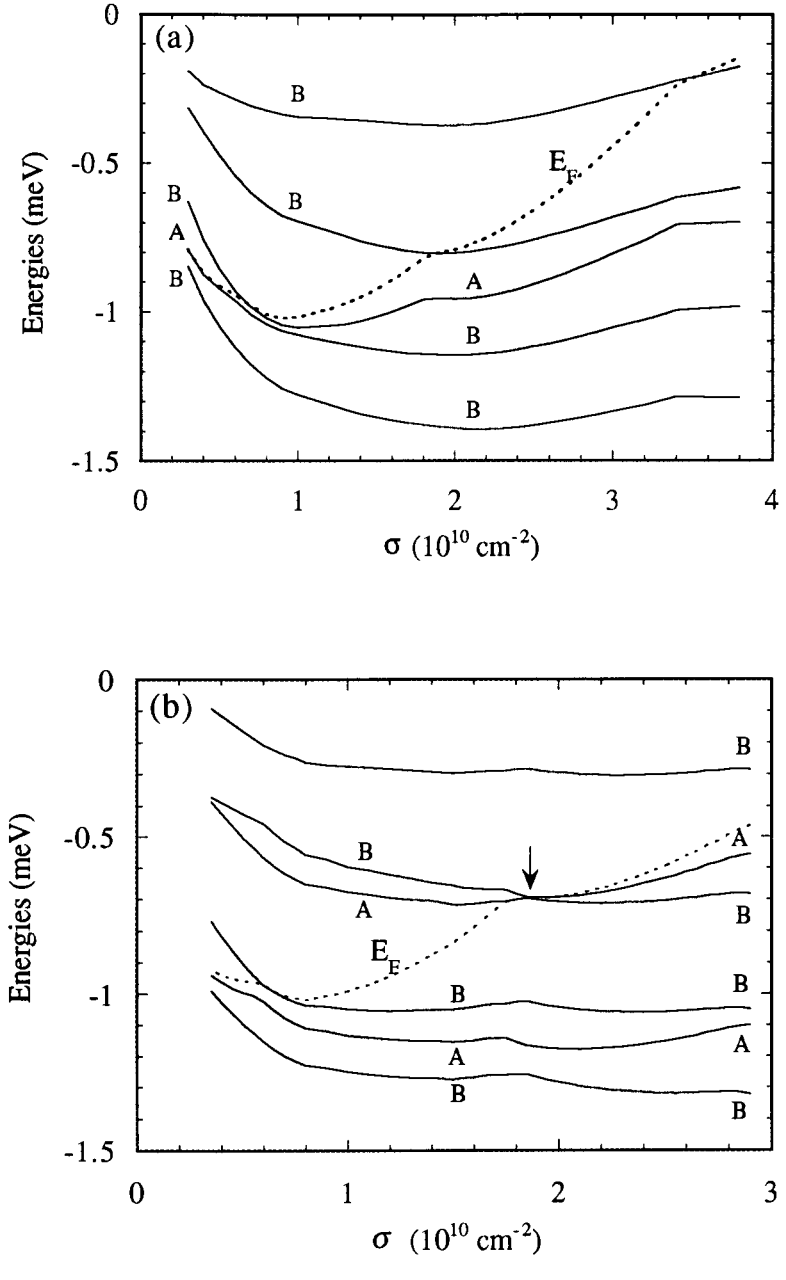

Figure 4.7: The electronic structures of dissimilar parallel quantum wires. (a) $w_a = 50$ nm and $w_b = 200$ nm. (b) $w_a = 100$ nm and $w_b = 200$ nm. Other parameters are $s = 200$ nm and $d = 20$ nm, and $\sigma_a = \sigma_b = \sigma$. The solid lines are the few lowest transverse energy levels, and the dotted line is the Fermi energy. The levels are labeled A or B according to which wire they primarily belong to.

w_a = 50 nm and w_b = 200 nm. For Fig. 4.7(b), w_a = 100 nm and w_b = 200 nm. Other parameters are s = 200 nm, d = 20 nm, and $\sigma_a = \sigma_b = \sigma$ for both calculations. In Fig. 4.7, the solid lines are the few lowest transverse energy levels, and the dotted line is the Fermi energy. The levels are again labeled A or B according to which wire they primarily belong to.

Generally speaking, in dissimilar parallel wires, the transverse levels of the two wires are well separated from each other. When the Fermi energy crosses a transverse level, an abrupt charge imbalance occurs for the same reason as in similar wires. The charge imbalance can significantly "twist" the curves of transverse energy levels, but is not sufficient to lock two levels together. The level twists are seen when the Fermi energy crosses the 3rd and 4th levels in Fig. 4.7(a), and the 3rd, 4th, and 5th levels in Fig. 4.7(b). It is interesting to note that energy levels belonging to different wires are twisted in opposite ways. This is because the two wires have an excess and deficit of electrons, respectively, and thus their energy levels are affected by the charge imbalance in different ways. Moreover, the level twists of wire B are not as significant as those of wire A because wire B is much wider.

However, when a pair of levels happen to be close when the Fermi energy crosses them, they can be squeezed together significantly by the charge imbalance. This is reflected in the crossing between levels 4 and 5 (indicated by an arrow) in Fig. 4.7(b). This energy crossing, however, is a case of *anti-crossing* instead of level locking, because the level sequence reverses. In this case, the charge imbalance narrows the energy gap at the anti-crossing, but the levels then separate quickly.

Another way to study two dissimilar wires is by varying the donor density of one wire while fixing the donor density of the other wire. Such a case is shown in Fig. 4.8. Here, σ_b is varied while σ_a is fixed at 1.5×10^{10} cm^2. The parameters used here are w_a = 190 nm, w_b = 200 nm, s = 200 nm, and d = 20 nm. When σ_b increases, the Fermi energy also increases for the most part. To keep the Fermi energy the same in both wires, some electrons must transfer from wire B to wire A. These excess electrons cause wire A to have a net negative charge, and thus its energy levels rise with increasing σ_b. On the other hand, because wire B is deficient of electrons, its levels fall. Since the levels in wire A increase with the Fermi energy, their trajectories are similar to that of the Fermi energy. The Fermi energy is therefore unlikely to cross the levels of wire A. In other words, the Fermi energy can cross only one level at a time.

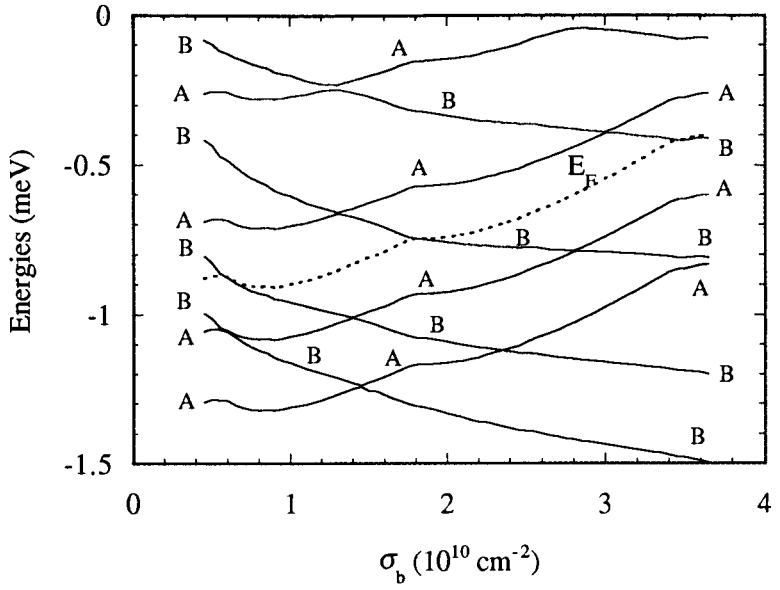

Figure 4.8: σ_b is varied while $\sigma_a = 1.5 \times 10^{10}$ cm^2. The parameters are $w_a = 190$ nm, $w_b = 200$ nm, $s = 200$ nm, and $d = 20$ nm. Levels are labeled A or B according to which wire they primarily belong to.

4.3 Summary and Experimental Implications

Based on above discussion, we summarize the conditions for energy level locking as follows.

1. The system should be quasi-one-dimensional and consist of parallel subsystems with Coulomb interaction.

2. The subsystems should be similar.

3. The separation between the subsystems should be large enough for tunneling between them to be weak.

It should be noted that the quasi-one-dimension condition is essential for energy level locking. To see this, let us consider a quasi-two-dimensional system, such as a system of double quantum wells. Because there is no density of states singularity in two-dimensional systems, corresponding to Eq. (4.7), we now have

$$\Delta N_b = \frac{m^* A}{\pi \hbar^2} \sum_{\ell, E_\ell < E_F} \Delta E, \tag{4.11}$$

where ΔN_b is the variation of the number of electrons in well B, and A is the total area of the quantum wells. Eq. (4.11) implies that all populated levels contribute to ΔN_b *equally.*

In other words, the newly populated level that dominates the filling of electrons in two parallel quantum wires does not have a dominant effect, and thus causes no strong charge imbalance between the subsystems. Therefore, generally speaking, no energy level locking will occur in quasi-two-dimensional systems.

The energy level locking effect can have significant experimental implications. As was mentioned in Chapter 1, in the pioneering measurement of two parallel quantum wires done by Smith *et al.* [20], the total conductance shows successive double steps of $4e^2/h$. It was suggested that these double steps of conductance result from non-random alignments of the wire subbands, and thus imply some correlation between the two quantum wires. Using the energy level locking effect, double steps can be easily explained. Since the transverse levels lock in pairs, the Fermi level crosses two transverse levels at almost the same time. Because each new populated level contributes a single step $2e^2/h$ to the conductance, the total conductance of two parallel wires will show a series of double steps. Note that, however, our numerical calculations show that the energy level locking effect requires the similarity of the two quantum wires. But the relative widths of the two quantum wires used by Smith *et al.* have not been mentioned in their paper [20].

It is also worth considering a recent experimental measurement made by Simpson *et al.* [93] on two parallel quantum wires. In this work, Simpson *et al.* compared the total conductance of two quantum wires to the sum of the two *individual conductances*, but found no significant difference between these. They therefore excluded the possibility of correlations between parallel quantum wires. However, their experiment used special situations in which the two quantum wires can be quite *dissimilar*. Therefore, this experiment is not sufficient to establish whether there is some correlation between *similar* quantum wires or not.

In principle, it should be possible to detect the energy level locking in two similar parallel quantum wires by comparing the total conductance of the two wires to the sum of the conductances of the two individual wires. However, such an experiment must be done with a high accuracy because the effect of energy level locking can be very subtle.

Considering that it is now possible to tune independently several gate voltages applied to quantum wire devices [93, 159, 160, 161], we suggest another possible way to detect the energy level locking effect experimentally. When one tunes one side gate voltage while fixing the other, the widths of plateaus of the total conductance change. Based on our theoretical studies, we know that the locked levels tend to stay together. This feature should make the width of a plateau (for double steps) relatively insensitive to the variation of the gate

voltage *when the plateau width is close to the maximum.* This is because the maximum width of the plateau corresponds to the smallest separation of the two levels, which is the situation of energy level locking.

Besides using the transport properties, other experimental methods such as excitation spectra measurements [39, 117] can in principle be used to verify the existence of energy level locking in two similar parallel quantum wires.

Finally, it should be pointed out that the realistic samples used in experimental measurements [20, 93] are always short gated quantum wires. In the realistic systems, electrons confined between the gates share the same Fermi energy with the electron reservoirs of source and drain, and therefore charge imbalance can be easily achieved by transferring electrons from or to the reservoirs. Also, the lateral confinement of electrons in the gated quantum wires tends to be stronger than in the Coulomb-confined systems, and thus the quantum hybridization that competes with level locking should be less important. Therefore, it is reasonable to expect that energy level locking should occur in the gated quantum wires that have similar widths.

In conclusion for this chapter: We have presented a theoretical study demonstrating that energy level locking should occur in similar parallel quantum wires. The energy level locking is driven by a charge imbalance associated with the onset of filling of transverse energy levels with electrons. This novel phenomenon is qualitatively different from the anti-crossing behavior that is typical of nearly degenerate energy levels in quantum systems. These results should stimulate further experimental and theoretical studies of this phenomenon.

Chapter 5

Split-Gate Quantum Wires: Definition of the Model

We now focus on discussing the realistic split-gate quantum wires, i.e., quantum wires that are fabricated with the split-gate technique. As described in Chapter 1, the split-gate quantum wires have the important advantages of relatively high electron mobilities and of allowing one to vary the confining potential by tuning the gate voltage. Because of these advantages, the split-gate quantum wires have been widely used in experimental studies [18, 19, 20, 22, 24] and may eventually have applications in switches, transistors, and sensors.

Consider the typical split-gate quantum wire whose cross-section is shown in Fig. 5.1. (It is useful to compare Fig. 5.1 with Fig. 1.1 in Chapter 1.) For convenience of discussion, we assume that the quantum wire is infinitely long in the direction perpendicular to the paper. The layers from the top are the GaAs cap, the Si-doped $Al_xGa_{1-x}As$, the undoped $Al_xGa_{1-x}As$ spacer, and the GaAs channel. The thicknesses of the GaAs cap, the Si-doped $Al_xGa_{1-x}As$, and the undoped $Al_xGa_{1-x}As$ spacer are t_c, t_d, and t_s, respectively. On top of the GaAs cap are two metallic gates with a spatial separation w. When a sufficient negative voltage is applied to the gates, electrons are confined laterally to the central region at the $L = t_c + t_d + t_s$ interface, as shown in Fig. 5.1. The coordinate frame is chosen in such a way that the exposed surface of the GaAs cap is the $z = 0$ plane, and the lateral direction is along the x-axis.

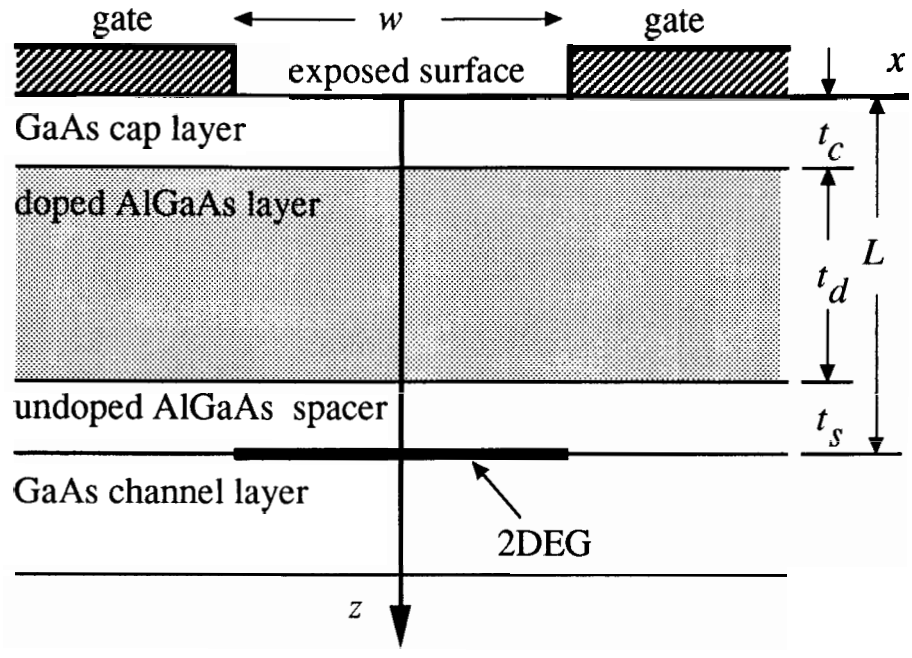

Figure 5.1: The cross-section of a typical split-gate quantum wire and the coordinate frame chosen for calculations.

An essential question about this split-gate quantum wire is how to determine the potential that confines the electrons laterally in the presence of a gate voltage. Here, we need to distinguish two related concepts. One is the *external confining potential* or *bare confining potential*, which does not include the screening by the 2DEG and depends on external conditions.[1] The other concept is the *self-consistent confining potential* or *screened confining potential*, which is the sum of the external confining potential and the 2DEG self-screening. The self-consistent confining potential determines the electronic energy levels of the wire quantitatively, but it has to be calculated numerically using the self-consistent procedures described in Chapter 2. Such numerical calculations are complicated, and the effects of the various properties of the quantum wire are not clearly reflected in the calculations. On the other hand, if the 2DEG is completely depleted, it is possible to obtain a general analytic form of the external confining potential which can provide a lot of insight into realistic quantum wires. In particular, based on this external confining potential, the depletion and

[1]The external conditions refer to the factors not belonging to the 2DEG, such as the gate separation, layer thicknesses, applied gate voltage, etc.

pinchoff voltages (refer to Fig. 1.4 and the relevant text in Chapter 1) can be calculated analytically, which is very useful for experimentalists to improve device performance.

However, the external confining potential (simplified as "confining potential" in following text) depends on many factors such as the details of the donors, surfaces and interfaces, and on whether the system is in equilibrium or not. Therefore, a model must be established to describe these properties.

Based on the assumptions of complete ionization of all donors, a uniform potential on the exposed surface, and overall system equilibrium, Davies [144, 146] suggested a model and calculated the confining potential of quantum wires with the Green's function method. However, his assumptions are oversimplified. Because of the complete ionization of all of the donors that was assumed, his model could not describe the effects of illumination on quantum wires. The assumption of the uniform potential on the exposed surface ceases to be valid when a non-zero gate voltage is applied, because the surface electrons are very localized. Moreover, the overall system equilibrium does not always hold because of the high energy barrier that is involved in quantum wires. Due to these limitations, the qualitative results obtained within Davies' model do not agree with experimental measurements satisfactorily [144]. (We will have more discussion on this in the next chapter.)

In this chapter, we will establish a *new* model of split-gate quantum wires which incorporates the crucial properties of donors, surfaces and interfaces, and considerations of system equilibrium that apply in different situations. In each of the following sections, we first present a feature of our model and then provide explanations and arguments in support for that feature. Most of the results presented in this chapter have been published in Ref. [35].

5.1 Feature I: Donors

The first feature of our model incorporates the following properties of the donors:

1. The Si donors in the doped $Al_xGa_{1-x}As$ layer are uniformly distributed. Electrons can be trapped in both the shallow levels and deep levels of the Si donors.

2. Electrons in the shallow levels can be easily excited to the conduction band, because the binding energy for the shallow levels is small.

3. Electrons in the deep levels can be excited to the shallow levels or to the conduction band by illumination.

In fabricating quantum wires, it is possible to ensure that almost all the Si atoms in the doped $Al_xGa_{1-x}As$ layer take the Ga sites and are thus donors of electrons. In this theoretical study, we assume that all of the Si donors are uniformly distributed in the doped $Al_xGa_{1-x}As$ layer.

The Si donors are associated with two kinds of localized states: the *shallow levels* and the *deep levels*. We now review the properties of these two kinds of localized states separately.

5.1.1 Shallow Levels

In $Al_xGa_{1-x}As$, the three electrons in the outmost shell of Ga atoms or Al atoms join the five electrons in the outmost shell of As atoms to form the tetrahedral chemical bonds of the zincblende-type crystal. When a Si atom replaces a Ga or Al atom, there will be an extra electron at the Si site because the Si atom has four electrons in its outmost shell. This extra electron is called a *donated electron*. Because the valence band of $Al_xGa_{1-x}As$ is completely filled, the donated electron has to occupy the conduction band. However, after donating an electron, the Si donor is associated with a positive charge $+e$. This charge can attract the electron into a series of hydrogenic-like bound states, which are called *shallow levels*. In the effective mass theory [122], neglecting central cell effects, the energies of the shallow levels are given by

$$E_s(n) = -\frac{m^* e^4}{2(4\pi\varepsilon\varepsilon_0\hbar n)^2} = -\frac{1}{\varepsilon^2 n^2}\left(\frac{m^*}{m_e}\right)(\text{Ryd}), n = 1, 2, 3, \cdots, \tag{5.1}$$

where m^* is the effective mass of electron, ε is the dielectric constant, and 1 Ryd = 13.6 eV.

The shallow levels of a Si donor have very small energy spacings. To see this, we define the *binding energy* of the shallow levels as

$$E_b = -E_s(1) = \frac{1}{\varepsilon^2}\left(\frac{m^*}{m_e}\right)(\text{Ryd}). \tag{5.2}$$

For $Al_xGa_{1-x}As$, as long as $x < 0.45$, the Γ valley (at the center of the first Brillouin zone) is the lowest one of the conduction band, and the effective mass of electrons in the Γ valley is $m^* = 0.067\ m_e$. For the $Al_xGa_{1-x}As$ used in quantum wires, $x \sim 0.3$ usually, so we should use $m^* = 0.067\ m_e$. If we take the dielectric constant for $Al_xGa_{1-x}As$ and GaAs to be $\varepsilon = 12.5$, we obtain that $E_b = 5.83$ meV. Such a binding energy of shallow Si donors has been verified by various experiments [162, 163].[2]

[2] In reality both m^* and ε depend weakly on x in $Al_xGa_{1-x}As$.

Because of the small binding energy of the shallow levels, electrons can be easily excited from the shallow levels to the conduction band. In following discussion, we will neglect the binding energy of the shallow levels because it is much smaller than other relevant energy parameters such as the surface Schottky barrier (Φ_{ssb} ~0.8 eV) and the GaAs-$Al_xGa_{1-x}As$ conduction band offset (ΔE_c ~0.2 eV), as shown in Table 1.1 in Chapter 1.

5.1.2 Deep Levels

In $Al_xGa_{1-x}As$, when $x > 0.2$, electrons can be trapped by Si donors in other kinds of localized states that are associated with much larger binding energies. These levels are called *deep levels.* (For a recent review see [164].) It is now generally accepted [165, 166, 167, 168] that the deep levels are associated with a local lattice distortion which is usually called a *DX center.* The microscopic structure of a DX center has been suggested [168] as shown in Fig. 5.2(a). On the left hand side is the undistorted lattice structure of a Si atom and its neighbors in $Al_xGa_{1-x}As$. On the right hand side is a distorted DX center, where one bond between Si and As is broken and the Si atom moves toward the interstitial site. (It is widely believed [164] that electron transfer occurs between deep donors so that they exist as pairs DX^+ and DX^- of positively and negatively charged ions. Since these pairs are charge neutral overall, in this thesis we will treat such deep donors as if they were un-ionized.)

According to Ref. [166], the relationship between the deep levels and shallow levels can be described by the energy diagram in Fig. 5.2(b). The two parabola-like energy curves correspond to a shallow level and a deep level, as indicated in the figure, as functions of a configuration coordinate which represents the lattice distortion. A stable deep level corresponds to the minimum point A of the right-hand curve, which involves a lattice distortion K_0. A stable shallow level corresponds to the minimum point C of the left-hand curve, which involves no lattice distortion. The deep level is lower in energy than the shallow level. In Fig. 5.2(b) one can see three major processes. In the process of *photon absorption*, an electron is excited from point A to point B by absorbing a photon ($h\nu \geq 1.0$ eV) [169] while the lattice distortion is unchanged. However, the system at point B is not stable. The lattice distortion transforms into phonons and disappears, which corresponds to a relaxation of the system from point B to point C, which is labeled *relaxation.* In the process of *thermal distortion*, an electron transfers from point C to point A, which involves crossing an energy barrier $\Delta E \sim 0.1$ eV [165] and introducing the lattice distortion K_0. At low temperatures ($T < 1$ K), however, the thermal distortion is suppressed because there are not sufficient

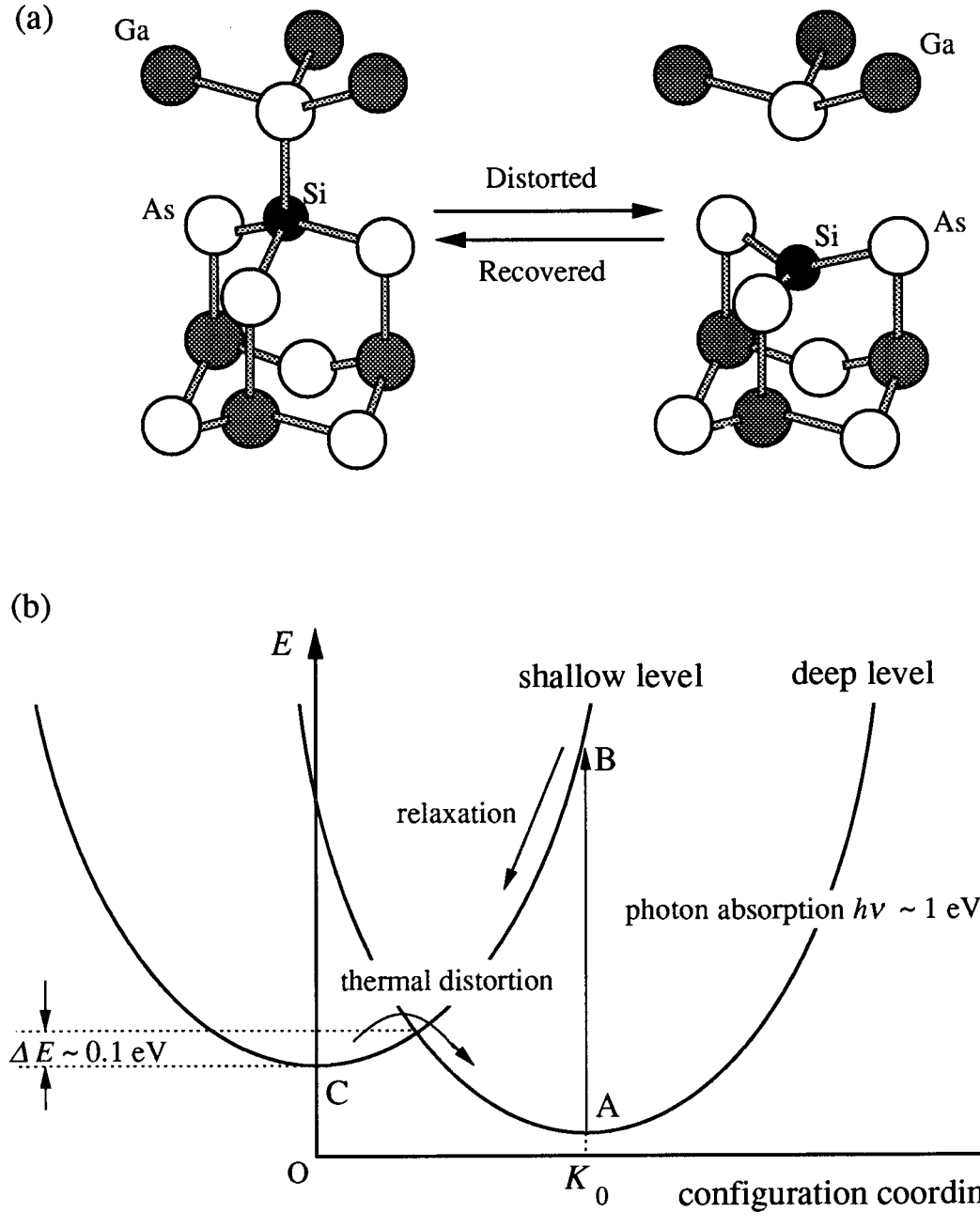

Figure 5.2: The relationship between the shallow levels and deep levels. (a) The microscopic structures of the undistorted lattice (left) and a DX center (right), as per reference [168]. (b) A shallow level and a deep level as functions of the configuration coordinate, and the three relevant processes of photon absorption, relaxation, and thermal distortion, as per reference [166].

phonons present to overcome the energy barrier. It is found that the thermal distortion from the shallow levels to the deep levels is significant only when $T > 100$ K. [170] The above picture of the deep levels and shallow levels is well supported by many experiments such as persistent-photoconductivity, thermal emission, and deep level transient spectroscopy (DLTS). [165, 166, 167, 169, 170]

According to the first property of Feature I of our model, in the doped layer of the quantum wire, we have

$$N_{\text{total}} = N_{\text{s}} + N_{\text{d}}, \tag{5.3}$$

where N_{total}, N_{s}, and N_{d} are the total concentration of donors, and the concentrations of donors in the shallow levels and in the deep levels, respectively. Note that according to Feature I the ionized[3] donors are included here in N_{s}. In principle, N_{total} is known from fabrication information but N_{s} and N_{d} are undetermined. Because electrons in the deep levels can be excited to the shallow levels or to the conduction band by illumination, N_{s} and N_{d} are changed when the sample is illuminated. The uncertainty of N_{s} makes it difficult to analyze the quantum wire, because N_{s} determines the number of donated electrons as well as spatial charge density. However, we will develop a method to calculate N_{s} within our model in the next chapter.

5.2 Feature II: Surfaces and Interfaces

Feature II incorporates the following properties of surfaces and interfaces in the split gate quantum wire into the model:

1. The Fermi level of the exposed GaAs surface is pinned at the surface states within the band gap. The surface states are localized.

2. The interface Schottky barrier between GaAs and metallic gates depends on the gate metal.

3. The GaAs-$Al_xGa_{1-x}As$ interfaces induce an abrupt conduction band offset, which depends on the Al composition in $Al_xGa_{1-x}As$.

[3] Note that we treat deep donors as un-ionized species througthout this work as discussed on page 73.

5.2.1 GaAs Surfaces

Generally speaking, semiconductor surfaces are quite complicated because of the rich variety of possible combinations of bulk materials, lattice reconstructions, and surface contaminations. (For a general review see [171].) Fortunately, we only need to deal with the properties of the exposed GaAs surfaces in the split-gate quantum wire shown in Fig. 5.1. The exposed surface in the quantum wire is usually the GaAs(100) surface for reasons related to the growth method that uses MBE or OMCVD [11, 12].

After the split-gate quantum wire is fabricated, the exposed GaAs surface is usually contaminated by oxygen or other atoms. [172] Many experimental studies [173, 174] of contaminated GaAs surfaces show that the surface Fermi energy is pinned at the surface states within the forbidden gap when the surface is covered by a fraction of monolayer of adatoms. In other words, the location of the Fermi energy relative to the band edges is independent of concentration of donors in the bulk GaAs. This surface behavior is called the *Fermi-level pinning effect.* Experiments [173] show that the pinning position of the Fermi energy is insensitive to the types of adatoms. It is thought [173, 175] that the surface states at the contaminated surfaces are associated with the adatom-induced surface defects. The surface states are very localized, which can be understood from the fact that energies of the surface states have a small dispersion. [173, 174]

An important parameter related to the exposed surface is the *surface Schottky barrier*, which is defined as the energy difference between the conduction band minimum and the surface states

$$\Phi_{\rm ssb} = E_{\rm cbm} - E_{\rm surf}. \tag{5.4}$$

In n-type GaAs, some of the donated electrons transfer to the surface states and the positively ionized donors cause energy bands to bend in the GaAs. (See Fig. 5.3(a).) Based on experimental measurements [176, 177, 178], the surface Schottky barrier for the n-type "exposed" GaAs(100) surface is approximately $\Phi_{\rm ssb} = 0.8$ eV. For the split-gate quantum wire shown in Fig. 5.1, although the GaAs cap is not doped, the Si-doped $Al_xGa_{1-x}As$ layer makes the exposed surface behave like a n-type GaAs surface. Therefore, in our calculations that follow, we will use $\Phi_{\rm ssb} = 0.8$ eV as the value of the surface Schottky barrier for the exposed GaAs(100) surface of the quantum wire.

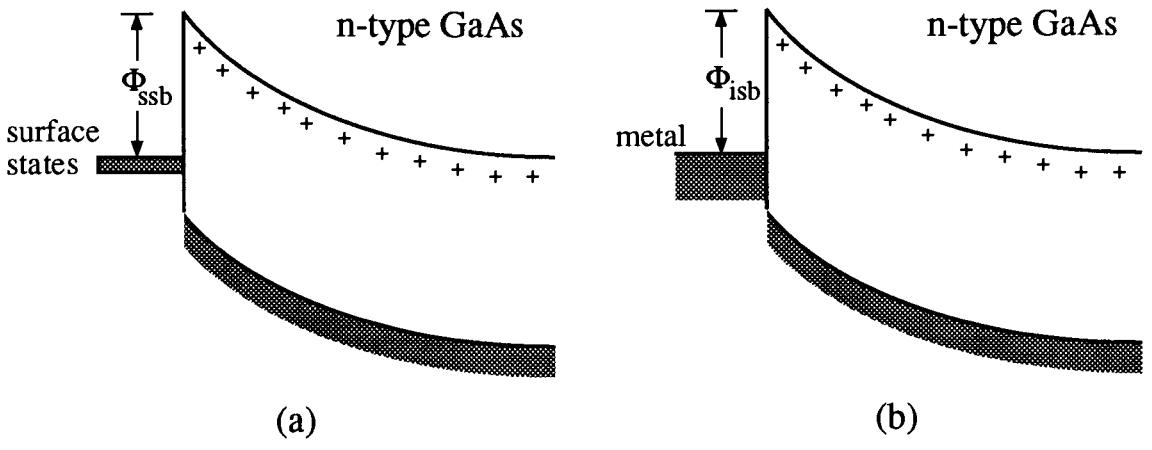

Figure 5.3: A comparison between (a) the surface Schottky barrier of a n-type GaAs and (b) the interface Schottky barrier between a metal and the n-type GaAs.

5.2.2 Metal-GaAs Interfaces

Metal-semiconductor interfaces have been studied for a long time and are well understood. (For a general review see [171].) An important parameter for metal-semiconductor interfaces is the *interface Schottky barrier*. For n-type GaAs, it is defined as the energy difference between the conduction band minimum of the GaAs and the Fermi level of the metal,

$$\Phi_{\rm isb} = E_{\rm cbm} - E_{\rm F}. \tag{5.5}$$

Note that the Fermi level of the metal locates within the band gap of GaAs, as shown in Fig. 5.3(b). The metal-GaAs interface is associated with *interface states* or *metal-induced gap states* (MIGS), which are caused by the Bloch wavefunctions in the metal extending into the GaAs [179]. Electrons donated from the n-type GaAs can therefore be trapped by the interfaces states, and the energy bands are bent in the GaAs correspondingly, as shown in Fig. 5.3(b).

There is a strong similarity between the *interface* Schottky barrier and the *surface* Schottky barrier. They are both associated with electronic states within the band gap, and can cause band bending when electrons are trapped by the states within the band gap. Therefore, the relevant theoretical analysis can be the same. However, the values of the *interface*

Schottky barrier and the *surface* Schottky barrier for n-type GaAs are not necessarily the same, because the mechanisms that cause the two kinds of energy barriers are not the same. In particular, there has been no generally accepted model for surface states at contaminated semiconductor surfaces, and this problem is still in process of investigation. For a detailed picture, see Ref. [171].

It has been found that the interface Schottky barrier depends on the contact metal. In Table 5.1, we list the experimental values of the interface Schottky barriers for different metals on the n-type GaAs(100), based on both current-voltage and capacitance-voltage measurements [180, 181, 182]. For most metals, the values of interface Schottky barriers from the I/V and C/V measurements are quite similar. Here, it is worth mentioning that good agreement has been achieved between theoretical calculations [183] and experimental measurements for some interface Schottky barriers.

Table 5.1: Interface Schottky barriers for various metals on n-type GaAs(100). All values are in eV.

Metal	Ag	Au	Pd	Cu	Al	Ti	Pb	Bi	Fe	Mg
I/V	0.90	0.89	0.91	0.96	0.85	0.83	0.80	0.77	0.72	0.62
C/V	0.89	0.87	0.93	0.96	0.84	0.83	0.91	0.79	0.75	0.66

5.2.3 GaAs-AlGaAs Interfaces

The interfaces between GaAs and $Al_xGa_{1-x}As$ introduce abrupt discontinuities of the energy bands. (For a recent review, see Ref. [184].) In studying quantum wires, we only need to consider the *conduction* band offsets at the GaAs-$Al_xGa_{1-x}As$ interfaces because the valence band is completely filled and is thus irrelevant to the properties of the quantum wires that are discussed in this thesis.

There are many experimental measurements [185, 186, 187] of the conduction band offsets at the GaAs-$Al_xGa_{1-x}As$ interfaces. It is found that the conduction band offset ΔE_c depends on the Al composition x of the $Al_xGa_{1-x}As$, and the dependence is approximately linear when $x < 0.45$. For most GaAs-$Al_xGa_{1-x}As$ quantum wires, $x \sim 0.3$. Correspondingly, we will use $\Delta E_c = 0.2$ eV in relevant calculations.

5.3 Feature III: Equilibrium Considerations

Feature III of our model consists of assumptions about the different equilibrium and non-equilibrium situations that can occur in quantum wires:

1. When the quantum wire is in absolute equilibrium, there are three different equilibrium regimes.

2. We assume that electrons on both sides of the spacer layer are always in equilibrium because the spacer energy barrier is small. However, the surface energy barrier is so high that the Fermi energy of surface electrons can be different from the Fermi energy of the rest of the electrons in the system.

3. We assume that the whole system is in absolute equilibrium after the quantum wire has just been fabricated or has just been illuminated at zero gate voltage.

4. When the gate voltage varies, the number of surface electrons is conserved.

5.3.1 Absolute Equilibrium

Absolute equilibrium means that the Fermi energy is uniform within the whole system of the quantum wire. Under the conditions of absolute equilibrium, we identify three different equilibrium regimes at zero gate voltage. The energy band structures for these three equilibrium regimes are shown in Fig. 5.4. The curves corresponds to the bottom of conduction band along the z-axis. Note that we have neglected the binding energy of the shallow levels as per Feature I.

Three Equilibrium Regimes

In equilibrium regime A (Fig. 5.4(a)), the shallow Si donors everywhere in the doped layer are ionized, but no 2DEG is present at the $z = L$ interface. This means that all of the electrons donated by the shallow donors have transferred to the $z = 0$ plane to fill the surface or interface states. This lowers the system's energy because the conduction band edge of the GaAs channel layer is higher than the surface and interface energy levels. Due to this transfer of electrons, the conduction band is bent in the GaAs cap and doped $Al_xGa_{1-x}As$ layers. The electrons accumulated at the $z = 0$ plane effectively form a "capacitor" with the positively ionized donors. Therefore, the conduction band in the undoped $Al_xGa_{1-x}As$

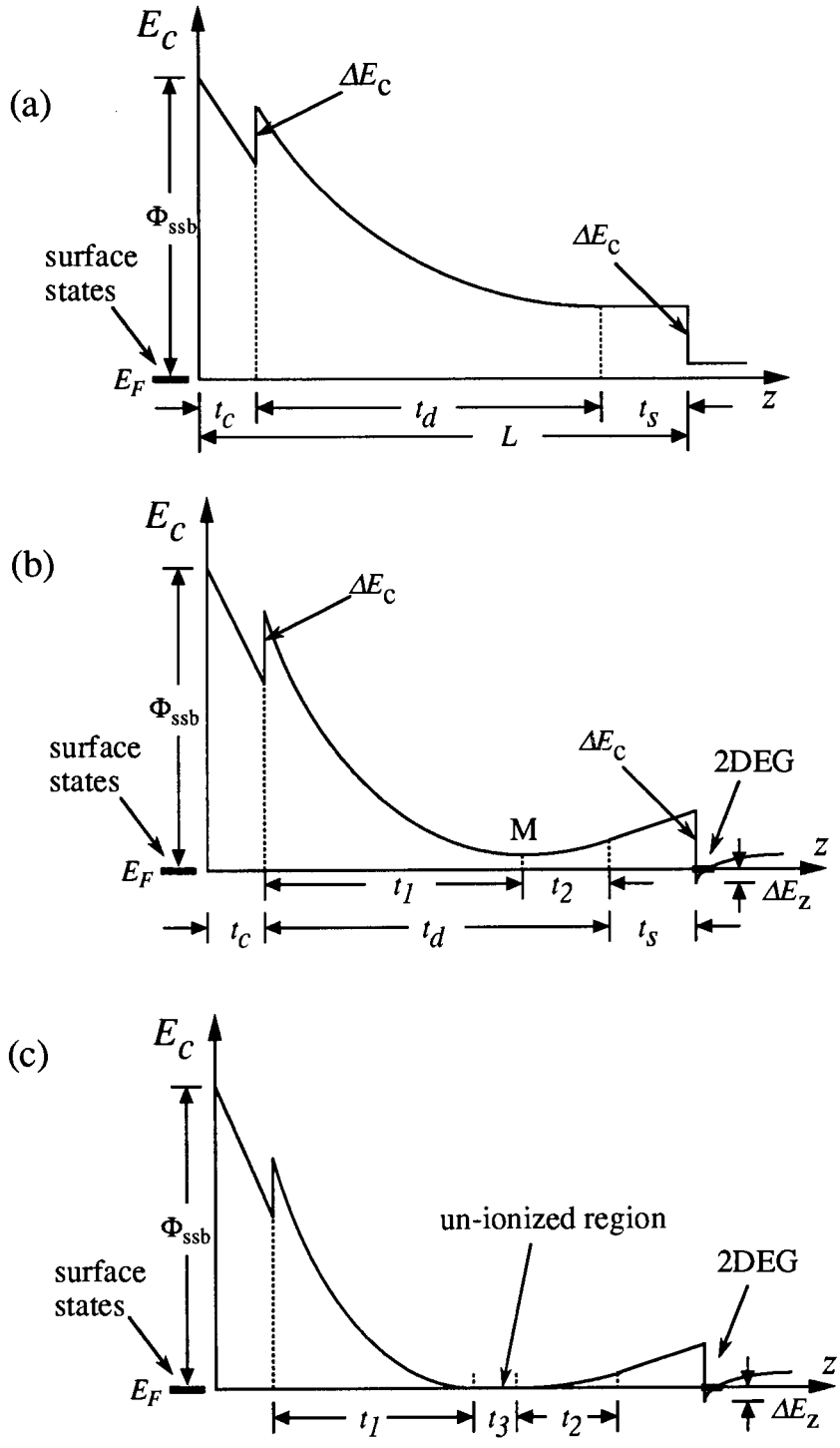

Figure 5.4: The energy band structures for the three equilibrium regimes when the quantum wire is in absolute equilibrium at zero gate voltage. (a) Equilibrium regime A. (b) Equilibrium regime B. (c) Equilibrium regime C.

and the GaAs channel layers remains flat. Equilibrium regime A occurs when the shallow donor density is very low and the layer thicknesses t_c and t_d are small.

In equilibrium regime B (Fig. 5.4(b)), the shallow donors everywhere in the doped layer are ionized and a 2DEG is present at the $z = L$ plane. Now the curved conduction band within the doped $Al_xGa_{1-x}As$ layer has a minimum point M which divides the whole doped layer into two parts, with thicknesses t_1 and t_2, respectively. Because the electric field at point M is zero, one may consider all of the donated electrons from the region to the left of point M to transfer to the $z = 0$ plane to form one "capacitor", while all of the donated electrons to the right of point M transfer to the $z = L$ plane to form another "capacitor". These two "capacitors" have no interaction with each other because each screens itself completely. This consideration enables us to discuss each "capacitor" separately. Equilibrium regime B occurs when the shallow donor density is moderate.

Equilibrium regime C (Fig. 5.4c) is the most complicated one. It differs from regime B by the presence of an *un-ionized region* in the doped layer. In this un-ionized region, the shallow levels of the donors line up with the system's Fermi level and electrons in this region are not ionized (i.e., the electrons can be regarded as being bound to the shallow donors.). Correspondingly, the whole doped $Al_xGa_{1-x}As$ layer is divided into three parts. The one on the left hand side forms one "capacitor" with the $z = 0$ electrons, the one on the right hand side forms another "capacitor" with the 2DEG, and the one in the middle is charge-neutral with a flat conduction band. Equilibrium regime C occurs when the shallow donor density is very high or the doped layer is very thick.

Identification of the Equilibrium Regimes

In calculating the confining potential of a split-gate quantum wire, it is important to know which of the equilibrium regimes the system is in when the quantum wire is in absolute equilibrium at zero gate voltage. However, the equilibrium regimes *under the exposed surface* and *under the gates* can be different from each other because the GaAs surface Schottky barrier Φ_{ssb} and the metal-GaAs interface Schottky barrier Φ_{isb} can be different (see Feature II.). This makes theoretical studies somewhat more complicated. Here we provide the criteria for identifying the equilibrium regimes *under the exposed surface* ($|x| < w/2$). The identification of the equilibrium regimes *under the gates* ($|x| > w/2$) can be done in a similar way.

Let N_α be the critical shallow donor density that divides regimes A and B, and N_β be the

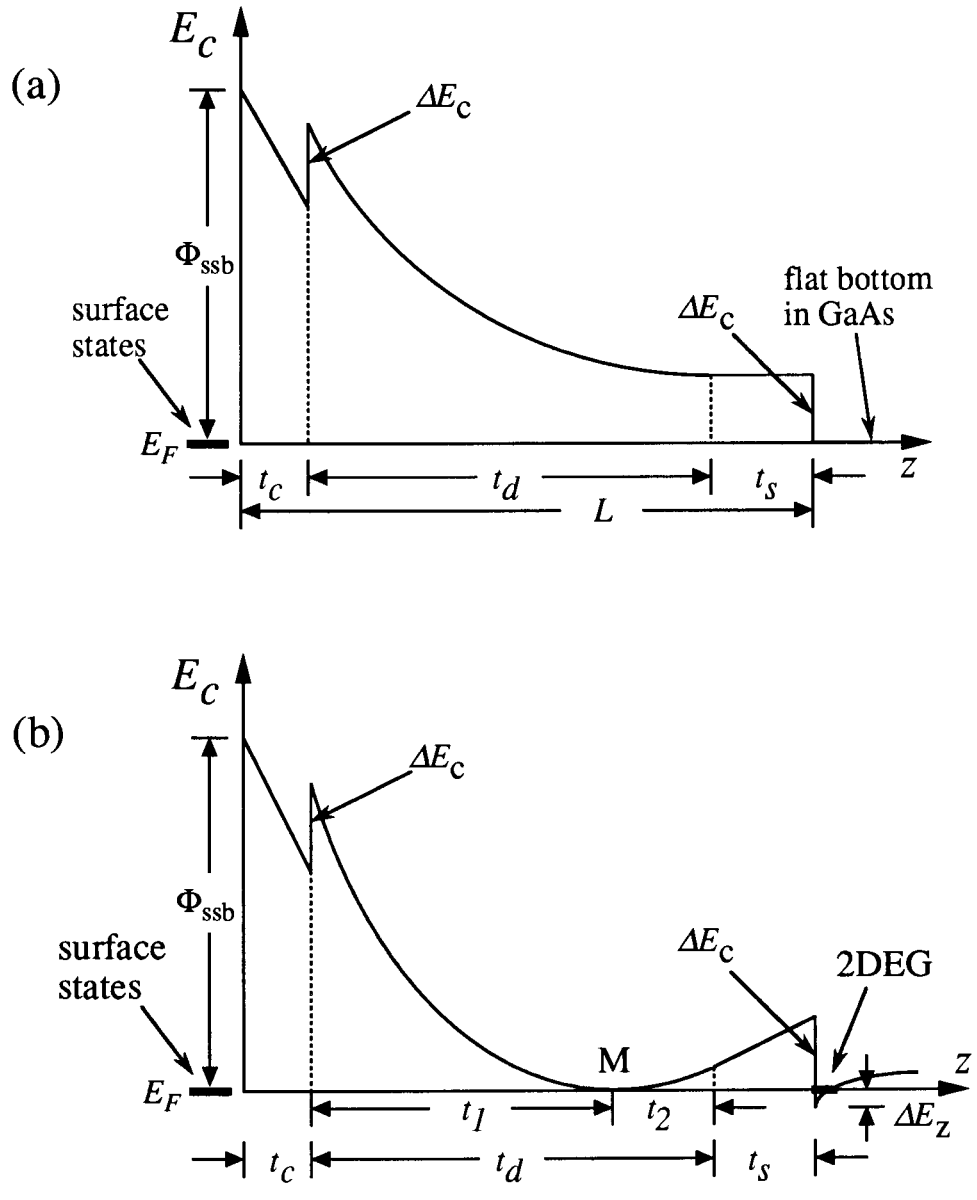

Figure 5.5: (a) The critical situation between equilibrium regimes A and B. (b) The critical situation between equilibrium regimes B and C.

one that divides regimes B and C. At N_α, the conduction band bottom in the GaAs channel layer lines up exactly with the system's Fermi level, which also lines up with the surface energy levels. (See Fig. 5.5(a).) Considering that the width of the exposed surface, i.e., the gate separation (w>100 nm), is much larger than the thickness the cap layer ($t_c \sim 10$ nm), we can neglect the edge effects of the "capacitor" formed by the surface electrons and the ionized donors in the doped layer. Thus,

$$\frac{e^2 N_\alpha}{\varepsilon\varepsilon_0}(t_c t_d + \frac{t_d^2}{2}) = \Phi_{ssb}, \tag{5.6}$$

in which the left side gives the total amount of band bending in the cap and doped layers. Note that the two band offsets at $z = t_c$ and $z = L$ cancel each other. For a particular quantum wire, t_c, t_d, and Φ_{ssb} are known, and therefore the critical shallow density N_α can be calculated from Eq. (5.6) directly.

When $N_s = N_\beta$, the minimum point M of the curved conduction band in the doped layer just touches the Fermi energy, as shown in Fig. 5.5(b). Therefore,

$$\frac{e^2 N_\beta}{\varepsilon\varepsilon_0}(t_c t_1 + \frac{t_1^2}{2}) = \Phi_{ssb} + \Delta E_c, \tag{5.7}$$

$$\frac{e^2 N_\beta}{\varepsilon\varepsilon_0}(t_s t_2 + \frac{t_2^2}{2}) = \Delta E_c - \Delta E_z, \tag{5.8}$$

$$t_1 + t_2 = t_d, \tag{5.9}$$

where Eqs. (5.7) and (5.8) correspond to the bottom of the conduction band at point M, being equal to the Fermi levels of the surface states and the 2DEG, respectively. In the above three equations, N_β, t_1, and t_2 are the three unknown parameters to be solved for. Note that ΔE_z is the energy difference between the 2DEG Fermi energy and the bottom of the conduction band at $z = L$ (refer to Fig. 5.4c). Typically $\Delta E_z \sim 40$ meV.

At this critical shallow donor density, the corresponding area density of surface electrons at $z = 0$ is

$$\sigma_\beta = N_\beta t_1, \tag{5.10}$$

and the area density of the 2DEG at $z = L$ is

$$n_\beta = N_\beta t_2. \tag{5.11}$$

For a particular quantum wire, we can identify its equilibrium regime by comparing its actual shallow donor density N_s to its critical values N_α and N_β, which are calculated

Table 5.2: The criteria for identifying different equilibrium regimes under the exposed surface at zero gate voltage.

Equilibrium regime	By shallow donor density N_s	By 2DEG density n_0
A	$N_s < N_\alpha$	$n_0 = 0$
B	$N_\alpha < N_s < N_\beta$	$0 < n_0 < n_\beta$
C	$N_s > N_\beta$	$n_0 > n_\beta$

above. However, as a part of N_{total}, N_s is usually not known directly. On the other hand, the 2DEG area density n_0 at zero gate voltage can readily be determined experimentally from transport measurements. (The density of the 2DEG is usually measured from edge state backscattering experiments [190, 191] at various gate voltages, and n_0 can be obtained by extrapolating the 2DEG densities at non-zero gate voltages to zero gate voltage.) Therefore, it is more convenient to work in terms of the comparison between n_β and n_0. The conditions for different equilibrium regimes *under the exposed surface* are listed in Table 5.2.

Note that, by replacing the surface Schottky barrier Φ_{ssb} by the interface Schottky barrier Φ_{isb} in Eqs. (5.6) and (5.7), we can calculate the critical parameters for the equilibrium regimes *under the gates.*

Determination of N_s

The shallow donor density N_s can be calculated from the measured n_0, the area density of 2DEG at zero gate voltage, through the relationship between N_s and n_0. The relationship between N_s and n_0 depends on which the equilibrium regime the quantum wire is in at zero gate voltage.

If the quantum wire is in equilibrium regime B (refer to Fig. 5.4(b)), then the shallow donor density N_s is obtained by solving the following equations

$$\frac{e^2 N_s}{\varepsilon\varepsilon_0}(t_c t_1 + \frac{t_1^2}{2}) - \frac{e^2 N_s}{\varepsilon\varepsilon_0}(t_s t_2 + \frac{t_2^2}{2}) = \Phi_{\text{ssb}} + \Delta E_z, \tag{5.12}$$

$$t_1 + t_2 = t_d, \tag{5.13}$$

$$N_s t_2 = n_0, \tag{5.14}$$

where t_1 and t_2 have been shown in Fig. 5.4(b). These equations are based on the condition that the surface Fermi energy level is equal to that of the 2DEG. Note that, with N_s and t_1 evaluated from above equations, we can also calculate the area density of electrons at the

exposed surface through

$$\sigma_0 = N_s t_1, \tag{5.15}$$

which is assumed to be uniform at zero gate voltage. This result will be used in calculating the pinchoff voltage in Chapter 6.

If the quantum wire is in equilibrium regime C (refer to Fig. 5.4(c)), then N_s should be calculated from

$$\frac{e^2 N_s}{\varepsilon\varepsilon_0}(t_s t_2 + \frac{t_2^2}{2}) = \Delta E_c - \Delta E_z, \tag{5.16}$$

$$N_s t_2 = n_0, \tag{5.17}$$

where only N_s and t_2 are not known in the above two equations. Note that the first equation comes from the fact that the Fermi level of the 2DEG is equal to the energy level of the shallow donors in the un-ionized region in the doped layer. (See Fig. 5.4(c).) Similarly, because of the equality of the Fermi level of the surface states and the energy level of shallow donors in the un-ionized region, we have

$$\frac{e^2 N_s}{\varepsilon\varepsilon_0}(t_c t_1 + \frac{t_1^2}{2}) = \Phi_{ssb}, \tag{5.18}$$

which gives t_1. Therefore, we can calculate the area density of surface electron at zero gate voltage through

$$\sigma_0 = N_s t_1, \tag{5.19}$$

and the thickness of the un-ionized region in the doped layer through

$$t_3 = t_d - t_1 - t_2. \tag{5.20}$$

5.3.2 Partial Equilibrium

As shown in Fig. 5.4, energy barriers due to the surface Schottky barrier and the spacer separate the electrons of the 2DEG from those at the exposed surface, and those in the un-ionized region. Considering that conductance measurements [18, 19, 20, 22, 24] are performed at very low temperatures ($T \leq 1$ K), we face the question whether or not we should consider the whole system to be in absolute equilibrium.

To answer this question, we suppose that there are Fermi-level differences between the electrons in the different regions in a quantum wire (see Fig. 5.6(a)), and estimate the flux of electrons across the energy barriers. If the flux crossing an energy barrier is so large

that the electron densities on both sides of the barrier can change quickly, then we should consider that electrons on both sides of the barrier to be in equilibrium. On the other hand, if the flux is so small that it has almost no effect on the electron densities on the appropriate time scale, then we should assume that electrons on both sides of the barrier can have different Fermi energies. At low temperatures, the thermal activation of electrons is negligible. Therefore, we only need to investigate the flux of electrons due to tunneling through the energy barriers.

For the purpose of this analysis, let us consider an arbitrary one-dimensional energy barrier which separates two electron gases. (See Fig. 5.6(b).) The Fermi energy difference between the two electron gases is ΔE. Now let us calculate the electron flux that tunnels through the energy barrier because of the Fermi energy difference ΔE. (For a general review of calculations of tunneling fluxes, see Ref. [188].)

Since we are only interested in qualitative estimates, we will calculate, for simplicity, the tunneling fluxes assuming that the electrons on either side of the barrier are ideal electron gases. (See Fig. 5.6(b).) The electron energies can then be written as

$$E = E_z + E_{||}(\mathbf{k}_{||}) = \frac{\hbar^2 k_z^2}{2m} + \frac{\hbar^2 k_{||}^2}{2m}, \tag{5.21}$$

where E_z and k_z are the energy and wavevector for the z-direction, and $E_{||}$ and $\mathbf{k}_{||}$ are the energy and wavevector for the direction parallel to the barrier, i.e. perpendicular to the z-direction.

For the state (k_z, $\mathbf{k}_{||}$) on the left side with $k_z > 0$, the electron flux per k_z state tunneling through the energy barrier is

$$j(k_x, \mathbf{k}_{||}) = j(k_z) = T(E_z) j_0(k_z), \tag{5.22}$$

where $T(E_z)$ is the transmission probability for an electron with energy E_z to tunnel the energy barrier, and $j_0(k_z)$ is the incoming flux for a k_z state. For free electrons, $j_0(k_z)$ can be expressed by

$$j_0(k_z) = v_z(k_z) = \frac{\hbar k_z}{m} = \frac{1}{\hbar}\frac{\partial E_z}{\partial k_z} = \frac{1}{\hbar}\frac{\partial E}{\partial k_z}. \tag{5.23}$$

Therefore, the total tunneling flux per unit area is given by

$$J = \frac{2}{(2\pi)^3 \hbar} \iiint_{E_F - \Delta E \le E \le E_F} dk_z d^2 k_{||} T(E_z) \frac{\partial E}{\partial k_z}, \tag{5.24}$$

which includes contributions of all electrons with energies between $E_F - \Delta E$ and E_F in Fig. 5.6(b).

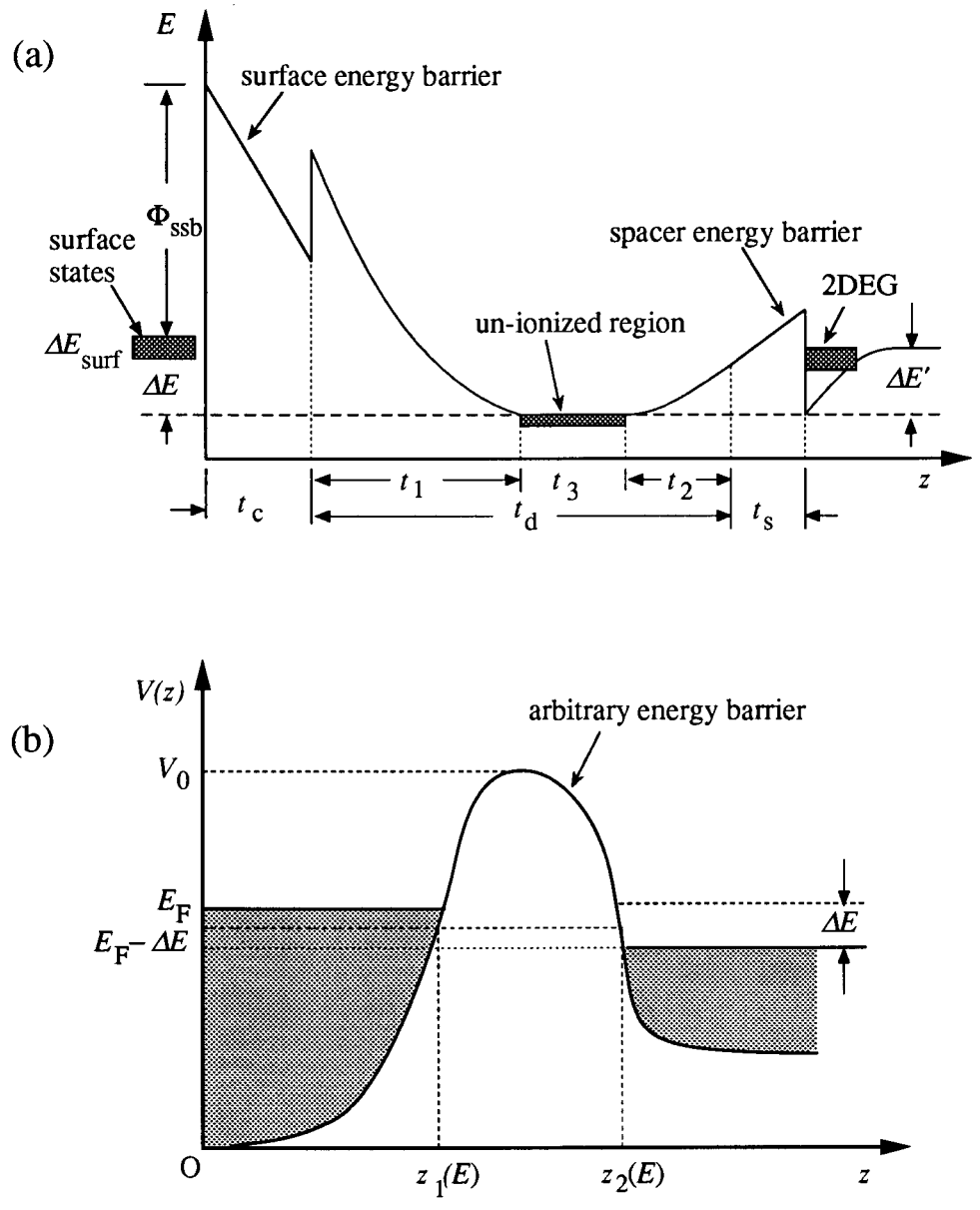

Figure 5.6: (a) A non-equilibrium situation for a quantum wire with the electrons in different regions having different Fermi energies. (b) An arbitrary tunneling energy barrier for calculating the tunneling flux.

The most common approximation for the transmission probability $T(E_z)$ is the semi-classical WKB form

$$T(E_z) = \exp[-2I(E_z)], \tag{5.25}$$

$$I(E_z) = \int_{z_1(E_z)}^{z_2(E_z)} dz \sqrt{\frac{2m(V(z) - E_z)}{\hbar^2}}, \tag{5.26}$$

which depends only on E_z. However, when the Fermi level difference is much smaller than the height of the energy barrier relative to the Fermi level, i.e., $\Delta E \ll V_0 - E_F$, we can use the following approximation

$$T(E_z) \simeq T(E_F) = \exp\left\{-2\int_{z_1(E_F)}^{z_2(E_F)} dz \sqrt{\frac{2m(V(z) - E_F)}{\hbar^2}}\right\}. \tag{5.27}$$

Correspondingly, equation (5.24) becomes

$$J \simeq \frac{2m}{(2\pi)^2\hbar^3} T(E_F) \int_{E_F - \Delta E}^{E_F} E dE = \frac{2m}{(2\pi)^2\hbar^3} T(E_F)(E_F \Delta E - \frac{(\Delta E)^2}{2}), \tag{5.28}$$

where we have used $d^2k_{||} = (\pi m/\hbar^2)dE_{||} = (\pi m/\hbar^2)dE$. From equation (5.28), we can see that the tunneling current depends on the transmission probability $T(E_F)$, the Fermi energy E_F, and the energy difference ΔE between the Fermi energies of the two electron gases.

Now we use equation (5.28) to estimate the tunneling currents in a quantum wire. (Note that the electron mass m in equation (5.28) should be replaced by the effective mass of electron m^*.) The typical parameter values we can use for this estimate are $\Phi_{ssb} = 0.8$ eV, $\Delta E_c = 0.2$ eV, $t_c = 10$ nm, $t_d = 40$ nm, $t_s = 20$ nm, $N_s = 0.5 \times 10^{18}$ cm^{-3}, and $m^* = 0.067m_e$. Approximately, we can use $t_1 \sim 25$ nm and $t_2 \sim 10$ nm, to describe the energy barriers.

In Fig. 5.6(b), the surface electrons have a higher Fermi energy than electrons in the un-ionized region in the doped layer by ΔE. Considering that the surface energy barrier consists of the cap layer and the left side of the ionized doped layer, the transmission probability for the surface energy barrier is estimated to be $T(E_F) \sim 10^{-18}$, which is very small.

For surface electrons, their energy range ΔE_{surf} is very small (typically $\Delta E_{surf} < 0.1$ eV). Therefore, all of the surface electrons can tunnel through the surface energy barrier because the states with the same energies on the other side of the barrier are empty. Thus, $\Delta E = \Delta E_s$. On the other hand, because the Fermi energy here is relative to the lowest energy of surface states, $E_F = \Delta E_{surf}$ effectively. If we use $\Delta E_{surf} = 0.1$ eV, then $J \sim 10^{-10}$ cm^{-2}s^{-1}. Considering that the surface density of electrons is typically $\sigma \sim 10^{12}$ cm^{-2}, the tunneling

flux through the surface energy barrier is negligible. Therefore, we should not consider the surface electrons to be always in equilibrium with the rest in the system.[4]

Similarly, we can estimate the tunneling flux through the spacer energy barrier. For the spacer energy barrier $J \sim 10^{11}\text{cm}^{-2}\text{s}^{-1}$, which is much larger. Considering the area density of the 2DEG is typically $n \sim 10^{11}$ cm^{-2}, the electrons on the two sides of the spacer energy barrier should reach equilibrium in seconds. Therefore, we should treat electrons in the un-ionized region as always being in equilibrium with the 2DEG.

It should be pointed out that the above values of electron flux in quantum wires are *rough estimates* because the surface electrons and the electrons bound to donors in the un-ionized region are both localized. However, these estimates give us a general idea of the scales of the tunneling fluxes of electrons in the quantum wire.

According to above discussion, quantum wires are generally in partial equilibrium. That is, the Fermi energy of the 2DEG is the same as that of the electrons in the un-ionized region (if the un-ionized region is present), but is different from that of the surface electrons.

However, there are two special situations for which we have reasons to consider the whole system as being in absolute equilibrium. One situation is after the sample has just been fabricated and no gate voltage has been applied. This is based on the consideration that the high-temperature (T~500 K) fabrication process provides the conditions necessary for the whole system to reach equilibrium. The other situation is after the quantum wire has just been illuminated, because the electrons excited by illumination have sufficient energy to cross the surface energy barrier, which helps the system to approach equilibrium. In these two situations, the assumption of absolute equilibrium is the starting point for our analytic calculations.

[4] In fact, m^* of a surface electron should be larger than $0.067m_e$ of the GaAs conduction band. Considering that m^* appears in the exponential expression of the transmission probability $D(E_F)$, the tunneling flux should be even smaller.

Chapter 6

Split-Gate Quantum Wires: Calculations

In the first part of this chapter, we set up a general framework for calculating the potential function in the split-gate quantum wire based on the model defined in Chapter 5. Within this framework, we are able to study band bending, the boundary contribution (the consequence of the gate voltage), the effect of illumination, and the confining potential of the quantum wire *quantitatively*. In particular, analytic expressions for the depletion and pinchoff voltages before and after illumination are obtained. In the second part, we take several real split-gate quantum wires as examples for calculating the depletion and pinchoff voltages, and compare the calculated results with experimental measurements. Most of the results presented in this chapter have been published in Ref. [35].

6.1 General Framework

Consider the split-gate quantum wire shown in Fig. 5.1. Because the system is uniform in the y-direction, the potential function is independent of y. Let $\varphi_{\text{total}}(x, z)$ be the total potential function of the system. (The subscript "total" is used to distinguish this potential function from others that will appear later.) Thus the total potential energy of an electron is $-e\varphi_{\text{total}}(x, z)$. Now our objective is to calculate $\varphi_{\text{total}}(x, z)$ within the quantum wire, i.e., in the half space $z > 0$.

Let $\rho_{\text{total}}(x, z)$ be the total charge density in the quantum wire, i.e., for $z > 0$. The

relation between $\varphi_{\text{total}}(x,z)$ and $\rho_{\text{total}}(x,z)$ is described by the Poisson equation

$$\nabla^2\varphi_{\text{total}}(x,z) = -\frac{\rho_{\text{total}}(x,z)}{\varepsilon\varepsilon_0}, \tag{6.1}$$

where ε is the dielectric constant of the quantum wire. Generally speaking, to solve Eq. (6.1) in the half space $z > 0$, we need to know both the total charge density $\rho_{\text{total}}(x,z)$ and the boundary conditions at the $z = 0$ boundary plane.

First, let us consider the boundary conditions of the quantum wire. Because the potential in the metallic gate is uniform, the potential distribution on the interface between the gate and the GaAs cap, i.e., for $|x| \geq w/2$ and $z = 0$, can be regarded as known. However, the potential distribution on the exposed surface, i.e., for $|x| < w/2$ and $z = 0$, is not known. What we know about the exposed surface is that the total number of surface electrons is conserved and the surface states are localized (Feature II). In view of this feature of the boundary conditions, we use the following strategy to solve this problem. We assume that the potential distribution on the exposed surface can be described by some analytic expression which contains some unknown coefficients. Thus the potential distribution on the $z = 0$ plane is completely "known" and the potential function in the half space $z > 0$ can be found by solving Eq. (6.1). Then, using the potential function that is the solution, we determine the unknown coefficients based on the surface properties given in Feature II.

For convenience of calculations, we choose the potential *just inside* the GaAs cap adjacent to the gates to be zero. That is,

$$\varphi_{\text{total}}(x,z)|_{|x|\geq w/2, z=0^+} = 0, \tag{6.2}$$

where $z = 0^+$ means in the GaAs cap and $|x| \geq w/2$ under the gates. Note that the zero value of potential chosen here is different from that we have used in Chapter 5, where the zero potential is chosen at the Fermi energy of the system. (See Fig. 5.4 and Fig. 5.5.) The zero potential condition (6.2) is more suitable for our present calculations because it enables us to discuss the potential function without always involving the interface Schottky barrier. Because of the presence of the interface Schottky barrier Φ_{isb} at the gate-GaAs interface (Feature II), the potential energy of an electron at the Fermi level in the gate is $-\Phi_{\text{isb}}$, according to the zero potential condition (6.2). To express this explicitly,

$$-e\varphi_{\text{total}}(x,z)|_{|x|\geq w/2, z=0^-} = -\Phi_{\text{isb}}, \tag{6.3}$$

where $(|x| \geq w/2, z = 0^-)$ means within the gates.

It is clear that this is an electrostatic problem with the Dirichlet boundary conditions at the $z = 0^+$ plane. Using the Green's function method [189], the solution of Eq. (6.1) for $z > 0$ can be conveniently expressed as

$$\varphi_{\text{total}}(x, z) = \varphi_{\text{c}}(x, z) + \varphi_{\text{b}}(x, z), \tag{6.4}$$

where

$$\varphi_{\text{c}}(x, z) = \frac{1}{4\pi\varepsilon\varepsilon_0} \iiint d^3r' \rho_{\text{total}}(x', z') G(\mathbf{r}, \mathbf{r}'), \tag{6.5}$$

is the contribution from spatial charges and

$$\varphi_{\text{b}}(x, z) = \frac{1}{4\pi} \iint_{(z'=0^+)} dx'dy' \varphi_{\text{total}}(x', z') \frac{\partial}{\partial z'} G(\mathbf{r}, \mathbf{r}'), \tag{6.6}$$

is the contribution from the $z = 0^+$ boundary. Here $\mathbf{r} = (x, y, z)$, $\mathbf{r}' = (x', y', z')$, and $G(\mathbf{r}, \mathbf{r}')$ is the Green's function, which is the solution of

$$\nabla'^2 G(\mathbf{r}, \mathbf{r}') = -4\pi\delta(\mathbf{r} - \mathbf{r}'), \tag{6.7}$$

$$G(\mathbf{r}, \mathbf{r}') \mid_{z'=0^+} = 0. \tag{6.8}$$

Using the image charge method [189], it is easy to find that

$$G(\mathbf{r}, \mathbf{r}') = \frac{1}{[(x'-x)^2 + (y'-y)^2 + (z'-z)^2]^{1/2}} - \frac{1}{[(x'-x)^2 + (y'-y)^2 + (z'+z)^2]^{1/2}}. \tag{6.9}$$

Correspondingly,

$$\frac{\partial G(\mathbf{r}, \mathbf{r}')}{\partial z'} \Big|_{z'=0^+} = \frac{2z}{[(x'-x)^2 + (y'-y)^2 + (z'-z)^2]^{3/2}}, \tag{6.10}$$

which appears in the second term in the expression of $\varphi_{\text{total}}(x, z)$. Because the boundary potential distribution $\varphi_{\text{total}}(x, z = 0^+)$ is "known", the total potential function $\varphi_{\text{total}}(x, z)$ for $z > 0$ can be calculated directly from Eqs. (6.4), (6.5) and (6.6) once we determine $\rho_{\text{total}}(x, z)$.

Here we should point out that the conduction band within the quantum wire has offsets at the two GaAs-$Al_xGa_{1-x}As$ interfaces. (See, for example, Fig. 1.1(b).) In the absence of electrostatic potentials, the bottom of the conduction band within the quantum wire can be expressed as

$$E_{\text{offset}}(z) = \begin{cases} 0, & \text{if } 0 \le z \le t_{\text{c}} \\ \Delta E_{\text{c}}, & \text{if } t_{\text{c}} < z < L \\ 0, & \text{if } z \ge L \end{cases} \tag{6.11}$$

where ΔE_c is the band offset and $L = t_c + t_d + t_s$. This means that the total energy of an electron in the region $t_c < z < L$ is $-e\varphi_{total}(x,z) + \Delta E_c$ effectively, instead of just $-e\varphi_{total}(x,z)$. However, for electrons of the 2DEG at $z = L$, the potential energy is still $-e\varphi_{total}(x,z)$ because the two band offsets at $z = t_c$ and $z = L$ cancel each other.

6.1.1 Spatial Charge Distributions

Before performing detailed calculations, it is useful to make a general analysis of the distributions of spatial charges in the quantum wire.

Generally speaking, the spatial charges consist of the positive charges of the ionized donors in the doped layer and the negative charges of the 2DEG. If the quantum wire is in equilibrium regime B (Fig. 5.4(b)) at zero gate voltage, the distributions of the spatial charges can be of the three different types shown in Fig. 6.1. In the first situation (Fig. 6.1(a)), the shallow donors everywhere in the doped layer ($t_c < z < t_c + t_d$) are ionized and a 2DEG is present everywhere at the $z = L$ interface. This situation occurs when the gate voltage is above the depletion voltage. When the gate voltage is between the depletion voltage and the pinchoff voltage, the 2DEG is depleted from under the gates and is confined to the central region of the quantum wire. This is the second type of the spatial charge distribution (Fig. 6.1(b)). The third situation (Fig. 6.1(c)) occurs when the gate voltage is below the pinchoff voltage, so that the 2DEG is completely depleted from the $z = L$ interface.

If the quantum wire is in equilibrium regime C at zero gate voltage, the spatial charge distribution can be one of the six different types, which are shown in Fig. 6.2. The greater complexity seen here is due to the presence of an un-ionized region in the doped layer. In the first situation (Fig. 6.2(a)), the un-ionized region is infinite, being present for all x. When the gate voltage decreases sufficiently but is above the depletion voltage, the un-ionized region shrinks to the central region in the doped layer while the 2DEG is still present at the whole $z = L$ interface. This corresponds to the second situation (Fig. 6.2(b)). When the gate voltage decreases further, the spatial charge distribution in general can be one of the two possibilities: a finite un-ionized region is present but the 2DEG is confined to the central regions (Fig. 6.2(c1)), or the un-ionized region disappears while the 2DEG is still present at the whole $z = L$ interface (Fig. 6.2(c2)). Which of Fig. 6.2(c1) and Fig. 6.2(c2) occurs depends on the parameters of a particular quantum wire. In the fourth situation (Fig. 6.2(d)), the un-ionized region disappears while a confined 2DEG is present. Finally,

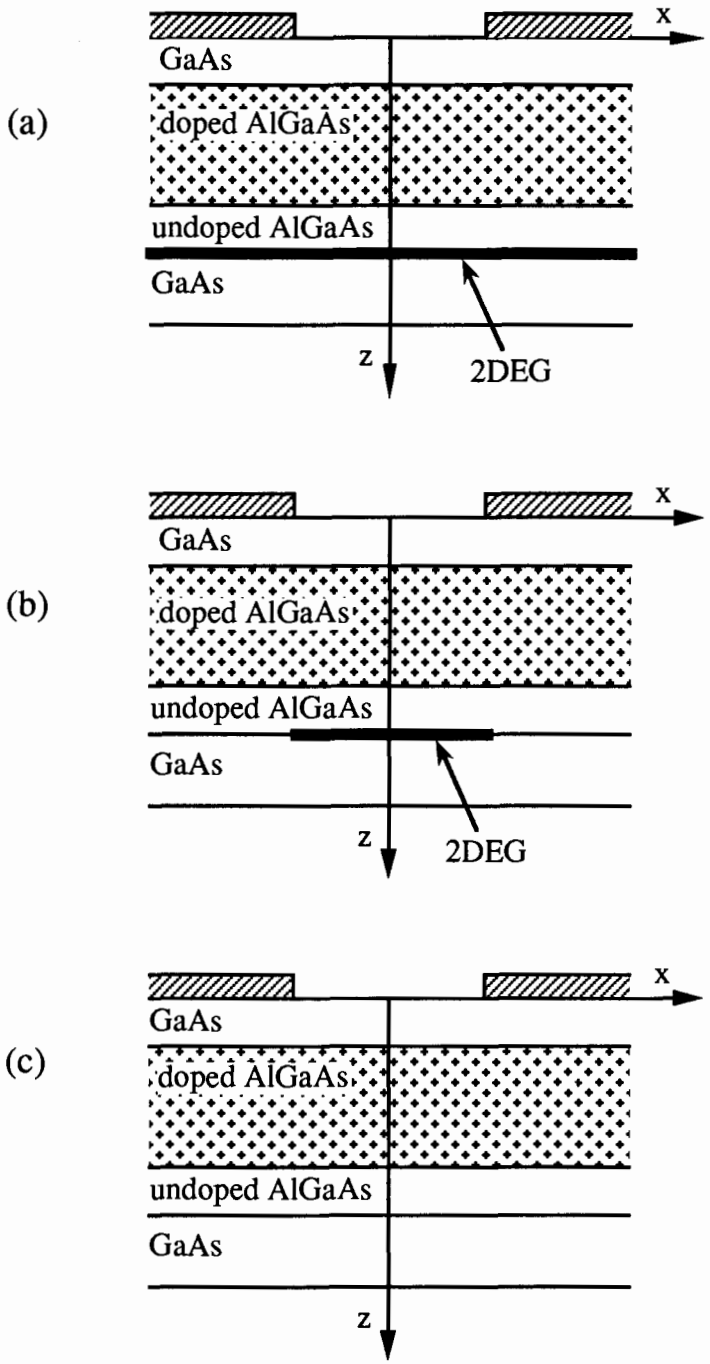

Figure 6.1: A cross-sectional description of the three different types of spatial charge distribution corresponding to equilibrium regime B. (a) The 2DEG is not confined laterally above the depletion voltage. (b) The 2DEG is confined to the wire region between the depletion and pinchoff voltages. (c) The 2DEG is absent below the pinchoff voltage.

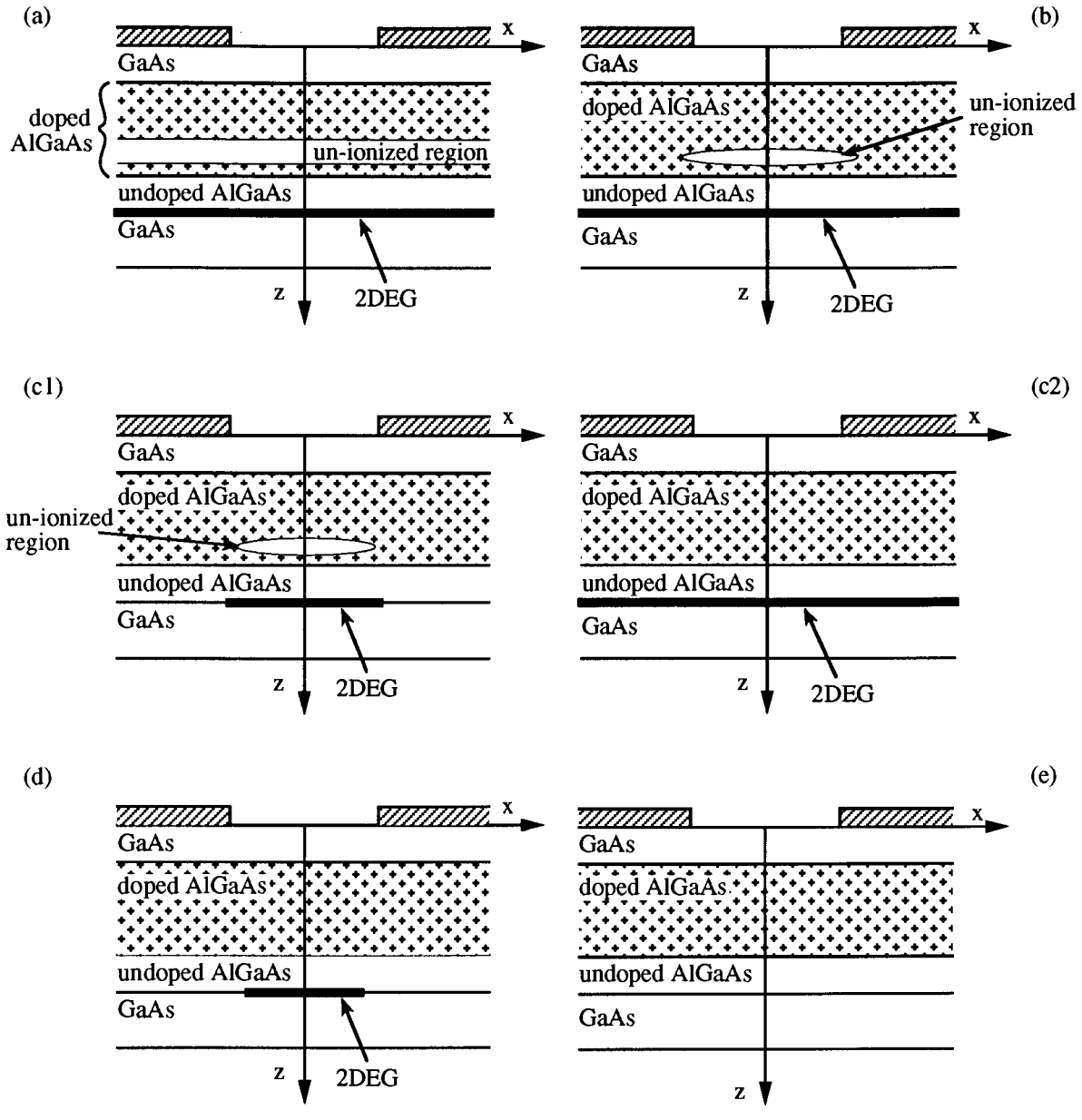

Figure 6.2: A cross-sectional description of the six different types of spatial charge distribution according to equilibrium regime C. (a) An *infinite* un-ionized region and an *infinite* 2DEG. (b) An *finite* un-ionized region and an *infinite* 2DEG. (c1) A *finite* un-ionized region and a *confined* 2DEG. (c2) A *completely* ionized doped layer an *infinite* 2DEG. (d) A *completely* ionized doped layer and a *confined* 2DEG. (e) A *completely* ionized doped layer with an *absent* 2DEG.

when the gate voltage is below the pinchoff voltage, the 2DEG is completely depleted from the $z = L$ interface and the only spatial charges are the positive charges in the whole doped layer, which is the fifth situation (Fig. 6.2(e)).

Here we need to make a remark. In the above analysis of the spatial charge distributions, we have not considered that the equilibrium regimes *under the exposed surface* and *under the gates* at zero gate voltage can be different (see Sec. 5.3.1). This difference can indeed occur because the surface Schottky barrier $\Phi_{\rm ssb}$ and the interface Schottky barrier $\Phi_{\rm isb}$ are not equal in general. If we take this into consideration, there will be more different types of spatial charge distribution. However, the purpose of our analysis of the spatial charge distribution is to provide a general picture for the evolution of spatial charges with the gate voltage. Moreover, for the real quantum wires we will consider later, the values of $\Phi_{\rm ssb}$ and $\Phi_{\rm isb}$ are very close together, and therefore the difference in the equilibrium regimes is not significant.

For convenience of discussion, we split the total charge density into three parts

$$\rho_{\rm total}(x,z) = \rho_1(x,z) + \rho_2(x,z) + \rho_3(x,z), \tag{6.12}$$

where $\rho_1(x,z)$ corresponds to a uniform distribution of positive charges in the *whole* doped layer ($t_{\rm c} < z < t_{\rm c} + t_{\rm d}$), $\rho_2(x,y)$ contains the corresponding negative charges in the un-ionized region (when appropriate to cancel the over-counted amount of the positive charge in $\rho_1(x,z)$), and $\rho_3(x,y)$ corresponds to the the negative charges of the 2DEG. Substituting Eq. (6.12) into Eq. (6.5), we obtain

$$\varphi_{\rm c}(x,z) = \varphi_{\rm c1}(x,z) + \varphi_{\rm c2}(x,z) + \varphi_{\rm c3}(x,z), \tag{6.13}$$

where

$$\varphi_{\rm c1}(x,z) = \frac{1}{4\pi\varepsilon\varepsilon_0}\iiint d^3r'\rho_1(x',z')G(\mathbf{r},\mathbf{r}'), \tag{6.14}$$

$$\varphi_{\rm c2}(x,z) = \frac{1}{4\pi\varepsilon\varepsilon_0}\iiint d^3r'\rho_2(x',z')G(\mathbf{r},\mathbf{r}'), \tag{6.15}$$

$$\varphi_{\rm c3}(x,z) = \frac{1}{4\pi\varepsilon\varepsilon_0}\iiint d^3r'\rho_3(x',z')G(\mathbf{r},\mathbf{r}'), \tag{6.16}$$

where $\varphi_{\rm c1}(x,z)$ descibes the effect of the positive charges in a *wholly* ionized doped layer, $\varphi_{\rm c2}(x,z)$ of the negative charges in the un-ionized region if they are needed to cancel the effect of the over-counted positive charge in $\varphi_{\rm c1}(x,z)$, and $\varphi_{\rm c3}(x,z)$ describes the self-screening effect of the 2DEG.

Correspondingly, the confining potential, which will mean the *external* confining potential, is given by

$$\varphi_{\text{conf}}(x,z) = \varphi_{\text{c1}}(x,z) + \varphi_{\text{c2}}(x,z) + \varphi_{\text{b}}(x,z), \tag{6.17}$$

which does not include $\varphi_{\text{c3}}(x,z)$, the self-screening effect of the 2DEG.

6.1.2 Depletion and Pinchoff Voltages

Because of the presence of the 2DEG and the possible un-ionized region in the doped layer, it is not possible to obtain a general analytic solution for the total potential function. However, it is possible to calculate the depletion voltage and the pinchoff voltage of the quantum wire analytically.

Let us now relate the depletion and pinchoff voltages to the potential function $\varphi_{\text{total}}(x,z)$. Recalling that the gate voltage V_{g} is applied between the gate and the 2DEG (see Fig. 1.3), V_{g} measures the energy difference between the Fermi levels in the gate and in the 2DEG. That is,

$$-eV_{\text{g}} = E_{\text{F}}(\text{gate}) - E_{\text{F}}(\text{2DEG}), \tag{6.18}$$

where $E_{\text{F}}(\text{gate})$ and $E_{\text{F}}(\text{2DEG})$ are the Fermi levels in the gate and the 2DEG, respectively. Note that the applied gate voltage is negative, i.e., $V_{\text{g}} \leq 0$.

At the depletion voltage V_{dep}, electrons of the 2DEG are just depleted from under the gates. In other words, the Fermi level of the 2DEG is almost the same as the energy value of the potential well when $|x| \to \infty$, which is just the bottom of the conduction band of GaAs at $(|x| \to \infty, z = L)$. (See Fig. 6.3.) According to Eq. (6.18), the depletion voltage V_{dep} satisfies

$$-eV_{\text{dep}} = -\Phi_{\text{isb}} + e\varphi_{\text{total}}(|x| \to \infty, z = L), \tag{6.19}$$

where $-\Phi_{\text{isb}}$ and $-e\varphi_{\text{total}}(|x| \to \infty, z = L)$ are equal to the Fermi levels in the gate and of the 2DEG, respectively.

At the depletion voltage, the 2DEG and the un-ionized region (if it occurs) are localized to the central regions of the quantum wire and therefore have no electrostatic effect on a position that is infinitely far away, i.e., $|x| \to \infty$. This is because the Green's function vanishes as $G \sim 1/x^2$. Therefore, in calculating $\varphi_{\text{total}}(|x| \to \infty, z = L)$, the result would not change if we can take $\rho_2(x,z) = 0$ and $\rho_3(x,z) = 0$. This consideration will be used below.

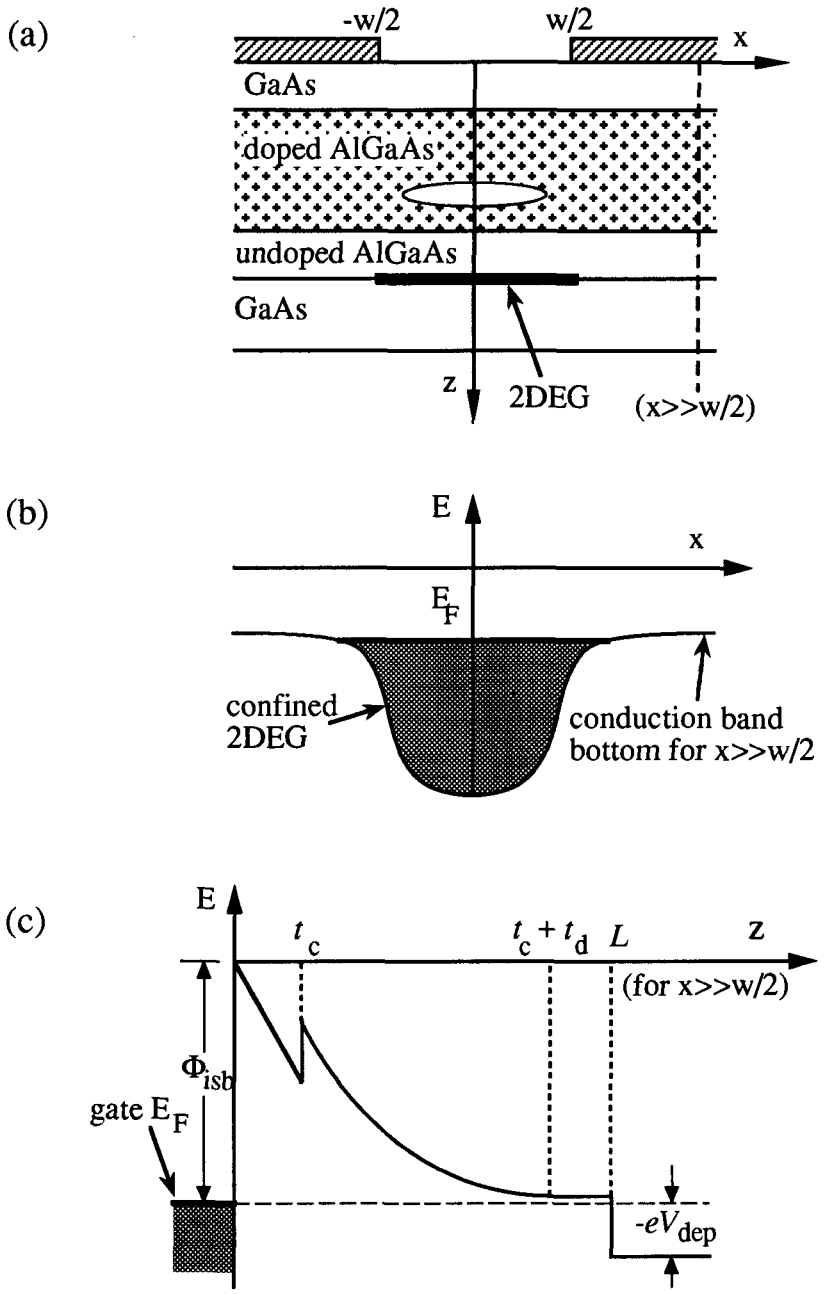

Figure 6.3: The spatial charge distribution and the band structure at the depletion voltage. (a) The cross-sectional view of a possible spatial charge distribution. The 2DEG is confined to the central region and a finite un-ionized region is present in the doped layer. (b) Schematic profile of the $z = L$ potential well that confines electrons. The shaded area shows the confined electrons. (c) The band bending in the z-direction for $|x| \rightarrow \infty$, i.e., along the dashed line shown in (a).

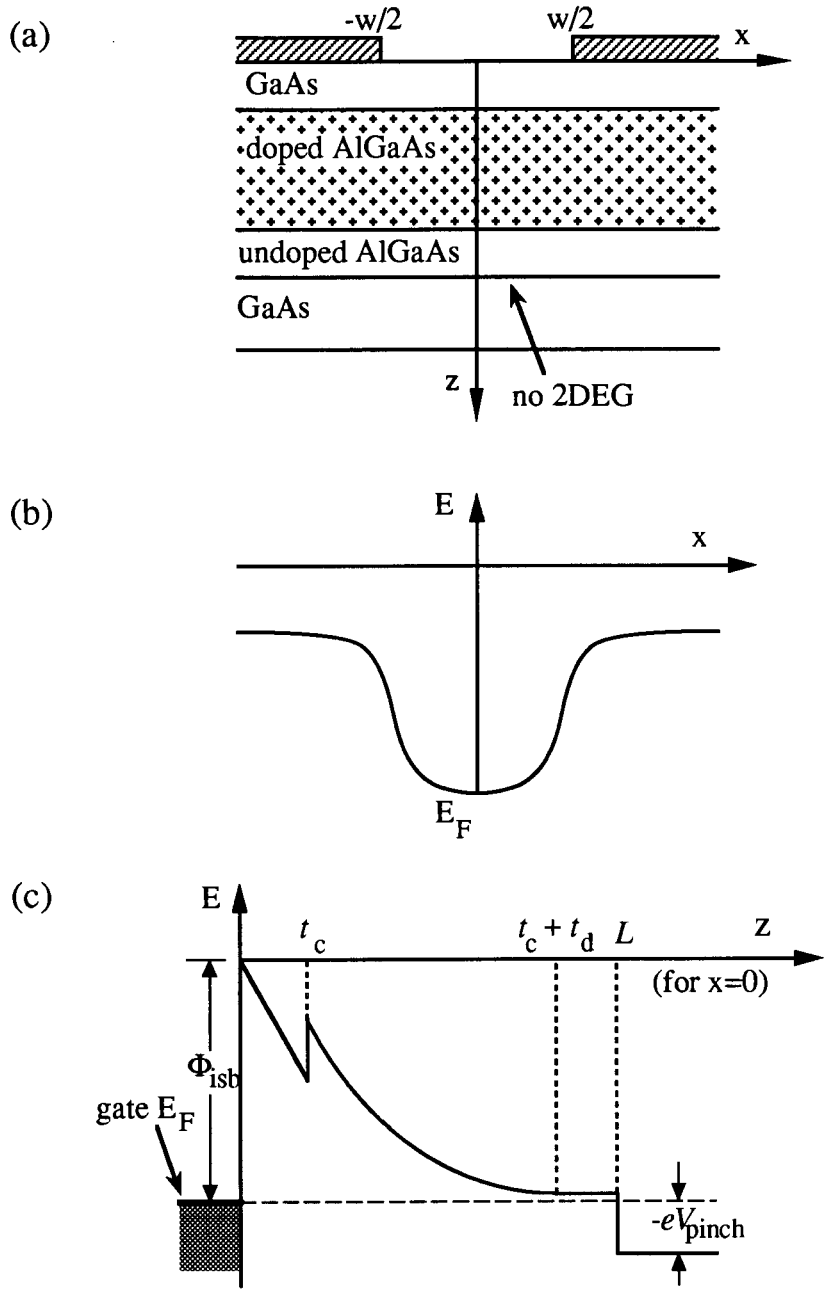

Figure 6.4: The spatial charge distribution and the band structure at the pinchoff voltage. (a) The cross-sectional view of the spatial charge distribution at the pinchoff voltage. The shallow donors are ionized everywhere in the doped layer and no 2DEG is present. (b) The profile of the $z = L$ potential well with no electrons present. (c) The band bending in the z-direction for $x = 0$.

At the pinchoff voltage V_{pinch}, electrons are just completely depleted from the $z = L$ interface. (See Fig. 6.4.) In other words, the Fermi energy of electrons is equal to the lowest energy value of the $z = L$ potential well at the pinchoff voltage. Therefore, the pinchoff voltage measures the energy difference between the Fermi level in the gate and the bottom of conduction band at the point $(x = 0, z = L)$, which has the lowest potential energy at the $z = L$ interface. Thus,

$$-eV_{\text{pinch}} = -\Phi_{\text{isb}} + e\varphi_{\text{total}}(x = 0, z = L), \tag{6.20}$$

where $-e\varphi_{\text{total}}(x = 0, z = L)$ is the potential energy at $(x = 0, z = L)$.

At the pinchoff voltage, because the 2DEG is completely depleted and the shallow donors in doped layer are ionized everywhere, $\rho_2(x, z) = 0$ and $\rho_3(x, z) = 0$. Therefore, $\varphi_{\text{total}}(x = 0, z = L)$ and V_{pinch} can be calculated analytically. See detailed calculations below.

6.1.3 Band Bending

As mentioned above, the conduction band is bent in the z-direction within the quantum wire, which is an important phenomenon. The band bending is mainly caused by spatial charges in the quantum wire. For convenience of discussion, we define the *amount of band bending* due to the spatial charges as

$$E_{\text{bend}}(x) = e\varphi_{\text{c}}(x, z = L). \tag{6.21}$$

Note that the boundary conditions, which are related to the applied gate voltage, also causes some band bending, especially for $|x| \leq w/2$. However, the band bending due to the boundary conditions is combined with the effect of lateral confinement due to the boundary conditions, and it is not convenient to separate these two effects. Therefore, we will consider $\varphi_{\text{b}}(x, z)$ as a whole, which will be studied in detail in the next section. In this section we focus on the band bending due to the *spatial charges.*

When $|x| \to \infty$, because of the boundary condition given by Eq. (6.2) and the relationship $\partial G/\partial z' \sim 1/x^3$ given by Eq. (6.10), $\varphi_{\text{b}}(|x| \to \infty, z)$ vanishes according to Eq. (6.6). Therefore, the difference between the conduction band bottoms at $(|x| \to \infty, z = 0^+)$ and $(|x| \to \infty, z = L)$ is

$$[-e\varphi_{\text{total}}(x, z = 0^+)] - [-e\varphi_{\text{total}}(x, z = L)] = e\varphi_{\text{c}}(x, z = L) = E_{\text{bend}}(x), \tag{6.22}$$

which is completely due to the spatial charges because the boundary effect for $|x| \to \infty$ vanishes.

The amount of band bending $E_{\text{bend}}(x)$ due to the spatial charges (referred to as "band bending" below) is a very useful concept. For example, using Eq. (6.22), the depletion voltage given by Eq. (6.19) becomes

$$-eV_{\text{dep}} = E_{\text{bend}}(|x| \to \infty) - \Phi_{\text{isb}}. \tag{6.23}$$

(Referring to the band structure in Fig. 6.3(c), this equation is obvious.) On the other hand, the pinchoff voltage given by Eq. (6.20) becomes

$$-eV_{\text{pinch}} = E_{\text{bend}}(x = 0) + e\varphi_{\text{b}}(x = 0, z = L) - \Phi_{\text{isb}}, \tag{6.24}$$

where $E_{\text{bend}}(x = 0)$ is the amount of band bending for $x = 0$ and $e\varphi_{\text{b}}(x = 0, z = L)$ is the boundary contribution for $(x = 0, z = L)$ at the pinchoff voltage. Therefore, we need to calculate $E_{\text{bend}}(x = 0)$ at the pinchoff voltage and $E_{\text{bend}}(|x| \to \infty)$ at the depletion voltage for the quantum wire before and after illumination.

Before Illumination

First, let us calculate $E_{\text{bend}}(x = 0)$ at the pinchoff voltage. At the pinchoff voltage, because all the shallow donors in the doped layer are ionized and no 2DEG is present, $\rho_2(x, z) = 0$ and $\rho_3(x, z) = 0$. Therefore, the total charge density $\rho_{\text{total}}(x, z)$ for $z > 0$ is

$$\rho_{\text{total}}(x, z) = \rho_1(x, z) = \begin{cases} 0, & \text{if } 0 < z \le t_{\text{c}} \\ eN_{\text{s}}, & \text{if } t_{\text{c}} < z < t_{\text{c}} + t_{\text{d}} \\ 0, & \text{if } z \ge t_{\text{c}} + t_{\text{d}} \end{cases} \tag{6.25}$$

where N_{s} is the shallow donor density which has been determined in Sec. 5.3.1. Note that the charge density depends only on z. This means that the amount of band bending at the pinchoff voltage before illumination is independent of x.

Substituting Eq. (6.25) into Eq. (6.5) and performing the integral, we obtain

$$\varphi_{\text{c}}(x, z) = \frac{eN_{\text{s}}}{\varepsilon\varepsilon_0} \times \begin{cases} t_{\text{d}} z, & \text{if } 0^+ < z \le t_{\text{c}} \\ -\frac{1}{2}(z - t_{\text{c}} - t_{\text{d}})^2 + t_{\text{c}} t_{\text{d}} + \frac{1}{2} t_{\text{d}}^2, & \text{if } t_{\text{c}} < z < t_{\text{c}} + t_{\text{d}} \\ t_{\text{c}} t_{\text{d}} + \frac{1}{2} t_{\text{d}}^2, & \text{if } z \ge t_{\text{c}} + t_{\text{d}} \end{cases} \tag{6.26}$$

which depends on z only. Note that $\varphi_{\text{total}}(x,z)$ is linear with z in the cap layer, parabolic in the doped layer, and constant in the spacer layer and the 2DEG channel layer. Thus, according to Eq. (6.21), the amount of band bending for $x = 0$ at the pinchoff voltage is

$$E_{\text{bend}}(x=0) = e\varphi_{\text{c}}(x=0, z=L) = E_0, \tag{6.27}$$

where

$$E_0 = \frac{e^2 N_{\text{s}}}{\varepsilon\varepsilon_0}(t_{\text{c}}t_{\text{d}} + \frac{1}{2}t_{\text{d}}^2). \tag{6.28}$$

Note that such a result has been obtained in Chapter 5 directly (see Eq. (5.6)) by considering the positively ionized doped layer and surface electrons as a "capacitor".

At the depletion voltage, both the 2DEG and the possible un-ionized region are localized to the central regions of the quantum wire. Because the finite 2DEG and the un-ionized region have no electrostatic effect at a position that is infinitely far away, i.e., $|x| \to \infty$, we can take $\rho_2(x,z) = \rho_3(x,z) = 0$ when calculating $E_{\text{bend}}(|x| \to \infty)$ at the depletion voltage. Effectively, we have the same spatial charge density as given by Eq. (6.25), and therefore the amount of band bending should be the same. That is,

$$E_{\text{bend}}(|x| \to \infty) = E_0. \tag{6.29}$$

After Illumination

After illumination, the shallow donor density is increased in the *illuminated region* in the doped layer because a percentage of the deep donors in this region are transformed into the shallow donors (Feature I). It is reasonable to assume that the *illuminated region* is the region of the doped layer that is under the exposed surface, i.e., $|x| \leq w/2$. Therefore, the charge density at the pinchoff voltage after illumination becomes

$$\rho'_{\text{c}}(x,z) = \rho'_1(x,z) = \begin{cases} eN'_{\text{s}}, & \text{if } x \leq |w/2| \text{ and } t_{\text{c}} < z < t_{\text{c}} + t_{\text{d}} \\ eN_{\text{s}}, & \text{if } x > |w/2| \text{ and } t_{\text{c}} < z < t_{\text{c}} + t_{\text{d}} \\ 0, & \text{otherwise} \end{cases} \tag{6.30}$$

where N'_{s} is the shallow donor density after the illumination and thus $N'_{\text{s}} > N_{\text{s}}$. Note that N'_{s} should be determined in the same way as N_{s} is, through the measured 2DEG density in the quantum wire after illumination.

In principle, we can perform similar calculations for the amounts of band bending after illumination as we did before illumination. However, because $\rho'_{\text{total}}(x,z)$ is now dependent

on both x and z, the calculation for a general form of $\varphi'_{\text{total}}(x,z)$ after illumination becomes very complicated. Since we only need to know the amount of band bending for $x = 0$, we can calculate $\varphi'_{\text{total}}(x = 0, z)$ directly. Substituting Eq. (6.30) into (6.5) and performing the integral, we obtain

$$\varphi'_{\text{total}}(0,L) \simeq \frac{eN'_{\text{s}}}{\varepsilon\varepsilon_0}(t_{\text{c}}t_{\text{d}} + \frac{1}{2}t_{\text{d}}^2)\left[1 - (\alpha_1 + \alpha_2)\frac{N'_{\text{s}} - N_{\text{s}}}{N'_{\text{s}}}\right], \tag{6.31}$$

where α_1 and α_2 are two factors depending only on the relative ratio L/w

$$\alpha_1 = \frac{2L}{\pi w,} \tag{6.32}$$

$$\alpha_2 = -\frac{8L^3}{\pi w^3}, \tag{6.33}$$

and higher order terms in L/w are neglected. (If we take $L = 70$ nm and $w = 300$ nm for typical split-gate quantum wires, then $\alpha_1 = 0.15$ and $\alpha_2 = -0.03$, which are much less than 1. The higher order terms about L/w are even smaller and therefore it is sufficient to keep only α_1 and α_2.) Therefore, the total amount of band bending for $x = 0$ at the pinchoff voltage after illumination is

$$E'_{\text{bend}}(x = 0) = E'_0\left[1 - (\alpha_1 + \alpha_2)\frac{N'_{\text{s}} - N_{\text{s}}}{N'_{\text{s}}}\right], \tag{6.34}$$

where

$$E'_0 = \frac{e^2N'_{\text{s}}}{\varepsilon\varepsilon_0}(t_{\text{c}}t_{\text{d}} + \frac{1}{2}t_{\text{d}}^2). \tag{6.35}$$

Since the shallow donor density in region of the doped layer *under the gates*, i.e., for $|x| > w/2$, has not been changed by illumination, the amount of the band bending $E'_{\text{bend}}(|x| \to \infty)$ at the depletion voltage after illumination remains unchanged. That is,

$$E'_{\text{bend}}(|x| \to \infty) = E_0 \tag{6.36}$$

We have now calculated the amounts of band bending for $x = 0$ at the pinchoff voltage and for $|x| = \infty$ at the depletion voltage both before and after illumination. The results are summarized in Table 6.1.

6.1.4 Boundary Contribution

The potential function due to the boundary contribution, i.e., $\varphi_{\text{b}}(x,z)$, provides the potential well at $z = L$ that confines the 2DEG laterally. To see that, consider the total potential

Table 6.1: The amounts of band bending for $|x| \to \infty$ at the depletion voltage and for $x = 0$ at the pinchoff voltage before and after illumination.

	before illumination	after illumination
for $\|x\| \to \infty$ at V_{dep}	E_0	E_0
for $x = 0$ at V_{pinch}	E_0	$E_0'[1-(\alpha_1+\alpha_2)(N_s'-N_s)/N_s']$

distribution within the quantum wire at the pinchoff voltage before illumination. The potential due to spatial charges, which is given by Eq. (6.26) is independent of x. Therefore, the lateral confinement for electrons at $z = L$ must come from the boundary contribution.

To calculate the boundary contribution $\varphi_b(x,z)$, we need to determine the potential distribution on the exposed surface ($|x| < w/2$, $z = 0^+$). Considering the symmetry of the quantum wire, the potential function should be even in x. Thus the potential function at the exposed surface can be generally expressed as

$$\varphi_{\text{total}}(x, z = 0^+) = \sum_{k=0}^{\infty} a_k x^{2k}, \quad |x| < w/2, \tag{6.37}$$

where $\{a_k\}$ are a series of constant coefficients. In calculations, we need to keep at least two terms in expansion (6.37) so that the surface potential can be kept continuous at $x = \pm w/2$. If we keep the first two terms in Eq. (6.37) and remember that the potential immediate under the gates has been chosen to be zero, this yields

$$\varphi_{\text{total}}(x, z = 0^+) = \begin{cases} V_0(1 - 4x^2/w^2), & \text{if } |x| < w/2 \\ 0, & \text{if } |x| \geq w/2 \end{cases} \tag{6.38}$$

where V_0 is a voltage constant and will be determined later using surface properties.

Substituting Eq. (6.38) into equation (6.6) and performing the integral, the boundary contribution is

$$\varphi_b(x,z) = \frac{4V_0}{\pi w^2}\left[(\frac{w^2}{4} + z^2 - x^2)\theta(x,z) + xz\ln\frac{(w+2x)^2+4z^2}{(w-2x)^2+4z^2} - wz\right], \tag{6.39}$$

where

$$\theta(x,z) = \arctan\frac{w-2x}{2z} + \arctan\frac{w+2x}{2z}, \tag{6.40}$$

is just the angle that is subtended by the exposed surface at the point (x,z). It is easy to verify that, when $z = 0^+$, Eq. (6.39) reduces to the expression (6.38).

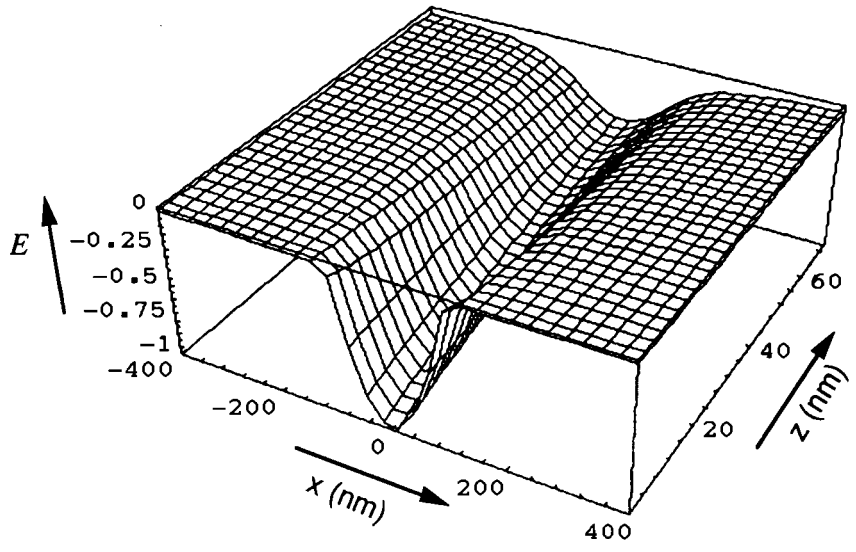

Figure 6.5: A Three-dimensional representation of the potential energy $-e\varphi_b(x,z)$ due to the boundary contribution for $z > 0^+$. Used parameters are $w = 100$ nm and $eV_0 = 1$ (arbitrary unit).

To visualize the effect of the boundary contribution, we present a three-dimensional plot of the potential energy $-e\varphi_{\rm b}(x,z)$ in Fig. 6.5. For a fixed z, we can see the profile of $-e\varphi_{\rm b}(x,z)$ along the x direction. Note that the larger L is, the more shallow the confining potential well becomes.

In particular, we are interested in the central point $(x = 0, z = L)$ and the boundary contribution at this point is

$$\varphi_{\rm b}(0,L) = \frac{2V_0}{\pi}[(1+\frac{4L^2}{w^2})\arctan\frac{w}{2L} - \frac{2L}{w}]. \tag{6.41}$$

This result can be written as

$$\varphi_{\rm b}(0,L) = V_0 g(L/w), \tag{6.42}$$

where

$$g(L/w) = \frac{2}{\pi}[(1+\frac{4L^2}{w^2})\arctan\frac{w}{2L} - \frac{2L}{w}] \tag{6.43}$$

is a geometrical factor which depends only on the ratio L/w.

With both $\varphi_{\rm c}(x,z)$ and $\varphi_{\rm b}(x,z)$ known at the pinchoff voltage, it is possible to calculate the electron distribution $\sigma(x)$ on the exposed surface $(|x| < w/2, z = 0)$ at the pinchoff voltage. For this purpose, we write total potential function for $|x| < w/2$ in the whole space

as,

$$\varphi_{\text{total}}(x,z) = \begin{cases} \varphi_{\text{c}}(x,z) + \varphi_{\text{b}}(x,z), & \text{if } z > 0, \\ \varphi_{\text{b}}(x,-z), & \text{if } z < 0, \end{cases} \tag{6.44}$$

where the expression for $z < 0$ is based on the consideration that the $z < 0$ half space (outside of the quantum wire) has the same boundary condition as Eq. (6.38) but has no spatial charges. Therefore, the surface electron density $\sigma(x)$ at the exposed surface ($|x| < w/2, z = 0$) can be calculated through

$$\begin{aligned} -\frac{e\sigma(x)}{\varepsilon\varepsilon_0} &= -\frac{\partial}{\partial z}\varphi_{\text{total}}(x,z)|_{z=0+} + \frac{\partial}{\partial z}\varphi_{\text{total}}(x,z)|_{z=0-} \\ &= -2\frac{\partial}{\partial z}\varphi_{\text{b}}(x,z)|_{z=0+} - \frac{\partial}{\partial z}\varphi_{\text{c}}(x,z)|_{z=0+}, \end{aligned} \tag{6.45}$$

where we have used Eq. (6.44). Substituting $\varphi_{\text{c}}(x,z)$ in Eq. (6.26) and $\varphi_{\text{b}}(x,z)$ in Eq. (6.39) into Eq. (6.45), we obtain

$$-e\sigma(x) = -eN_{\text{s}}t_{\text{d}} + \frac{8\varepsilon\varepsilon_0 V_0}{\pi w^2}[x \ln \frac{(w+2x)^2}{(w-2x)^2} - w], \tag{6.46}$$

where the first and the second terms are due to $\varphi_{\text{c}}(x,z)$ and and $\varphi_{\text{b}}(x,z)$, respectively.

Now the voltage constant V_0 can be determined by the conservation of the total number of surface electrons (Feature II). In other words, the linear electron density on the exposed surface is independent of the gate voltage. Therefore,

$$\int_{-w/2}^{w/2} \sigma(x)dx = w\sigma_0 = wN_{\text{s}}t_1, \tag{6.47}$$

where $\sigma_0 = N_{\text{s}}t_1$ is the area density of surface electron at zero gate voltage, which have been calculated in Sec. 5.3.1. Substituting Eq. (6.46) into (6.47) and performing the integral, we obtain

$$V_0 = \frac{\pi e w N_{\text{s}}}{8\varepsilon\varepsilon_0}(t_{\text{d}} - t_1). \tag{6.48}$$

Note that t_1 should be determined from the calculation procedures described in Sec. 5.3.1.

Note that for situations after illumination, N_{s} in above equations should be replaced with N_{s}', which is the shallow donor density after illumination.

Here it is appropriate to comment on the earlier work of Davies [144] who was the first to study the boundary contribution to the potential of a quantum wire using the Green's function method. Davies considered only the leading term in the expansion (6.37) of the surface potential. However, this approximation is not adequate since it yields a discontinuous

potential along the surface at $x = \pm w/2$. As a consequence, the integral of the surface electron density diverges. By retaining also the second term of the expansion (6.37), we obtain a continuous surface potential and a finite integrated surface electron density. This enables us to use the conservation of the the surface electron at the exposed surface to evaluate V_0.

6.1.5 Summary

We now summarize the main results we have obtained in this chapter.

Using the Green's function method, the total potential function within the quantum wire can be generally expressed as the sum of the contribution of spatial charges and the boundary contribution

$$\varphi_{\text{total}}(x,z) = \varphi_{\text{c}}(x,z) + \varphi_{\text{b}}(x,z), \tag{6.49}$$

where

$$\varphi_{\text{c}}(x,z) = \frac{1}{4\pi\varepsilon\varepsilon_0}\iiint d^3r'\rho_{\text{total}}(x',z')G(\mathbf{r},\mathbf{r}'), \tag{6.50}$$

$$\varphi_{\text{b}}(x,z) = \frac{1}{4\pi}\iint_{(z'=0^+)} dx'dy'\varphi_{\text{total}}(x',z')\frac{\partial}{\partial z'}G(\mathbf{r},\mathbf{r}'). \tag{6.51}$$

For convenience, the contribution of the spatial charges can be split into three parts

$$\varphi_{\text{c}}(x,z) = \varphi_{\text{c1}}(x,z) + \varphi_{\text{c2}}(x,z) + \varphi_{\text{c3}}(x,z), \tag{6.52}$$

with $\varphi_{\text{c1}}(x,z) + \varphi_{\text{c2}}(x,z)$ and $\varphi_{\text{c3}}(x,z)$ corresponding to the total positive charge in the doped layer and the negative charge of the 2DEG, respectively. The external confining potential can therefore be written as

$$\varphi_{\text{conf}}(x,z) = \varphi_{\text{c1}}(x,z) + \varphi_{\text{c2}}(x,z) + \varphi_{\text{b}}(x,z). \tag{6.53}$$

The external confining potential is provided mainly by the boundary contribution, which is

$$\varphi_{\text{b}}(x,z) = \frac{4V_0}{\pi w^2}\left[(\frac{w^2}{4} + z^2 - x^2)\theta(x,z) + xz\ln\frac{(w+2x)^2+4z^2}{(w-2x)^2+4z^2} - wz\right], \tag{6.54}$$

where

$$\theta(x,z) = \arctan\frac{w-2x}{2z} + \arctan\frac{w+2x}{2z}, \tag{6.55}$$

if we use a parabolic potential on the exposed surface. The spatial charges in the doped layer affect the confining potential when an un-ionized region is present, or after the quantum

wire has been illuminated. At the pinchoff voltage before illumination, the x-dependence of the total potential is given by $\varphi_b(x,z)$.

The depletion voltage and the pinchoff voltage can be calculated analytically using the known parameters of the quantum wires. From Eqs. (6.23), (6.29), and (6.36), the depletion voltages of a split-gate quantum wire before and after illumination are given by

$$-eV_{dep} = E_0 - \Phi_{isb} \tag{6.56}$$

where

$$E_0 = \frac{e^2 N_s}{\varepsilon\varepsilon_0}(t_c t_d + \frac{1}{2}t_d^2). \tag{6.57}$$

The depletion voltage is not affected by illumination.

From Eqs. (6.24), (6.28), and (6.41), the pinchoff voltage before illumination is

$$-eV_{pinch} = E_0 + e\varphi_b(x=0, z=L) - \Phi_{isb}, \tag{6.58}$$

where

$$e\varphi_b(0,L) = \frac{2eV_0}{\pi}[(1+\frac{4L^2}{w^2})\arctan\frac{w}{2L} - \frac{2L}{w}]. \tag{6.59}$$

From Eqs. (6.24), (6.34), and (6.41), the pinchoff voltage after illumination is

$$-eV_{pinch} = E_0'\left[1-(\alpha_1+\alpha_2)\frac{N_s'-N_s}{N_s'}\right] + e\varphi_b'(x=0,z=L) - \Phi_{isb}, \tag{6.60}$$

where

$$E_0' = \frac{e^2 N_s'}{\varepsilon\varepsilon_0}(t_c t_d + \frac{1}{2}t_d^2), \tag{6.61}$$

and

$$e\varphi_b'(0,L) = \frac{2eV_0'}{\pi}[(1+\frac{4L^2}{w^2})\arctan\frac{w}{2L} - \frac{2L}{w}]. \tag{6.62}$$

where V_0' is the voltage constant after illumination.

6.2 Calculations for Real Samples

We will take four real split-gate quantum wires as examples for calculating the depletion and pinchoff voltages before and after illumination. Here the crucial thing is to determine the shallow donor densities N_s before illumination and N_s' after illumination. According to the discussion in Sec. 5.3.1, N_s and N_s' can be calculated from the corresponding values of n_0, the 2DEG densities at zero gate voltage, if the n_0 values are known from measurements.

Such calculations will be made for sample I. However, for many samples n_0 after illumination is not known. In this case, we use the total donor density N_{total} for N_s', which corresponds to the case of saturated illumination. Such calculations are made for samples II, III and IV.

6.2.1 Sample I

The depletion voltage and the pinchoff voltage of a quantum wire before or after illumination can be calculated analytically if the corresponding 2DEG densities n_0 at zero gate voltage are measured. Such calculations follow the following procedure:

1. Calculate the critical density n_β as described in Sec. 5.3.1.
2. Identify the equilibrium regime at zero gate voltage by comparing the measured n_0 to n_β according to Table 5.2.
3. Determine the shallow donor density N_s (before illumination) or N_s' (after illumination) using the measured n_0 as described in Sec. 5.3.1.
4. Calculate the depletion voltage from Eq. (6.56).
5. Calculate the pinchoff voltage before illumination from Eq. (6.58) and the pinchoff voltage after illumination from Eq. (6.60). (This step involves determining the voltage constant V_0 using the conservation of the total number of surface electrons.)

Sample I is a split-gate quantum wire fabricated and measured by Dr. Sachrajda and collaborators at the Institute of Microstructural Sciences at NRC. This sample is grown by MBE on a semi-insulating GaAs substrate, and its layers in sequence are a 65 nm GaAs buffer, 30 periods of GaAs/AlAs superlattice, 900 nm GaAs channel layer, 1.5 nm AlAs and 16 nm undoped $Al_{0.33}Ga_{0.67}As$ layers as the spacer, 40 nm Si-doped $Al_{0.33}Ga_{0.67}As$ layer with the donor density of 1.1×10^{18} cm^{-3}, and an 18 nm GaAs cap layer with normal surface (100). On top of the GaAs cap, two separate gate bars of titanium are applied using electron beam lithography. The gate bars have a spatial separation of 200 nm and a width of 200 nm.

Analysis after growth shows that the thickness of the undoped $Al_{0.33}Ga_{0.67}As$ layer is 14.5 nm instead of the expected value of 16 nm. This suggests that all of the actual thicknesses should be reduced by 10% from their expected values. Correspondingly, the concentration of the Si donors in the doped $Al_{0.33}Ga_{0.67}As$ layer should be increased by

Table 6.2: The sample parameters and relevant energy parameters used in the calculations for sample I.

Type	Description	Notation	Value	Unit
geometrical	GaAs cap layer	t_c	16.2	nm
	doped $Al_{0.33}Ga_{0.67}As$ layer	t_d	36	nm
	total spacer layer	t_s	15.75	nm
	gate separation	w	200	nm
energies	surface Schottky barrier	Φ_{ssb}	0.80	eV
	interface Schottky barrier	Φ_{isb}	0.83	eV
	conduction band offset	ΔE_c	0.20	eV
	z-direction energy spacing	ΔE_z	0.04	eV
others	effective mass of electron	m^*	0.067	m_e
	dielectric constant	ε	12.5	

10% so as to preserve the nominal total number of donors. The sample parameters based on fabrication information are listed in Table 6.2.

The values of the relevant energy parameters are chosen as follows: Based on the surface properties of GaAs(100) (Feature I), the surface Schottky barrier is taken as $\Phi_{ssb} = 0.80$ eV. According to Table 5.1 in Chapter 5, the interface Schottky barrier between titanium (the gate metal of sample I) and GaAs is $\Phi_{isb} = 0.83$ eV. The offset of the conduction band at the GaAs-$Al_xGa_{1-x}As$ interface is taken as $\Delta E_c = 0.20$ eV. Finally, according to our discussion in Chapter 1, the energy level spacing due to the z-direction confinement is typically $\Delta E_z = 0.04$ eV. Other parameters used are $m^* = 0.067$ and $\varepsilon = 12.5$. These parameters are also listed in Table 6.2.

The measured resistance curves for sample I are displayed in Fig. 1.4 in Chapter 1. The three resistance curves correspond to the three conditions of sample I: before illumination, after a short illumination, and after a long illumination. By inspection of Fig. 1.4, the depletion voltages for curves A, B, and C are -0.33 V, -0.35 V and -0.37 V, respectively, and the pinchoff voltages for curves A, B, and C are -0.55 V, -0.86 V, and -1.33 V, respectively. Corresponding to these three conditions, the measured 2DEG densities n_0 at zero gate voltage are 3.40×10^{11} cm^{-2}, 5.49×10^{11} cm^{-2}, and 6.25×10^{11} cm^{-2}, respectively.

Based on the parameters listed in Table 6.2, the calculated critical values that separate the equilibrium regimes of sample I are $N_\alpha = 0.45 \times 10^{18}$ cm^{-3}, $N_\beta = 0.80 \times 10^{18}$ cm^{-3}, and $n_\beta = 6.03 \times 10^{11}$ cm^{-2}. Referring to the criteria displayed in Table 5.2 in Chapter 5, the

Table 6.3: The equilibrium regimes and calculated results for sample I.

Parameter	Notation	Before ill.	Short ill.	Long ill.	Unit
equilibrium regime		B	B	C	
shallow donor density	N_s	0.65	0.77	1.02	10^{18} cm^{-3}
	t_1	30.79	28.87	24.03	nm
	t_2	5.21	7.13	6.11	nm
	t_3	0	0	5.86	nm
depletion voltage	V_{dep}	−0.34	−0.34	−0.34	V
pinchoff voltage	V_{pinch}	−0.53	−0.80	−1.43	V

Table 6.4: A comparison between the calculated and experimental results for the depletion and pinchoff voltages.

Parameter	Before ill.	Short ill.	Long ill.	Unit
experimental V_{dep}	−0.33	−0.35	−0.37	V
calculated V_{dep}	−0.34	−0.34	−0.34	V
experimental V_{pinch}	−0.55	−0.86	−1.33	V
calculated V_{pinch}	−0.53	−0.80	−1.43	V

equilibrium regimes of sample I are B, B, and C for the conditions before illumination, after a short illumination, and after a long illumination, respectively.

Following the procedure described at the beginning of this section, we made calculations for the conditions of sample I before illumination, after a short illumination, and after a long illumination, respectively. The calculated results are displayed in Table 6.3.

In Table 6.4, we compare the calculated and experimental results for the depletion and pinchoff voltages for the three conditions: before illumination, after a short illumination, and after a long illumination. The calculated and the experimental results are in good agreement. Note that the decrease of the experimental depletion voltage upon illumination can be explained by the fact that the gate bars are very narrow (see Fig. 1.3 in Chapter 1) and therefore some illuminating photons may penetrate into the regions under the gates and excite the deep donors there.

6.2.2 Other Samples

For some split-gate quantum wires, although their depletion and pinchoff voltages were determined from conductance measurements, the corresponding 2DEG densities n_0 were not measured. (Usually the 2DEG density n_0 *before illumination* is measured but the depletion and pinchoff voltages are measured *after illumination.*) In this case, we can not use the above calculation procedures because the information about n_0 is missing.

Experimentally, one is particularly interested in the pinchoff voltage of a quantum wire after illumination, because the pinchoff voltage before illumination is too low for the wire to display many conductance plateaus. Therefore, quantum wires are often illuminated sufficiently to bring the wires very close to the saturation condition of illumination, i.e., $N_s' \approx N_{\text{total}}$. On the other hand, considering that illumination has a very small effect on the depletion voltage (because the wires are short), we can use the measured depletion voltage to determine the shallow donor density N_s before illumination. Thus, it is possible to calculate the pinchoff voltage for the saturation condition of illumination without using any information on n_0. This approach is useful for many samples and the calculation procedures are:

1. Calculate the critical densities N_α and N_β as described in Sec. 5.3.1.
2. Calculate N_s using the measured depletion voltage from Eq. (6.56).
3. Take $N_s' = N_{\text{total}}$, where N_{total} is known from fabrication.
4. Identify the equilibrium regime at zero gate voltage.
5. Calculate the pinchoff voltage before illumination from Eq. (6.58) and after illumination from Eq. (6.60).

Note that the pinchoff voltage calculated through the above procedure corresponds to the saturated condition of illumination.

We take three samples as examples for such calculations. Samples II and III are the single split-gate quantum wires that were used by van Wees *et al.* [18] and Wharam *et al.* [19], respectively, in the first studies of conductance quantization. Sample IV is a system of the two parallel quantum wires used by Smith *et al.* [20] in studying the correlations between parallel quantum wires. (The conductance curves measured by Smith *et al.* [20] are shown in Fig. 1.6 in Chapter 1. However, for our present purpose, we only need to concentrate

Table 6.5: Parameters for samples II, III and IV that are used in the calculations.

Description	Notation	Sample II	Sample III	Sample IV	Unit
GaAs cap layer	t_c	20	10	10	nm
doped $Al_xGa_{1-x}As$ layer	t_d	40	40	40	nm
spacer layer	t_s	20	20	20	nm
gate separation	w	250	500	300	nm
wire separation	w_s	N/A	N/A	200	nm
total donor density	N_{total}	1.33	1.0	1.0	10^{18} cm^{-3}
measured depletion voltage	V_{dep}	-0.6	-0.5	-0.5	eV

on curve A, which is the first measurement after sample fabrication.) In our theory, the calculations for two quantum wires can be done similarly to that for a single quantum wire, by appropriately changing the total charge density and the boundary conditions.

The parameters for samples II, III, and IV are listed in Table 6.5. (Some of the parameters for samples III and IV that were not mentioned in the original papers [19, 20] were kindly provided to us by Dr. Ford.) Note that, for sample III, the widths of the exposed surfaces of the two quantum wires are the same $w_1 = w_2 = w$. The relevant energy parameters used in the calculations for these three samples were the same as those listed in Table 6.2.

The critical densities for sample II are $N_\alpha = 0.34\times10^{18}$ cm^{-3} and $N_\beta = 0.59\times10^{18}$ cm^{-3}. The critical densities for samples III and IV are the same: $N_\alpha = 0.46 \times 10^{18}$ cm^{-3} and $N_\beta = 0.76 \times 10^{18}$ cm^{-3}, because they have the same layer thicknesses. For the saturated illumination, $N_{total} > N_\beta$ for all samples and therefore they are all in equilibrium regime C.

The calculated results for the three samples are shown in Table 6.6. Note that, since samples III and IV have the same values of t_c, t_d, t_s, and N_{total}, the corresponding values of t_1, t_2, and t_3 (at zero gate voltage) are equal as well. However, the calculated pinchoff voltages are different because samples III and IV have different gate separations. The significant difference between the calculated pinchoff voltages of samples III and IV implies that the gate separation is an important factor in determining the value of the pinchoff voltage.

The calculated pinchoff voltage for sample III is very close to the measured result. We interprete this to mean that the measurement was carried out close to the condition of saturated illumination. On the other hand, the large difference between the calculated and

Table 6.6: The equilibrium regimes and calculated results for samples II, III and IV.

Parameter	Notation	Sample II	Sample III	Sample IV	Unit
equilibrium regime		C	C	C	
	t_1	18.0	28.5	28.5	nm
	t_2	4.0	4.9	4.9	nm
	t_3	18.0	6.6	4.9	nm
calculated pinchoff voltage	V_{pinch}	-3.6	-3.3	-1.7	V
measured pinchoff voltage	V_{pinch}	-2.2	-3.4	-1.5	V

measured V_{pinch} for sample II suggests that this measurement was carried out quite far away from the condition of saturated illumination.

Finally, it should be pointed out that the sample parameters used in our calculations above should have some uncertainties. Due to the details of fabrication process, the real layer thicknesses of a sample are usually different from their expected values, typically by 10%. (Such a difference has been corrected in our calculations for sample I.) The values of Φ_{ssb}, Φ_{isb} and ΔE_{c} used in the above calculations can also induce some errors. In obtaining the analytic expressions, we have made several approximations such as using a parabolic potential for the exposed surface and assuming that effects of illumination are confined to the illuminated region. Moreover, all of the above samples are short quantum wires, while the analytic expressions used in the calculations are for ideal quantum wires that are infinitely long. Considering these factors, the above calculated results are in very satisfactory agreement with experiment. This also means that our electrostatic model works quite well for realistic split-gate quantum wires.

Chapter 7

General Remarks

7.1 Thesis Summary

This thesis has presented both numerical studies of the electronic structure of Coulomb-confined quantum wires, and analytic studies of the electrostatic potentials in realistic split-gate quantum wires. A summary with general comments on the whole thesis is given below.

1. *The model of Coulomb-confined quantum wires.* This model was proposed as an idealization of realistic quantum wires for the purpose of numerical calculations. It reflects the essential physical structure of realistic quantum wires, and represents the net effect of many realistic factors. Within its simple picture, it becomes possible to study numerically some complicated properties of quantum wires, such as the many-body effects.

   The model of Coulomb-confined quantum wires can be improved to describe realistic quantum wires in a more accurate way. (See below in the next section.) In fact, this model is very flexible and can be applied to quantum wires fabricated with various confinement techniques, such as selective etching, gating, ion implantation, and selective epitaxy. (On the other hand, the more conventional direct numerical approach to solve the Schrödinger and Poisson equations with boundary conditions is not suitable for quantum wires fabricated by selective etching, ion implantation, and selective epitaxy, because the non-planar boundaries and complicated spatial charges make the calculations impossible.) Therefore, the Coulomb-confined model has many potential applications.

2. *Many-body effects.* Within the Coulomb-confined model, we have calculated self-consistently the electronic structures of quantum wires using the density functional theory and the Hartree approximation. The numerical results show that the many-body effects are important in the Coulomb-confined quantum wires, and that the exchange and correlation energies should be included in the calculations in order to obtain qualitatively accurate results. Our calculations provide new evidence that many-body effects tend to be stronger in low-dimensional systems.

3. *Bound states.* We have proved that, for any Coulomb-confined quantum wire, all populated states are bound. Our density functional calculations show that, at low linear electron densities and small separations between the donor ribbon and the electron plane, all of the electrons populate tightly bound states. However, at high densities and/or large separations, some weakly bound transverse energy levels can be populated by electrons. The numerical results of our present approach are not reliable when some weakly bound states are populated. Therefore, studies involving populated weakly bound states require a different approach.

4. *Energy level locking.* Using the Coulomb-confined model and the density functional theory, we have studied numerically the electronic correlations between two parallel quantum wires. The calculated electronic structure shows that transverse energy levels lock together in pairs when the two wires have similar widths and their separation is not too small. The energy level locking is associated with a charge imbalance and strong Coulomb interactions between the quantum wires. The charge imbalance is particularly significant when the Fermi level crosses a transverse energy level, because of the density of states singularities that are characteristic of one-dimensional fermionic systems. The energy level locking in similar parallel quantum wires has been predicted to be a quite long-range effect. However, this effect is much less likely to occur in dissimilar parallel wires because of the different electronic structure of such systems.

   Energy level locking is a novel phenomenon and is the opposite of the usual energy level anti-crossings that open energy gaps in quantum mechanical systems.

   The energy level locking effect can be used to explain the double conductance steps observed in a pair of parallel quantum wires. Some experimental methods have been suggested for further detecting this effect in pairs of parallel quantum wires.

5. *The model of split-gate quantum wires.* We have established a new electrostatic model of split-gate quantum wires. It incorporates the crucial properties of donors, surfaces and interfaces, and considerations of system equilibrium that apply in different situations. Explanations and arguments have been provided in support of the features of the model.

6. *Analytic calculations for split-gate quantum wires.* Based on the model of split-gate quantum wires and using the Green's function method, a general solution for the electrostatic potential has been obtained. In particular, the depletion and pinchoff voltages of quantum wires before and after illumination have been calculated analytically. Several samples of split-gate quantum wires have been taken as examples for calculations and the calculated results agree well with experimental measurements. Our electrostatic model of split-gate quantum wires and its analytic solution provide both a general theoretical tool for studying gated semiconductor devices and important information for improving device performance.

7.2 Suggested Future Work

Related to the theoretical studies of this thesis, further work listed below would be of interest.

1. *Complex Coulomb-confined quantum wires.* This work would improve on the model of Coulomb-confined quantum wires by including a *ribbon of electrons*, which represents electrons at the exposed surface, over the ribbon of donors. The whole system is still charge-neutral. The complex Coulomb-confined quantum wires are closer to realistic quantum wires in structure.

2. *Many-body effects at high electron densities.* Our numerical results in Chapter 3 show that many-body effects are important in Coulomb-confined quantum wires at low and moderate electron densities. When the electron density is high, calculations are difficult because some weakly bound states are populated. Using the model of complex Coulomb-confined quantum wires, the potential well that confines electrons in the electron plane becomes stronger. Therefore, it may be possible to make calculations and study many-body effects at high electron densities.

3. *Populated weakly bound states.* The calculations in Chapter 3 show that weakly bound states can be populated in Coulomb-confined quantum wires when the electron density is sufficiently high or the distance between the ribbon of donors and the electron plane is sufficiently large. However, when a weakly bound state is populated, numerical calculations using the technique described in Chapter 2 are not reliable. Therefore, a different numerical approach is required to study the electronic structure of quantum wires when weakly bound states are populated.

4. *Experimental exploration of the energy level locking effect.* It is important to detect energy level locking in parallel quantum wires experimentally in a unambiguous way. At the end of Chapter 4, we suggested some methods using transport and optical properties.

5. *Energy level locking in other systems.* Because energy level locking is an effect of quasi-one-dimensional fermionic systems, this effect should also be observable in quasi-one-dimensional systems of "holes". Since the energy level locking effect is new, further general studies of this effect would be of much interest.

6. *Confining potentials of quantum dots.* The electrostatic model presented in Chapter 5 and the analytic calculations presented in Chapter 6 can be conveniently applied to quantum dots. Because the self-screening effect of electrons is absent when there are only one electron in the quantum dot, the confining potential of the quantum dot can be calculated *analytically*, which is certainly useful in studying the electronic structure of the quantum dot.

7. *Short split-gate quantum wires.* Using the electrostatic model presented in Chapter 5, it may also be possible to calculate the depletion and pinchoff voltages of *short* quantum wires analytically by using appropriate boundary conditions. Thus the effect of the length of quantum wires can be studied.

8. *Numerical calculations for split-gate quantum wires.* Based on the external confining potential obtained in Chapter 6, it is possible to calculate the electronic structure of split-gate quantum wires when electrons of the 2DEG (and even the un-ionized region) are present, for various gate voltages. Such calculations should be self-consistent and thus the calculation procedures described in Chapter 2 can be used.

9. *Properties of the un-ionized region.* The calculations in Chapter 6 show that an un-ionized region can occur in a realistic quantum wire. The presence of the un-ionized region can affect the migration of electrons (or even impurities) in the doped layer. The tunneling of electrons between the un-ionized region and the confined 2DEG would also be an interesting topic.

10. *Improving the electrostatic model of split-gate quantum wires.* The electrostatic model defined in Chapter 5 could be improved if one were to understand in more detail how surface electrons react to an external field, what determines the ratio between the densities of shallow donors and deep donors in the doped layer, and exactly how deep donors are affected by illumination. Numerical studies of tunneling effects in quantum wires would also be useful for improving the model.

7.3 Device Applications

The trend of semiconductor device technology has been to develop ever smaller devices, in the interest of increased speed and lower cost. For this reason, quantum wires have a great potential for device applications [192, 193, 194, 195, 196], such as in switches, transistors, sensors, and lasers.

With further improvement in fabrication technology, it should be possible to control layer thicknesses of and sizes of gates of quantum wires more accurately. Then the main uncertain factors are the exposed surface, at which electrons can be trapped and affected by the environment (surface adatoms), and donors, whose distribution between the deep levels and the shallow levels is difficult to control, especially when illumination is involved. There are also impurity scattering and potential fluctuations due to impurities [113], which can affect the characteristics of quantum wires significantly.

Surface properties are very complicated, especially when surfaces are affected by the environment. [171]. In solving the problem of the exposed surface in a quantum wire, one possibility is to place another gate on the exposed surface, with this new gate being isolated from the split gate. (This would be a technological challenge considering the small length scale involved for the exposed surface.) If this can be achieved in fabrication, not only would the uncertainty due to the exposed surface be eliminated, but also the lateral confinement of quantum wires would be more controllable.

As to the uncertainties due to donors, many studies are needed to understand *quantitatively* the mechanisms by which shallow donors interchange with deep donors, the dynamic behavior of donors during sample fabrication, and the process of exciting deep donors to shallow donors by illumination. Therefore, one should carry out more general studies of donors in bulk semiconductors and apply the new research results achieved there to the studies of quantum wires.

It is always constructive to search for new methods of doping so that the impurity (dopant) scattering of electrons is reduced. The application of the spacer layer in most current modulation-doped [36] samples is a typical example of this. However, there are other factors that should be considered, such as the ease with which electrons can be donated by donors, effectively confined at the GaAs-$Al_xGa_{1-x}As$ interface (the positive charges due to ionized donors are needed), and the whole system can be kept in equilibrium (large energy barriers are not desirable).

An interesting idea that was introduced [197] recently to improve control over the device is to use a "back gate voltage", which can control the density of the 2DEG independently. Thus, the split-gate voltage can be used to provide only the lateral confinement for electrons, because the changes of the 2DEG density caused by the split-gate voltage can be eliminated by adjusting the back gate voltage. This is another example of improving the ability to control quantum wire devices.

Because of the existing problems mentioned above, it will take some time before quantum wires reach the stage of commercial applications. Hopefully, this thesis will contribute to the understanding of the characteristics of quantum wires and facilitate their device applications.

Appendix: General Formalism of the Density Functional Theory of Hohenberg, Kohn and Sham

Consider a system of N fermions in its ground state. According to Hohenberg, Kohn, and Sham [136, 137], the total energy for the ground state of the system is a functional of the electron density $n(\mathbf{r})$

$$E[n] = T[n] + U[n] + E_{\mathrm{xc}}[n], \tag{7.1}$$

where $T[n]$, $U[n]$, and $E_{\mathrm{xc}}[n]$ are the *total* kinetic energy, Coulomb energy, and exchange and correlation energy of the system, respectively. The total Coulomb energy $U[n]$ can be expressed as

$$U[n] = \int V_{\mathrm{ext}}(\mathbf{r}) n(\mathbf{r}) d\mathbf{r} + \frac{e^2}{2(4\pi\varepsilon\varepsilon_0)} \int\int \frac{n(\mathbf{r}) n(\mathbf{r}')}{|\mathbf{r} - \mathbf{r}'|} d\mathbf{r} d\mathbf{r}', \tag{7.2}$$

where the two terms correspond to the potential energy due to an external field and the Coulomb interations between the fermions, respectively.

The variational form of Eq. (7.1) is

$$\delta\{E[n] - \mu \int n(\mathbf{r}) d\mathbf{r}\} = 0, \tag{7.3}$$

with the Lagrange multiplier μ determined by

$$\int n(\mathbf{r}) d\mathbf{r} = N. \tag{7.4}$$

Eq. (7.3) implies

$$\frac{\delta E[n]}{\delta n(\mathbf{r})} = \mu, \tag{7.5}$$

and μ is equal to the chemical potential of the system for large N.

Combining Eqs. (7.1), (7.2) and (7.5), one obtains

$$V_{\text{eff}}[n;\mathbf{r}] + \frac{\delta T[n]}{\delta n(\mathbf{r})} = \mu, \tag{7.6}$$

where $V_{\text{eff}}[n;\mathbf{r}]$ is the effective potential energy given by

$$V_{\text{eff}}[n;\mathbf{r}] = V_{\text{c}}(\mathbf{r}) + \frac{\delta E_{\text{xc}}[n]}{\delta n(\mathbf{r})}, \tag{7.7}$$

where V_{c} is the Coulomb energy *per electron*

$$V_{\text{c}} = V_{\text{ext}}(\mathbf{r}) + \frac{e^2}{4\pi\varepsilon\varepsilon_0}\int \frac{n(\mathbf{r}')}{|\mathbf{r}-\mathbf{r}'|}d\mathbf{r}'. \tag{7.8}$$

Now consider a system of N fermions in which there is no interation between the fermions but each fermion has a potential energy $V_{\text{ext}}(\mathbf{r})$ due to an external field. In this situation, Eq. (7.6) becomes

$$V_{\text{ext}}(\mathbf{r}) + \frac{\delta T[n]}{\delta n(\mathbf{r})} = \mu. \tag{7.9}$$

Since the fermions have no interactions, the many-particle wave function of the system is simply a Slater determinant of single-particle wave functions $\Psi_i(\mathbf{r})$, which satisfies the Schrödinger equation

$$\left[-\frac{h^2}{2m}\nabla^2 + V_{\text{ext}}(\mathbf{r})\right]\Psi_i(\mathbf{r}) = E_i\Psi_i(\mathbf{r}). \tag{7.10}$$

Correspondingly, the electron density is given by

$$n(\mathbf{r}) = \sum_{i=1}^{N}|\Psi_i(\mathbf{r})|^2, \tag{7.11}$$

where the summation is over the N lowest-lying orthonormal solutions of Eq. (7.10). Thus we have found a solution for Eq. (7.6) by solving Eqs. (7.10) and (7.11) instead.

For a system of electrons, the effective potential energy $V_{\text{eff}}[n;\mathbf{r}]$ contains contributions from both the Coulomb energy and the exchange-correlation energy. However, to solve Eq. (7.6), one can take $V_{\text{eff}}[n;\mathbf{r}]$ as an "external" potential energy and solve

$$\left[-\frac{h^2}{2m}\nabla^2 + V_{\text{eff}}(\mathbf{r})\right]\Psi_i(\mathbf{r}) = E_i\Psi_i(\mathbf{r}). \tag{7.12}$$

The wave functions given by Eq. (7.12) are called the density functional wave functions or Kohn-Sham wave functions [137]. In this way, the many-particle problem is effectively reduced to a single-particle problem.

The above results are rigorous. In practice, approximations are usually used in calculating the total exchange and correlation energy $E_{\rm xc}[n]$. According to Kohn and Sham [137], $E_{\rm xc}[n]$ can be expanded as

$$E_{\rm xc}[n] = \int d\mathbf{r} \left\{ \epsilon_{\rm xc}(n(\mathbf{r}))n(\mathbf{r}) + \epsilon_{\rm xc}^{(2)}(n(\mathbf{r}))|\nabla n(\mathbf{r})|^2 + \cdot \right\}, \tag{7.13}$$

where $\epsilon_{\rm xc}$ is the exchange-correlation energy *per electron*. If the electron density $n(\mathbf{r})$ varies slowly in space, it is usual to omit all the gradient terms and keep only the first term in Eq. (7.13). Correspondingly, the effective potential energy becomes a direct function of position

$$V_{\rm eff}(\mathbf{r}) = V_{\rm c}(\mathbf{r}) + \frac{d}{dn}\left\{ n\epsilon_{\rm xc}(n(\mathbf{r})) \right\}. \tag{7.14}$$

Such a treatment is called the *local density approximation* (LDA). The local density approximation has been very successful in studying the ground state properties of many systems, such as atoms, molecules, and crystalline solids [157].

Bibliography

[1] T. Ando, *J. Phys. Soc. Japan* **51**, 3900 (1982).

[2] K. A. Müller, W. Berlinger, P. Pfluger, V. Gelser, and G. J. Guntherodt, *Solid State Commun.* **55**, 803 (1985).

[3] G. Landwehr and S. Uchida, *Surf. Sci.* **160**, 718 (1986).

[4] J. G. Bednorz and K. A. Müller, *Z. Phys. B* **64**, 189 (1986); C. W. Chu, P. H. Hor, R. L. Meng, L. Gao, Z. J. Huang, amd Y. Q. Wand, *Phys. Rev. Lett.* **58**, 405 (1987).

[5] A. D. Yoffe, *Solid State Ionics.* **37**, 1 (1990).

[6] W. P. Su, J. R. Schrieffer, and A. J. Heeger, *Phys. Rev. Lett.* **42**, 1698 (1979).

[7] R. S. Kwok, G. Gruner, and S. E. Brown, *Phys. Rev. Lett.* **65**, 365 (1990); J. W. Brill, M. Chung, Y. K. Kuo, X. Zhan, E. Figueroa, and G. Mozurkewich, *Phys. Rev. Lett.* **74**, 1182 (1995).

[8] C. Weisbush and B. Vinter, *Quantum Semiconductor Structures*, (Academic Press, San Diego, 1991).

[9] C. W. J. Beenakker and H. van Houten, "Quantum Transport in Semiconductor Nanostructures", in *Solid State Physics, Advances in Research and Applications* Vol. 44, edited by H. Ehrenreich and D. Turnbull, (Academic Press, San Diego, 1991).

[10] S. E. Ulloa, A. MacKinnon, E. Castaño, and G. Kirczenow, "From Ballistic Transport to Localization", in *Handbook of Semiconductors* Vol. I, edited by P. T. Landsberg, (North-Holland, Amsterdam, 1992).

[11] E. H. C. Parker, *The Technology of Molecular Beam Epitaxy*, (Plenum Press, New York, 1992).

[12] L. L. Chang and B. C. Giessen, *Synthetic Modulated Structures*, (Academic, Orlando, 1985).

[13] M. L. Roukes, T. J. Thornton, A. Scherer, J. A. Simmons, B. P. van der Gaag, and E. D. Beebe, in *Science and Engineering of 1- and 0-Dimensional Semiconductors*, edited by S. P. Beaumont and C. M. Sotomayer-Torres, (Plenum, London, 1990).

[14] R. Dingle, W. Wiegmann, and C. H. Henry, *Phys. Rev. Lett.* **33**, 827 (1974).

[15] R. Dingle, A. C. Gossard, and W. Wiegmann, *Phys. Rev. Lett.* **34**, 827 (1975).

[16] K. von Klitzing, G. Dorda, and M. Pepper, *Phys. Rev. Lett.* **45**, 494 (1980).

[17] For a review of the Quantum Hall Effect, see R. E. Prange and S. M. Girvin, *The Quantum Hall Effect*, (Springer Verlag, New York, 1990).

[18] B. J. van Wees, H. van Houten, C. W. J. Beenakker, J. G. Williamson, L. P. Kouwenhoven, D. van der Marel, and C. T. Foxon, *Phys. Rev. Lett.* **60**, 848 (1988).

[19] D. A. Wharam, T. J. Thornton, R. Newbury, M. Pepper, H. Ahmed, J. E. F. Frost, D. G. Hasko, D. C. Peacock, D. A. Ritchie, and G. A. C. Jones, *J. Phys. C: Solid State Phys.* **21**, L209 (1988).

[20] C. G. Smith, M. Pepper, R. Newbury, H. Ahmed, D. G. Hasko, D. C. Peacock, J. E. F. Frost, D. A. Ritchie, G. A. C. Jones, and G. Hill, *J. Phys.: Condens. Matter* **1**, 6763 (1989).

[21] E. Tekman and S. Ciraci, *Phys. Rev. B* **40**, 8559 (1989).

[22] P. L. McEuen, B. W. Alphenaar, R. G. Wheeler, and R. N. Sacks, *Surf. Sci.* **229**, 312 (1990).

[23] Y. S. Joe and S. E. Ulloa, *Phys. Rev. B* **47**, 9948 (1993).

[24] G. Timp, R. E. Behringer, and J. E. Cunningham, *Phys. Rev. B* **42**, 9259 (1990).

[25] B. J. van Wees, L. P. Kouwenhoven, C. J. P. M. Harmans, J. G. Williamson, C. E. Timmering, M. E. I. Broekaart, C. T. Foxon, and J. J. Harris, *Phys. Rev. Lett.* **62**, 2523 (1989).

[26] J. H. F. Scott-Thomas, S. B. Field, M. A. Kastner, H. I. Smith, and D. A. Antoniadis, *Phys. Rev. Lett.* **62**, 583 (1989).

[27] S. E. Ulloa, E. Castaño, and G. Kirczenow, *Phys. Rev. B* **41**, 12350 (1990).

[28] L. P. Kouwenhoven, F. W. J. Hekking, B. J. van Wees, C. J. P. M. Harmans, C. E. Timmering, and C. T. Foxon, *Phys. Rev. Lett.* **65**, 351 (1990).

[29] K. Ismail, T. P. Smith III, W. T. Masselink, and H. I. Smith, *Appl. Phy. Lett.* **55**, 2766 (1989).

[30] G. Kirczenow, *Phys. Rev. B* **46**, 1439 (1992).

[31] Y. Sun and G. Kirczenow, *Phys. Rev. B* **47**, 4413 (1993).

[32] Y. Sun and G. Kirczenow, *Phys. Rev. Lett.* **72**, 2450 (1994).

[33] Y. Sun and G. Kirczenow, in *22nd Int. Conf. on the Phys. of Semicond.* in Vancouver, Canada, 1994, p. 1751.

[34] Y. Sun and G. Kirczenow, *Canadian J. Phys.* **73**, 357 (1995).

[35] Y. Sun, G. Kirczenow, A. S. Sachrajda, and Y. Feng, *J. Appl. Phys.* **77**, 6361 (1995).

[36] R. Dingle et al., *Appl. Phys. Lett.* **7**, 665 (1978).

[37] R. G. Wheeler, K. K. Choi, A. Goel, R. Wisnieff, and D. E. Prober, *Phys. Rev. Lett.* **49**, 1674 (1982).

[38] A. Scherer, M. L. Roukes, H. G. Craighead, R. M. Ruthen, E. D. Beebe, and J. P. Harbison, *Appl. Phys. Lett.* **51**, 2133 (1987).

[39] W. Hansen, M. Horst, J. P. Kotthaus, U. Merkt, C. Sikorski, and K. Ploog, *Phys. Rev. Lett.* **58**, 2586 (1987).

[40] W. J. Skocpol, L. D. Jackel, E. L. Hu, R. E. Howard, and L. A. Fetter, *Phys. Rev. Lett.* **49**, 951 (1982).

[41] J. P. Kirtley, Z. Schlesinger, T. N. Thesis, F. P. Milliken, and S. L. Wright, and L. F. Palmateer, *Phys. Rev. B* **34**, 5414 (1986).

[42] L. Bliek, E. Braun, G. Hein, V. Kose, J. Niemeyer, D. Weimann, and W. Schlapp, *Semicond. Sci. Technol.* **1**, 110 (1986).

[43] K. K. Choi, D. C. Tsui, and S. C. Palmateer, *Phys. Rev. B* **33**, 8216 (1986).

[44] H. van Houten, B. J. van Wees, M. G. J. Heijman, and J. P. André, *Appl. Phys. Lett.* **49** 1781 (1986).

[45] R. E. Behringer, P. M. Mankiewich, and R. E. Howard, *J. Vac. Sci. Technol. B* **5**, 236 (1987).

[46] M. L. Roukes, A. Scherer, S. J. Allen, Jr., H. G. Craighead, R. M. Ruthen, E. D. Beebe, and J. P. Harbison, *Phys. Rev. Lett. B* **59**, 3011 (1987).

[47] A. Scherer and M. L. Roukes, *Appl. Phys. Lett.* **55**, 377 (1989).

[48] T. J. Thornton, M. Pepper, H. Ahmed, D. Andrews, and G. J. Davies, *Phys. Rev. Lett.* **56**, 1198 (1986).

[49] H. Z. Zheng, H. P. Wei, D. C. Tsui, and G. Weimann, *Phys. Rev. B* **34**, 5635 (1986).

[50] H. G. Craighead, *J. Appl. Phys.* **55**, 4430 (1984).

[51] T. P. Smith III, H. Arnot, J. M. Hong, C. M. Knoedler, S. E. Laux, and H. Schmid, *Phys. Rev. Lett.* **59**, 2802 (1987).

[52] C. J. B. Ford, T. J. Thornton, R. Newbury, M. Pepper, H. Ahmed, G. J. Davies, and D. Andrews, *Superlatt. and Microstruct.* **4**, 541 (1988).

[53] C. J. B. Ford, T. J. Thornton, R. Newbury, M. Pepper, H. Ahmed, C. T. Foxon, J. J. Harris, and C Roberts, *J. Phys. C* **21**, L325 (1988).

[54] Y. Hirayama, S. Tarucha, Y. Suzuki, and H. Okamoto, *Phys. Rev.* **37**, 2774 (1988).

[55] Y. Hirayama and T. Saku, *Appl. Phys. Lett.* **54**, 2556 (1989).

[56] T. Hiramoto, K. Hirakawa, Y. Iye, and T. Ikoma, *Appl. Phys. Lett.* **54**, 2013 (1989).

[57] Y. Arakawa and H. Sakaki, *Appl. Phys. Lett.* **40**, 939 (1982).

[58] P. M. Petroff, A. C. Gossard, and W. Wiegmann *Appl. Phys. Lett.* **46**, 620 (1984).

[59] T. Fukui and H. Saito, *Appl. Phys. Lett.* **50**, 824 (1987); *J. Vac. Sci. Technol. B* **6**, 1373 (1988).

[60] H. Asai, S. Yamada, and T. Fukui, *Appl. Phys. Lett.* **51**, 1518 (1987).

[61] J. Motohisa, M. Tanaka, and H. Sakaki, *Appl. Phys. Lett.* **55**, 1214 (1989).

[62] C. S. Tsai, J. A. Lebens, C. C. Ahn, A. Nouhi, and K. J. Vahala, *Appl. Phys. Lett.* **60**, 240 (1992).

[63] S. Tsukamoto, Y. Nagamune, M. Nishioka, and Y. Arakawa, *Appl. Phys. Lett.* **62**, 49 (1993).

[64] K. Kash, J. M. Worlock, M. D. Sturge, P. Grabbe, J. P. Harbison, A. Scherer, and P. S. D. Lin, *Appl. Phys. Lett.* **53**, 1268 (1988).

[65] U. Meirav, M. Heiblum, and F. Stern, *Appl. Phys. Lett.* **52**, 1268 (1988).

[66] A. D. Wieck and K. Ploog, *Surf. Sci.* **229**, 252 (1990); *Appl. Phys. Lett.* **56**, 928 (1990).

[67] F. Brinkop, W. Hansen, J. P. Kotthaus, and K. Ploog, *Phys. Rev. B* **37**, 6547 (1988).

[68] S. Nakata, Y. Hirayama, S. Tarucha, and Y. Horikoshi, *J. Appl. Phys.* **69**, 3633 (1991).

[69] P. W. Anderson, *Phys. Rev.* **109** 1492 (1958).

[70] G. Bergmann, *Phys. Rep.* **107** 1 (1984).

[71] D. J. Thouless, *Phys. Rep.* **13** 93 (1974).

[72] K. B. Efetov, *Adv. Phys.* **32** 53 (1983).

[73] J. M. Ziman, *Models of Disorder*, (University Press, Cambridge, 1979).

[74] N. E. Cusack, *The Physics of Structurally Disordered Materials: An Introduction* (Adam Hilger, Bristol, 1987).

[75] I, M. Lifshitz, S. A. Gredescul, and L. A. Pastur, *Introduction to the Theory of Disordered Systems*, (Wiley, New York, 1988).

[76] R. J. Elliott, J. A. Krumhansl, and P. L. Leath, *Rev. Mod. Phys.* **46** 465 (1974).

[77] A. A. Goglin, *Phys. Rep.* **86** 2 (1982).

[78] B. J. van Wees, L. P. Kouwenhoven, E. M. M. Willems, C. J. P. M. Harmans, J. E. Mooij, H. van Houten, C. W J. Beenakker, J. G. Williamson, and C. T. Foxon, *Phys. Rev. B* **43**, 12431 (1991).

[79] H. van Houten, C. W J. Beenakker, P. H. M. van Loosdrecht, T. J. Thornton, H. Ahmed, M. Pepper, C. T. Foxon, and J. J. Harris, *Phys. Rev. B* **37** 8534 (1988).

[80] R. Landauer, *IBM J. Res. Develop.* **1**, 223 (1957).

[81] D. S. Fisher and P. A. Lee, *Phy. Rev. B* **23**, 6851 (1981).

[82] E. N. Economou and C. M. Soukoulis, *Phy. Rev. Lett.* **46**, 618 (1981); *Phy. Rev. Lett.* **47**, 973 (1981).

[83] M. Büttiker, *Phy. Rev. Lett.* **57**, 1761 (1986).

[84] Y. Imry, in *Directions in Condensed Matter Physics* Vol. 1, edited by G Grinstein and G. Mazenko, (World Scientific, Singapore, 1986).

[85] A. D. Stone and A. Szafer, *IBM J. Res. Develop.* **32**, 618 (1988).

[86] R. Landauer, *J. Phys. Condens. Matter* **1**, 8099 (1989).

[87] G. Kirczenow, *Solid State Commun.* **68**, 715 (1988); *Phys. Rev. B* **39**, 10452 (1989).

[88] A. Szafer and A. D. Stone, *Phys. Rev. Lett.* **62**, 300 (1989).

[89] Y. Avishai, M. Kaveh, S. Shatz, and Y. B. Band, *J. Phys.: Condens. Matter* **1**, 6907 (1989).

[90] Y. Hirayama and T. Saku, *Jpn. J. Appl. Phys.* **29**, L268 (1990); *Phys. Rev. B* **42**, 11408 (1990).

[91] S. W. Hwang, J. A. Simmons, D. C. Tsui, and M. Shayegan, *Phys. Rev.* **44**, 13497 (1991).

[92] P. E. Schmidt, M. Okada, K. Kosemura, and N. Yokoyama, *Jpn. J. Appl. Phys.* **30**, L1921 (1991).

[93] P. J. Simpson, D. R. Mace, C. J. B. Ford, I. Zailer, M. Pepper, D. A. Ritchie, J. E. F. Frost, M. P. Grimshaw, and G. A. C. Jones, *Appl. Phy. Lett.* **63**, 3191 (1993).

[94] D. A. Wharam, M. Pepper, H. Ahmed, J. E. F. Frost, D. G. Hasko, D. C. Peacock, D. A. Ritchie, and G. A. C. Jones, *J. Phys. C: Solid State Phys.* **21**, L887 (1988).

[95] P. C. Main, P. H. Beton, B. R. Snell, A. J. M. Neves, J. R. Owers-Bradley, L. Eaves, S. P. Beaumont, and C. D. W. Wilkinson, *Phys. Rev. B* **40**, 10033 (1989).

[96] L. P. Kouwenhoven, B. J. van Wees, W. Kool, C. J. P. M. Harmans, A. A. M. Staring, and C. T. Foxon, *Phys. Rev.* **40**, 8083 (1989).

[97] Y. Hirayama and T. Saku, *Solid State Commun.* **73**, 113 (1990); *Phys. Rev. B* **41**, 2927 (1990).

[98] S. Yamada and M. Yamamoto, *Phys. Rev. B* **43**, 9369 (1991).

[99] L. I. Glazman and M Jonson, *Phys. Rev. B* **41**, 10686 (1990).

[100] C. W. J. Beenakker and H. van Houten, *Phys. Rev. B* **39**, 10445 (1989).

[101] E. G. Haanapel and D. van der Marel, *Phys. Rev. B* **39**, 5489 (1989).

[102] C. S. Chu and R. S. Sorbello, *Phys. Rev. B* **44**, 5941 (1989).

[103] P. F. Bagwell, *Phys. Rev. B* **41**, 10354 (1990).

[104] E. Tekman and S. Ciraci, *Phys. Rev. B* **42**, 9098 (1990).

[105] J. Faist, P. Guret, and H. Rothuizen, *Phys. Rev. B* **42**, 3217 (1990).

[106] Y. P. Li, D. C. Tsui, J. J. Heremans, J. A. Simmons, and G. W. Weimann, *Appl. Phys. Lett.* **57**, 774 (1990).

[107] D. H. Cobden, N. K. Patel, M. Pepper, D. A. Ritchie, J. E. F. Frost, and G. A. C. Jones, *Phys. Rev. B* **44**, 1938 (1991).

[108] C. Dekker, A. J. Scholten, F. Liefrink, R. Eppenga, H. van Houten, and C. T. Foxon, *Phys. Rev. Lett.* **66**, 2148 (1991).

[109] C. J. B. Ford, S. Washburn, R. Newbury, C. M. Knoedler, and J. M. Hong, *Phys. Rev. B* **44**, 7339 (1991).

[110] J. Masek, P. Lipavski, and B. Kramer, *J. Phys. Condens. Matter* **1**, 6395 (1989).

[111] S. He and S. Das Sarma, *Phys. Rev. B* **40**, 3379 (1990).

[112] H Akera and T. Ando, *Phys. Rev. B* **41**, 11676 (1990); *Surf. Sci.* **229**, 268 (1990).

[113] J. A. Nixon and J. H. Davies, *Phys. Rev. B* **41**, 7929 (1990).

[114] C. S. Lent, *Appl. Phys. Lett.* **57**, 1678 (1990).

[115] A. Weisshaar, J. Lary, S. M. Goodnick, and V. K. Tripathi, *J. Appl. Phys.* **70**, 355 (1991).

[116] K. Kash, *J. Lumin.* **46**, 69 (1990).

[117] M. Kohl, D. Heitmann, W. W. Rühle, P. Grambow, and K. Ploog, *Phys. Rev. B* **41**, 12338 (1990).

[118] W. I. Friesen and B. Bergersen, *J. Phys. C: Solid State Phy.* **13**, 6627 (1980).

[119] D. Mackens, D. Heitmann, L. Prager, J. P. Kotthaus, and W. Beinvogl, *Phys. Rev. Lett.* **53**, 1485 (1984).

[120] W. M. Que and G. Kirczenow, *Phys. Rev. B* **37**, 7153 (1988).

[121] A. Gold and A. Ghazali, *Phys. Rev. B* **41**, 7626 (1990).

[122] W. Kohn, *Solid State Phys.* **5**, 257 (1957).

[123] D. J. BenDaniel and C. B. Duke, *Phys. Rev.* **152**, 683 (1966).

[124] V. J. Emery, "Theory of the One-Dimensional Gas", in *Highly Conducting One-Dimensional Solids*, edited by T. J. Devreese, R. P. Evrard, and V. E. van Doren, (Plenum Press, New York, 1979).

[125] J. Sólyom, *Adv. Phys.* **28**, 201 (1979).

[126] F. D. M. Haldane, *J. Phys. C* **14**, 2585 (1981); *Phys. Rev. Lett.* **47**, 1840 (1981).

[127] B. G. Levi, *Phys. Today* **47** 21 (1994).

[128] S. Tarucha, T. Honda, and T. Saku, *Solid State Commun.* **94**, 413 (1995).

[129] N. H. March, *Adv. Phys.* **6**, 1 (1957).

[130] S. E. Laux and F. Stern, *Appl. Phy. Lett.* **49**, 91 (1986).

[131] S. E. Laux, D. J. Franck, and F. Stern, *Surf. Sci.* **196**, 101 (1988).

[132] T. Ando, A. B. Fowler, and F. Stern, *Rev. Mod. Phys.* **54**, 437 (1982).

[133] G. W. Bryant, *Phys. Rev. Lett.* **59**, 1140 (1987).

[134] P. A. Maksym and T. Chakraborty, *Phys. Rev. Lett.* **65**, 108 (1990).

[135] J. Harris, J. A. Pals, and R. Woltjer, *Rep. Prog. Phys.* **52**, 1217 (1989).

[136] P. Hohenberg and W. Kohn, *Phys. Rev.* **136**, B864 (1964).

[137] W. Kohn and L. J. Sham, *Phys. Rev.* **140**, A1133(1965).

[138] W. Kohn, *Phys. Rev. Lett,* **56**, 2219 (1986).

[139] F. Stern, in *Physics of Low-Dimensional Semiconductor Structures*, edited by P. Butcher, N. H. March, and M. P. Tosi, (Plenum Press, New York, 1993).

[140] F. Stern and S. Das Sarma, *Phys. Rev. B* **30**, 1840 (1984).

[141] A. Y. Shik, *Sov. Phys. Semicond.* **19**, 915 (1985).

[142] W. Y. Lai and S. Das Sarma, *Phys. Rev. B* **33**, 8874 (1986).

[143] V. B. Shikin, *JETP Lett.* **50**, 167 (1989)

[144] J. H. Davies, *Semicond. Sci. Technol.* **3**, 995 (1988).

[145] L. I. Glazman and I. A. Larkin, *Superlatt. Microstruc.* **6**, 32 (1991).

[146] J. H. Davies, I. A. Larkin, and E. V. Sukhorukov, *J. Appl. Phys.* **77**, 4504 (1995).

[147] J. H. Luscombe and M. Luban, *Appl. Phy. Lett.* **57**, 61 (1990).

[148] J. H. Luscombe, A. Bouchard, and M. Luban, *Phy. Lett. Rev. B* **46**, 10262 (1992).

[149] M. Chen, W. Porod, and D. J. Kirkner, *J. Appl. Phy.* **75**, 2545 (1994).

[150] K. Kojima, K. Mitsunaga, and K. Kyuma, *Appl. Phy. Lett.* **55**, 862 (1989).

[151] T. Kerkhoven, A. T. Galick, U. Ravaioli, J. H. Arends, and Y. Saad, *J. Appl. Phy.* **68**, 3461 (1990).

[152] A. Nakamura and A. Okiji, *J. Phys. Soc. Jpn.* **60**, 1873 (1991).

[153] U. Ravaioli, T. Kerkhoven, M. Raschke, and A. T. Galick, *Superlatt. Microstruc.* **11**, 343 (1992).

[154] F. Stern, *Phys. Rev. Lett.* **30**, 278 (1973).

[155] M. Jonson, *J. Phys. C* **9**, 3055 (1976).

[156] B. Tanatar and D. M. Ceperly, *Phys. Rev. B* **39**, 5005 (1989).

[157] R. O. Jones and O. Gunnarsson, *Rev. Mod. Phys.* **61**, 689 (1989).

[158] L. D. Landau and E. M. Lifshtz, *Quantum Mechanics, Non-Relativistic Theory* (Pergamon, New York, 1986), 3rd ed., Sec. 21.

[159] Y. Feng, A. S. Sachrajda, R. P. Taylor, J. A. Adams, M. Davies, P. Zawadzki, P. T. Coleridge, D. Landheer, P. A. Marshall, and R. Barber, *Appl. Phy. Lett.* **63**, 1666 (1993).

[160] R. P. Taylor, J. A. Adams, M. Davies, P. A. Marshall, and R. Barber, *J. Vac. Sci. Technol. B* **11**, 628 (1993).

[161] S. Yang, M. J. Berry, A. S. Adourian, R. M. Westervelt, and A. C. Gossard, *Bull. Am. Phys. Soc.* **37**, 70 (1994).

[162] N. Lifshitz, A. Jayaraman, and R. A. Logan, *Phys. Rev. B* **21**, 670 (1980).

[163] T. Ishikawa, J. Saito, S. Sasa, and S. Hiyamizu, *Jpn. J. Appl. Phys.* **21**, L675 (1982).

[164] For a review, see D. V. Lang, "DX Centers in III-V Alloys", in *Deep Centers in Semiconductors*, edited by S. T. Pantelides, (Gordon and Breach Science Pubishers, Switzerland, 1992).

[165] D. V. Lang and R. A. Logan, *Phys. Rev. Lett.* **39**, 635 (1977).

[166] D. V. Lang, R. A. Logan, and M. Jaros, *Phys. Rev. B* **19**, 1015 (1979).

[167] R. Legros, P. M. Mooney, and S. L. Wright, *Phys. Rev. B* **35**, 7505 (1987).

[168] D. J. Chadi and K. J. Chang, *Phys. Rev. Lett.* **61**, 873 (1988); *Phys. Rev. B* **39**, 10063 (1989).

[169] G. A. Northrop and P. M. Mooney *J. Elect. Mater.* **20**, 13 (1991).

[170] N. Chand, T. Henderson, J. Klem, W. T. Masselink, R. Fischer, Y. C. Chang, and H. Morkoc, *Phys. Rev. B* **80**, 4431 (1984).

[171] For reviews of surface and interface properties, see H. Luth, *Surfaces and Interfaces of Solids*, (Springer-Verlag, Berlin, 1993), and W. Mönch, *Semiconductor Surfaces and Interfaces*, (Springer-Verlag, Berlin, 1993).

[172] Private discussion with A. S. Sachrajda and Y. Feng, the experimentalists of sample fabrication and conductance measurements at the Institute of Microstructural Sciences, NRC, Canada.

[173] W. E. Spicer, P. W. Chye, P. Skeath, I. Lindau, and C. Y. Su, *J. Vac. Sci. Technol.* **16**, 1422 (1979).

[174] M. Mattern-Klossen and H. Luth, *Surf. Sci.* **162**, 610 (1985).

[175] W. E. Spicer, I. Lindau, P. Skeath, and C. Y. Su, *J. Vac. Sci. Technol.* **17**, 1019 (1980).

[176] T. C. Chiang, R. Ludeke, M. Aono, G. Landgren, F. J. Himpsel, D. E. Eastman, *Phys. Rev. B* **27**, 4770 (1983).

[177] S. P. Svensson, J. Kanski, T. G. Anderson, P. O. Nilsson, *J. Vac. Sci. Technol. B* **2**, 235 (1984).

[178] W. Chen, D. Mao, S. Ahsan, A. Kahn, *J. Vac. Sci. Technol. B* **10**, 1886 (1992).

[179] V. Heine, *Phys. Rev.* **138 A**, 1689 (1965).

[180] J. R. Waldrop,*J. Vac. Sci. Technol. B* **2**, 445 (1984).

[181] N. Newman, W. E. Spicer, T. Kendelewicz, and I. Lindau, *J. Vac. Sci. Technol. B* **4**, 931 (1986).

[182] A. B. McLean and R. H. Williams, *J. Phys. C* **21**, 783 (1988).

[183] V. Heine, *Phys. Rev. Lett.* **56**, 2755 (1986).

[184] E. T. Yu, J. O. McCaldin, and T. C. McGill, "Band Offsets in Semiconductor Heterojunctions", in *Solid State Physics, Advances in Research and Applications* Vol. 46, edited by H. Ehrenreich and D. Turnbull, (Academic Press, San Diego, 1992).

[185] R. C. Miller, D. A. Kleinman, and A. C. Gossard, *Phys. Rev. B* **29**, 7085 (1984).

[186] H. Okumura, S. Misawa, S. Yoshida, and S. Gonda, *Appl. Phys. Lett.* **46**, 377 (1985).

[187] J. Batey and S. L. Wright, *Surf. Sci.* **174**, 320 (1986).

[188] C. B. Duke, "Tunneling in Solids", in *Solid State Physics*, Supplement Vol. 10, edited by F. Seitz, D. Turnbull, and H. Ehrenreich, (Academic Press, New York, 1969); G. Garcia-Calderón, "Tunneling in Semiconductor Resonant Structures", in *Physics of Low-Dimensional Semiconductor Structures*, edited by P. Butcher, N. H. March, and M. P. Tosi, (Plenum Press, New York, 1993).

[189] J. D. Jackson, *Classical Electrodynamics*, 2nd Edition, (John Wiley & Sons, New York, 1975), Section 1.10.

[190] R. J. Haug, A. H. MacDonald, P. Streda, and K. von Klitzing *Phys. Rev. Lett.* **61**, 2797 (1988).

[191] S. Washburn, A. B. Fowler, H. Schmid, and D. Kern, *Phys. Rev. Lett.* **61**, 2801 (1988).

[192] F. W. Sheard and L. Eaves, *Nature* **333**, 600 (1988).

[193] A. Khurana, *Physics Today* **41**, 21 (1988).

[194] E. Kapon, S. Simhony, R. Bhat, and D. M. Hwang, *Appl. Phys. Lett.* **55**, 2715 (1989).

[195] M. J. Kelly, *Semicond. Sci. Technol.* **5**, 1209 (1990).

[196] R. Landauer, *Physica A* **168**, 75 (1990).

[197] A. R. Hamilton, J. E. F. Frost, C. G. Smith, M. J. Kelly, E. H. Linfield, C. J. B. Ford, D. A. Ritchie, G. A. C. Jones, and M. Pepper, *Appl. Phys. Lett.* **60**, 2782 (1992).